Changes in Acetylcholine Receptor Expression; Neuromuscular Junction Morphology and Associated Myonuclei in *BALB/C* Mice Following Muscle Contusion Injury

by

Elizabeth Adrienne Louw

Thesis presented for the degree of Master in Physiology in

the Faculty of Science at

Stellenbosch University

Supervisor: Prof Kathryn H. Myburgh

a l·NJŎK 2015

DECLARATION

By submitting this thesis electronically, I declare that the entirety of the work contained therein is my own, original work, that I am the sole author thereof (save to the extent explicitly otherwise stated), that reproduction and publication thereof by Stellenbosch University will not infringe any third party rights and that I have not previously in its entirety or in part submitted it for obtaining any qualification.

Elizabeth Adrienne Louw

Date: January 2015

ABSTRACT

Contusion injuries cause significant muscle damage, that effects skeletal muscle in its entirety, including the innervating motorneuron and the myofibre's neuromuscular junction (NMJ). Upon injury, the acetylcholine receptors (AChR) scatter and disintegrate yet reaggregate over time to re-create an optimally functioning motor end-plate. This process involves the upregulation of the receptor subunits' – α, β, γ, δ, ε – expression to varying degrees.

Satellite cells are key role players in muscle regeneration, but studies linking the regenerative roles of satellite cells to the rehabilitating NMJ are limited. Moreover, the majority of studies on acetylcholine receptors investigate the effects of a denervation event rather than an injury that affects the muscle tissues in their entirety. Bromodeoxyuridine (BrdU) is a useful tool in labelling and tracking proliferated satellite cells.

Two experimental groups (referred to as PCR and BrdU group) of male BALB/C mice were subjected to a hind limb contusion injury induced with the mass-drop technique. Alzet® mini-osmotic pumps delivering BrdU (50 mM, 1.0 $\mu l.h^{-1}$ release rate) were inserted into the BrdU group prior to injury. Animals were sacrificed at days 1, 3, 5, 7, 10 and 14 post injury. Both injured and contralateral, non-injured *gastrocnemius* muscles were collected. qPCR was performed for AChR-γ and AChR-ε mRNA expression on the muscles of the PCR mice.

Muscles from the BrdU group were cryo-sectioned in longitudinal orientation and stained with 1) H&E and 2) immunohistochemically with α-bungarotoxin to visualise AChRs; and also with antibodies against laminin and BrdU. Images were obtained by light microscopy (1) to detect and describe contusion injury in longitudinal section and confocal microscopy (2) to observe the form, prevalence and arrangement of NMJs along both the injured and non-injured muscle. AChRs position themselves into junctional folds that adopted a coral-like appearance – identifiable as a NMJ. A 3D z-stack image at 40x magnification revealed myonuclei residing beneath the NMJ in intimate connection.

These NMJ were arranged along the muscle in central band; however contusion injury resulted in a disintegration of part of or the entire junctional complex.

Super-resolution microscopy revealed in depth structural arrangement in the intact NMJ. This became jagged and dispersed following contusion injury, by 7 days. Robust, regenerating NMJs were detected in muscle sections at 14 days post injury. Surface area and volume were measured and

revealed a trend towards a decrease in NMJ size at 7 days post injury, followed by an exaggerated increase in NMJ size by day 14 post injury.

A two-step staining procedure exposed $BrdU^+$ cells residing beneath the neuromuscular junction at 14 days post injury.

The results of this study show that NMJ morphology is indeed affected by muscle contusion injury, and repairs itself by increasing its AChR subunit production. We explored novel techniques for analysis of neuromuscular morphology and its changes after injury and during regeneration. We have also ascertained the migration of satellite cells to beneath the NMJ following contusion injury. These findings lay the foundation for future research to better understand the role players involved in neuromuscular regeneration.

OPSOMMING

Kontusie-beserings veroorsaak beduidende spierskade wat skeletspiere as geheel beïnvloed, insluitend die innerverende motorneuron en die spierweefsel se neuromuskulêre-aansluiting (NMA). Tydens besering disintegreer en spat die asetielcholienreseptore (AChR) uitmekaar, en hergroepeer tog oor tyd om 'n optimaal-funksionerende motor-eindplaat te herskep. Hierdie proses behels die opregulering van die reseptor-subeenhede – α, β, γ, δ, ε – uitdrukking tot verskillende grade.

Satellietselle is die sleutelrolspelers in hergenerering van spierweefsel, maar min studies wat die verband tussen hergenererende funksies van satellietselle en die rehabilitasie van NMA ondersoek is beskikbaar. Verder behandel die meerderheid van die studies wat asetielcholienreseptore ondersoek die gevolge van 'n senuwee-onderbreking, in plaas van beserings wat die spierweefsel as geheel beïnvloed. Bromodeoksi-uridine (BrdU) is 'n nuttige hulpmiddel in die merking en die monitering van prolifereerde satellietselle.

Twee eksperimentele groepe (naamlik PCR en BrdU groepe) van manlike BALB/C muise was onderworpe aan kontusie-besering van agterste ledemate, wat met die gewigimpaktegniek veroorsaak is. Alzet® mini-osmotiese-pompe wat BrdU lewer (50 mM, 1.0 µl.h^{-1} vrylatingstempo) is voor die besering in die BrdU groep ingeplant. Diere is geslag en die beseerde en kontralaterale, nie-beseerde gastrocnemius-spiere is ingesamel. qPCR is gedoen vir AChR-γ en AChR-ε mRNA uitdrukking op die spiere van die PCR-muise.

‘n Lengte-kriodeursnee van spiere van die BrdU groep was geneem en is met 1) H&E gekleur en 2) immunohistochemies gekleur met α-bungarotoksien om AChRs te visualiseer; en ook met teenliggaampies gekleur vir laminin en BrdU. Beelde is verkry deur ligmikroskopie (1) om kontusie besering in lengtesnee te observeer en te beskryf, en konfokale mikroskopie (2) om die vorm, voorkoms en rangskikking van NMAs langs beide die beseerde en nie-beseerde spiere te observeer. AChRs het hulself in aansluitingsvoue posisioneer en 'n koraal-agtige voorkoms aangeneem - wat as 'n NMA identifiseer kan word. 'n 3D z-stapel beeld op 40x vergroting het gewys dat myonukleusse in ‘n noue verband onder die neuromuskulêre aansluiting teenwoordig is.

Hierdie neuromuskulêre-aansluitings is gereël langs die spiere in sentrale band; hoewel kontusie-besering gelei tot 'n verbrokkeling van 'n gedeelte of van die hele aansluitingskompleks.

Super-resolusie mikroskopie het ‘n in-diepte strukturele rangskikking getoon in ongeskonde NMA. Dit het binne 7 dae gekronkel en versprei na kontusie-besering. Robuuste, hergenererende NMAs is 14 dae na die besering in spierlengtesnee waargeneem. Oppervlakte en volume is gemeet en het

getoon dat NMA grootte 7 dae na besering neig om af te neem, gevolg deur 'n oordrewe toename in NMA grootte op die 14de dag na besering.

'n Twee-stap verkleuring-prosedure het 14 dae na die besering BrdU^{+} selle onder die neuromuskulêre aansluiting blootgestel.

Die resultate van hierdie studie toon dat NMA morfologie inderdaad deur kontusie-besering van spiere beïnvloed, en herstel self deur die van die AChR subeenheid produksie te verhoog. Ons verken nuwe tegnieke vir analisering van neuromuskulêre morfologie en veranderinge na 'n besering en tydens hergenerering. Ons het ook vasgestel dat migrasie van satelliet selle onder die NMA na kontusie-besering plaasvind. Hierdie bevindinge lê die grondslag vir toekomstige navorsing om die rolspelers betrokke by neuromuskulêre hergenerering beter te verstaan.

ACKNOWLEDGEMENTS

I wish to thank the following people for the part they played in the completion of this project:

My supervisor, Prof Kathy Myburgh for her excellent guidance, understanding and support and for enabling me to explore this novel research field. It has been a privilege to work with and learn from you.

Lize Engelbrecht for setting such an inspiring example. From her invaluable guidance from the start of my research experience in the department - through countless hours of teaching, optimising and imaging as well as her moral support and understanding during the challenging phases of this project. Thank you my research big-sister!

Tayla Faulmann for being an enthusiastic and capable student and lending a fresh pair of eyes to my project in this final year of Masters, as well as being such a brilliant conference-buddy!

Dr Noel Markgraaf for his time and expertise in the Animal Unit.

Dr Peter Durcan for his PCR expertise and assistance.

Ashwin Isaacs for his instrumental guidance in the Histology lab.

Jeandre Viljoen for his cherished philosophical input about Masters, humans and life.

Dr Filippo Macaluso for his solid advice on administering the contusion injury and straight forward solutions to BrdU problems. And for being so Italian about everything.

Dr Kristin Sainani from Stanford Medical College, USA, for her dynamic Writing in the Sciences course.

The department in its entirety for being a place brimming with diversity, silliness, camaraderie and beautiful people.

My family and friends who supported me in all their unique and different ways as I went through this challenging, yet exciting journey.

The NRF and Stellenbosch Support Bursary for the financial support.

WhiteSci for the Travel Bursary.

And most importantly, to God, for catching me, raising me up and leading me onwards.

NOMENCLATURE

α-Btx	α-Bungarotoxin
ACh	Acetylcholine
AChE	Acetylcholinesterase
AChR	Acetylcholine Receptor
ANOVA	Analysis of Variance
AP	Action Potential
BoTX	Botulinum Toxin
BrdU	Bromodeoxyuridine (5-bromo-2-deoxyuridine)
BSA	Bovine Serum Albumin
BW	Body weight
Ca^{2+}	Calcium
ChAT	Choline Acetyltransferase
CT	Cycle Threshold
cDNA	Complementary Deoxyribonucleic acid
ChAT	Choline Acetyltransferase
DoK7	Downstream of Kinase 7
GAPDH	Glyceraldehyde-3-phosphate Dehydrogenase
H&E	Haematoxylin and Eosin
HCl	Hydrochloric Acid
LM-221	Laminin-221
Lrp4	Low-density Lipoprotein Receptor-related Protein 4
mAChR	Muscarinic Acetylcholine Receptor
MHC	Myosin Heavy Chain
MHCf	Fetal Myosin Heavy Chain
MRF	Myogenic Regulatory Factors
mRNA	Messenger Ribonucleic Acid

MuSK	Muscle Specific Tyrosine Kinase
AChR	Acetylcholine Receptor
AChR-ε	Adult Acetylcholine Receptor
AChR-γ	Fetal Acetylcholine Receptor
NMJ	Neuromuscular Junction
PBS	Phosphate Buffered Saline
qPCR	Quantitative Real Time Polymerase Chain Reaction
SC	Satellite Cell
SFI	Sciatic Functional Index
VGCC	Voltage-gated calcium Channels
VGSC	voltage-gated Sodium Channels
V/ZS	Volume/z-stack number

Table of Contents

Chapter 1 Literature Review

APPENDICES

LIST OF FIGURES

LIST OF TABLES

Chapter1 Literature Review

1.1 Introduction

"For humans, as for most members of the animal kingdom, to move is to survive."[1]

Muscle Contusion Injury

Skeletal muscle tissue spans the interior of the body - providing for movement and an additional protective function for the internal organs. Therefore, skeletal muscle is regularly subjected to many types of injury, or myotrauma, (e.g. mechanical, chemical or thermal) at various levels of severity. In a study involving 6300 healthy adults, ± 25 % experienced a musculoskeletal injury of some sort within 12 months—of which 83 % were activity-related[2]. Contusion injuries commonly occur in sports, particularly contact sports, as well as in motor vehicle accidents and in industrial settings. A contusion injury is defined as an event where a blunt non-penetrating object impacts on the skeletal muscle, crushing the local tissue[3]. This results in acute loss of structure and function, followed by muscle mass breakdown. In some instances, entire limbs are debilitated. In severe cases, death can result[3]!

Muscle fibres subjected to contusion injuries are compressed and torn. Contusions can be complicated by additional bone fracturing that threatens to puncture the already traumatised muscle and increases the extent and complexity of the injury. The severity of these injuries depends on which particular muscle has been affected and the degree of impact[4].

In this study, events following muscle contusion injury will be investigated. Two particular components that are close to, and interact with, muscle fibres will receive most attention, namely satellite cells and the neuromuscular junction.

Satellite cells

Satellite cells (SC) are the muscle's resident stem cells that are activated in events such as myotrauma and proliferate to produce additional muscle cells (myoblasts). These myoblasts assist with both muscle repair and the regeneration of new myofibres in a manner that is sustainable for the satellite cell pool. The various roles of satellite cells in the process of muscle repair have been extensively researched[3,5,6,7,8,9,10,11,12,13,14,15,16,17,18,19,20,21,22,23] and will be discussed in Section 1.3.

The Neuromuscular Junction

The neuromuscular junction (NMJ) encompasses the area connecting the myofibre and its innervating motor neuron – providing the crucial link for communication between the two[25–27]. Damage to the neuromuscular junction results in its degradation and results in the inability of the myofibre to receive and respond to signals sent from the motor neuron. This leads to loss of contractile function and muscle wastage[27–31].

Acetylcholine receptors (AChRs) are the key components of the neuromuscular junction, arranged along the junctional folds in the muscle membrane to accommodate the incoming nerve axon. AChRs receive the neurotransmitter, acetylcholine, which initiates the action potential in the muscle fibre and leads to muscle contraction. Different AChR subunits exist which create different types of AChRs. Skeletal muscle initially expresses a fetal type – AChR-γ – and, post-natally, a mature type – AChR-ε.

Following strain injury, AChRs scatter from their junctional complexes, or even disintegrate[26]. In events where the nerve is damaged, the lack of neural stimulation also promotes scattering and disintegration of the AChRs.

During regeneration, the synaptic AChR regions are replenished by either recycled AChRs, or newly synthesized AChRs. A transcriptional switch occurs between the fetal - and adult AChR type as myofibres revert back to predominantly fetal AChR expression in the beginning phases of NMJ regeneration and gradually shift back to producing the adult type AChR as NMJ integrity is restored.

This study aimed to measure the changing expression of AChR-γ and -ε following muscle contusion injury and to describe and quantify the morphological changes of the NMJ following injury as well as be the first to describe and quantify the morphological changes in the regenerating NMJ. Additionally, this study strove to identify activated satellite cells beneath the regenerating NMJ to announce a supportive role played by the SCs in NMJ repair.

1.2 Skeletal muscle

1.2.1 Introduction

Skeletal muscle consists of a multifaceted arrangement of muscle cells (muscle fibres) and represents the largest tissue mass in the body[3]. Skeletal muscle mass accounts for 34.1 ± 5.7% of body weight in women (healthy young females, age: 18-29 yr; weight: 65.0 ± 16.8 kg) and 42.3 ± 4.4

% in men (healthy young males, age: 18-23 yr; weight: 79.9 ± 15.4 kg)[32]. Skeletal muscle allows for respiration; postural stability; joint movement and locomotion and force production[3,33] - crucial functions for the independent, mobile human being. Its complex nature involves other structures in close proximity, such as a highly organised nerve- and blood vessel networks; and an extracellular connective-tissue matrix.

1.2.2 Anatomy

1.2.1.1 Myofibres

Muscle fibres, also referred to as myofibres, are elongated muscle cells and appear distinctly spindle-shaped, averaging between 10-100 µm in diameter[33] and reaching lengths of up to 12 cm[1]. Myofibres are abundant in skeletal muscle, with the large muscles of the lower limbs boasting the most fibre bundles. In humans, around 271 350 myofibres reside in the *tibialis anterior* and as many as 1 033 000[1] in the medial *gastrocnemius* – the muscle of focus in this study.

A plasma membrane – the sarcolemma – encloses each myofibre[1]. The sarcolemma, in turn, is coated by an extracellular matrix of glycoproteins called the basement membrane[1,34]. This membrane is composed of two layers: an internal basal lamina and an external reticular lamina[34].

Multiple nuclei (specifically termed myonuclei) are situated on the borders of the muscle fibre, nestled under the sarcolemma[3]. Each myofibre also possesses a number of muscle stem cells known as satellite cells - residing outside the sarcolemma, but beneath basal laminae of the basement membrane. These cells play an important role in muscle maintenance and regeneration and are discussed in detail later (see Section 1.3).

1.2.1.2 Connective tissue

A series of connective tissue layers give the muscle the structure and organisation it needs to fulfil its functional requirements. A thin layer of areolar connective tissue -the endomysium - encloses each myofibre, but allows the entry of blood capillaries and nerve fibres. A thicker sheath of connective tissue - the perimysium - groups between 100-200 individual myofibres together into bundles called fascicles[11]. Yet another layer of thick connective tissue - the epimysium - encases the entire muscle and projects inwards, creating compartments of fascicles[3]. The epimysium is continuous with the extra-cellular connective-tissue matrix, known as the myofascia[33], which separates the muscle from adjacent muscles. This 'bundle-within-a-bundle' arrangement is depicted in Figure 1.1.

Skeletal muscle attaches itself to the corresponding bone structure with bundles of collagen fibres known as tendons[11,33].

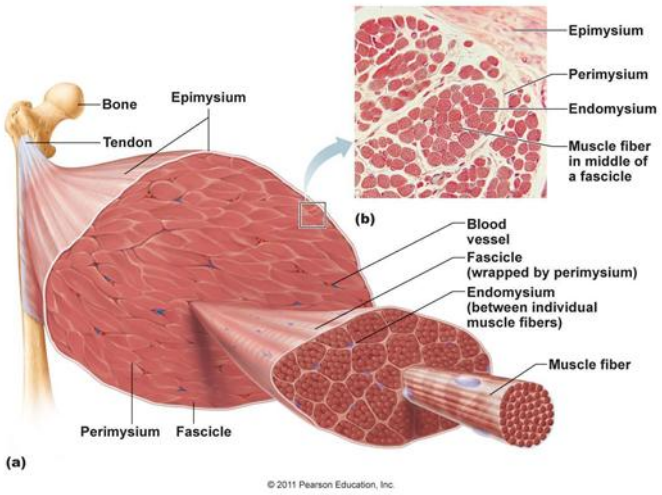

Figure 1.1 Structural organization of the skeletal muscle. This structure demonstrates a bundle-within-a-bundle type of organisation - from the muscle fibres to the fascicles grouped to form the entire muscle. [Copyright © 2011 Pearson Education, Inc.]

1.2.1.3 Vascularization

Skeletal muscle represents the largest component of the metabolically active cell mass of the body[35] and these high metabolic demands of the muscle tissue require extensive networks of blood capillaries to help maintain homeostasis within the muscle, especially during strenuous exercise[1].

Blood vessels transport oxygen and nutrients - essential for muscle metabolism and contraction - to the myofibres and waste material – such as heat and chemical products (e.g. lactate and carbon dioxide) - away from the myofibres[1]. Beyond their nutrient role, blood vessels transport the essential white blood cells (leukocytes, neutrophils, macrophages) to the muscle fibres. These cells fight infections and disease and assist in the major repair work that will be investigated in this study.

1.2.1.4 Innervation

As skeletal muscle is required for voluntary movements, rapid communication is essential and a highly organised level of innervation exists within the muscle tissue[27]. Motor neurons are muscle-specific nerves that innervate the myofibres. The term motor unit refers to a motor neuron and all the myofibres that it innervates. Hence each motor unit is able to contract singularly despite being made up of multiple fibres. The number of myofibres innervated by a single motor neuron varies between muscles (and even within the same muscle) based on the force requirements. For gross motor movements one motor neuron can innervate more myofibres, generally found in larger muscles, e.g. 20 myofibres innervated by one motor neuron in the *gluteus maximus*[27]. Smaller

muscles, requiring fine motor coordination, contain more motor units, innervating fewer myofibres per motor unit[33]. Some motor units consist of only one myofibre and its innervating motor neuron[33].

More motor units are activated in response to greater force production demands[33]. This enables the muscle to work as a unit while allowing for variation of force. Each myofibre receives an action potential from the neuron that sparks a complete contraction known as an all-or-nothing response. However, the number of fibres recruited for contraction increases according to the increased demand for force. This allows the perceived graded response as, for example, voluntarily recruiting 60% of one's muscle fibres is sufficient to generate about 60% of one's maximal force for that specific muscle.

The motor neuron branches into axon terminals to connect to each myofibre within the fascicle[33,27]. The myofibre requires a way to receive and respond to the impulses sent from the motor neuron. This gap is filled by a complex known as the neuromuscular junction (NMJ) (see Section 1.4).

1.3 Satellite cells

1.3.1 Introduction

Satellite cells (SCs) are widely known as the muscle's very own stem cells, whose function is to develop, maintain, repair and regenerate the myofibres on their journey from embryonic to mature muscle and thereafter[3,36,37]. Since myofibres are terminally differentiated[38], this SC reserve supplies the major source of additional deoxyribonucleic acids (DNA) needed for adaptations to the muscle during growth as well as in more drastic events.

1.3.2 Appearance, position and number

As mentioned earlier, SCs lie outside the myofibre, between the sarcolemma and the basal lamina[6,37,39,40] (see Figure 1.2) - in fact their name originates from this peripheral 'niche' position and its relation to the myofibre[36,38]. These cells are normally mitotically quiescent[36,37,41,42], but become activated, proliferate and differentiate in response to a variety of stimuli[3,41].

In early post-natal stages, the SC content of mouse muscle comprises ~30-35% of its total number of sub-laminal plus sub-sarcolemmal nuclei[37]. Undifferentiated, mono-nucleated quiescent SCs comprise a high nuclear-to-cytoplasmic volume ratio[41]. Activated SCs increase in cytoplasmic volume; display fine granulation and microfilaments within their cytoplasm; and develop abundant rough endoplasmic reticulum as well as some rounded mitochondria[41]. Once differentiated, these

SCs lend themselves to the formation of muscle tissue - termed myogenesis - of the developing myofibres as they lengthen and increase in diameter.

SCs contribute additional cytoplasmic mass and valuable nuclei to the growing myofibres. The added nuclei empower the myofibre to increase protein synthesis necessary for structural components and regulatory molecules for rapid and effective communication and myogenesis. As the muscle matures, the number of myonuclei increases and SC numbers diminish to a proportion of between 1 - 6 % of total sub-laminal nuclei [3,37,40,42,43]. (Percentages may differ according to different types of muscles, muscle fibre types (slow- or fast-twitch) and even between species. Nevertheless, SCs are present in all muscle fibre types with slow-twitch muscle fibres having generally more SCs than fast-twitch muscle fibres[3].

Concerning differences in muscle fibre types, Mackay *et al.* 2009 counted more SCs in Slow Type I myofibres (mean 0.070 ± 0.24 per 100 myofibres) compared to Type II (mean 0.066 ± 0.30 per 100 myofibres) although no comparison was made between the two to determine whether differences were significant[40].

SC number in myofibres can vary with circumstances and two most commonly occurring factors affecting SC number are aging (decreases SC number) and exercise (increases SC number). Shefer *et al.* (2010) describe means for SC number in isolated fibres of the *gastrocnemius* muscle - the muscle focused on in our study – in sedentary male rats[42]. They found 24 ± 2 SC nuclei in young male rats (age: 3.5 months) and a diminished 8 ± 1 SC nuclei in old male rates (age: 15 - 17 months)[42]. In the same study, rats put on an exercise regime for 20 minutes of running, 6 days a week, for 13 weeks boasted increased means of 30 ± 2 and 15 ± 2 SCs/fibre in young and old male rats respectively[42].

Different muscle types distribute their SCs in various patterns, i.e. in the slow twitch Type I muscle - the soleus - SCs amass around the middle, localizing around the motor end-plate of the innervating motor neuron, while SC's on the fast twitch Type II muscles - the *tibialis anterior* and the extensor *digitorium longus* - seem scattered randomly along the length of the myofibre[36].

1.3.3 Physiology

In adult muscle, under normal circumstances, SCs mostly remain mitotically quiescent[36,37,44], but are activated in events that compromise the muscle's homeostasis such as the stimuli for hypertrophy, repair and regeneration[14,38,43,44] (see Figure 1.2). Events resulting in myotrauma include: exercise (micro-damage), weight-bearing and mechanical stretch, wounds such as burns or lacerations, myodegenerative diseases and - in light of this study - contusion injuries[37,38,44]. Upon activation, SCs will proliferate and generate myoblasts – defined as such when the SC expresses myogenic

proteins[41]. Once SCs have differentiated into myonuclei, they fuse to form myotubes for new myofibres or repair existing myofibres[44,45] (see Figure 1.2). This contributes to the growth and repair of the muscle fibres.

The magnitude and rate of SC response differs according to the incidence and severity of the damage, i.e. low in maintaining homeostasis and stretching and high in large-scale damage that requires muscle regeneration. SCs are activated within a few hours of activity/damage - with rat myoblasts expressing myogenin with 8 hours[37,46] - and proliferation is highest within the first 12 – 48 hours[36,40,46].

The proportion of activated SC numbers is low in resting muscle – mean 0.5 % in human *gastrocnemius medialis* muscle biopsies taken in resting conditions[40]. Increases in response to e.g. electrical stimulation are high and rapid (mean 10 %; 48 hours after stimulation) whereas responses to exercise are less: resistance training, where 12 weeks of low resistance training showed a higher proportion of activated SCs (mean 2.5 %) in comparison to the same period of high resistance training (mean 1.4%)[40].

SC proliferation sustains the quiescent SC pool. Most SCs undergo at least one division *in vivo* before committing to terminal differentiation[37]. This allows myofibres to continue regenerating effectively in response to repeated damage – Sadeh *et al.* (1985) tracked effective regeneration up to 50 repeated cycles following extensive injury using myotoxins[47]. Even without such damage, there is a baseline myonuclei turnover within the myofibre (1 – 2 % per week in rodent studies)[37].

SCs can proliferate rapidly and extensively in response to injury. In early studies, Studitsky (1964) removed rodent muscle fibres, minced these fibres and replaced muscles them into the animal, after which they witnessed complete *in vivo* transformation into new functional muscle[48]. Zammit *et al.* revealed instances where 3 - 5.5 % SCs on an isolated and ablated myofibre needed only 4-5 days *in vitro* to expand in number and wholly replace that myofibre's myonuclei[49].

1.3.4 Satellite cell transcription factors

SCs activation, proliferation and differentiation are regulated by a number of transcription factors[41]. The main factors are briefly introduced below:

A. *Pax7* – is a satellite cell-specific transcription factor and is expressed in activated and proliferating SCs[41]. Pax7 is also a key regulator for satellite cell pool maintenance in the postnatal period[36]. Pax7 activates another group of transcription factors – the MRFs (see below).

The myogenic regulatory factors (MRFs) – are a family of muscle-specific helix–loop–helix transcription factors that are responsible for activating genes involved in muscle differentiation and comprise Myf5, MyoD, Mrf4, and myogenin[3,5031,36,38,41].

B. Myf5 - expression is upregulated first, for SC quiescence to activation , and in turn activates

C. MyoD - expressed upon SC activation and proliferation

D. MRF4 – SC differentiation

E. Myogenin - expression is upregulated in differentiated SCs that are fusing into myotubes and undergoing myotube maturation

Analysis of the expression of these transcription factors allows one to determine the state in which the detected SC is found.

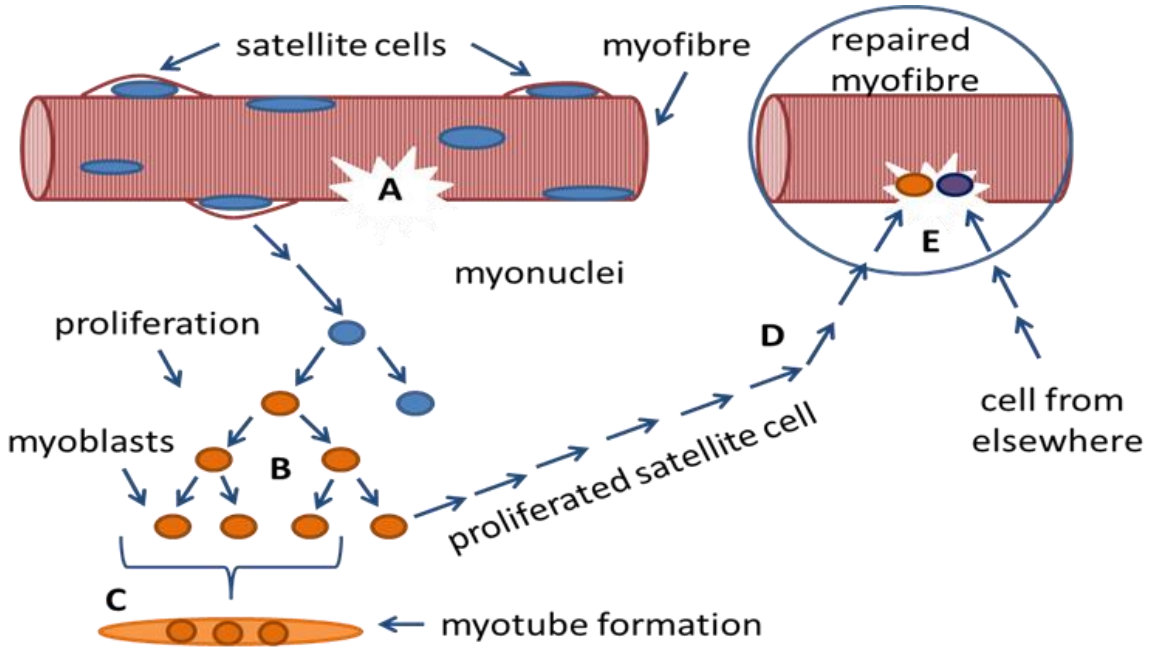

Figure 1.2 Satellite cell quiescent position and activity following myofibre damage. SCs lie between the sarcolemma and the basal lamina on the myofibre. Upon damage (A) myofibre sends signals that trigger SC activation. SCs replicate (B) to form one new dormant cell and one proliferating cell. Proliferated daughter SCs either form new myofibres (C) or repair the damage on the original fibre (D). Cells from elsewhere (e.g. bone marrow stem cells) may also assist in myofibre repair (E). (Adapted from http://www.life-enhancement.com/images/LEM1407satellite-cells548.gif)

1.4 The Neuromuscular Junction

1.4.1 Introduction

The neuromuscular junction (NMJ) encompasses the synapse between the motor neuron and the outer sarcolemma of its innervated skeletal muscle fibre[25,26] and enables communication between the two structures – thus providing the final crucial link between the peripheral nervous system and muscle action. The complex structural and signalling network of the NMJ ensures highly reliable neuromuscular signal transmission[25].

1.4.2 Basic location and structure

The neuromuscular junction can be separated into 3 parts:

Presynaptic – the motor nerve terminal branches that end in enlarged synaptic knobs or terminal bouton. This motor nerve terminal packages the neurotransmitter, acetylcholine (ACh), into synaptic vesicles[25] that are released into the synaptic cleft upon motor axon depolarization. *In vitro* studies have shown that other nerve derived factors exert regulatory roles on post-synaptic structures[51], such as neural agrin and neuregulin which play roles in the production and organization of the postsynaptic receptors[25,51].

Intrasynaptic – the synaptic basal lamina comprises an extra-cellular matrix, providing structural support to the sarcolemma as well as facilitating the organization of the post-synaptic membrane[25].

Postsynaptic – refers to the sub-synaptic area of the sarcolemma where nerve signals/impulses are received, known as the motor end-plate[25]. This specialized part of the sarcolemma incorporates a dense area of nicotinic acetylcholine receptors (AChR) and other signaling proteins such as low-density lipoprotein receptor-related protein 4 (Lrp4), muscle specific tyrosine kinase (MuSK), downstream of kinase 7 (Dok7), ErbB and Rapsyn[25]. These molecules are necessary for the establishment and proper functioning and maintenance of the motor end-plate and are discussed further in Sections 1.4.4 and 1.4.5.

To cater for the several twisting branches of the axon terminals, each end-plate creates a network of stabilizing invaginations, known as junctional folds[26]. This explains the exquisite coral-like structure of the typical motor end-plate henceforth referred to as the NMJ (see Figure 1.3).

1.4.3 Basic functioning of the neuromuscular junction: from impulse to contraction

The innervating motor neuron initiates the entire NMJ interaction through its chemo-electrical transmission of the action potential (AP).

In the motor neuron, choline acetyltransferase (ChAT) synthesizes acetylcholine (ACh)[25], which is packaged into presynaptic vesicles and stored in the synaptic knob. The arrival of an AP causes the voltage-gated calcium channels (VGCC) to open and extracellular calcium (Ca^{2+}) streams into the motor nerve terminal[25]. This Ca^{2+} influx triggers the release of ACh by the presynaptic vesicles moving towards and merging with the presynaptic membrane. This releases the ACh, through exocytosis, out of the vesicle and nerve terminal and into the synaptic cleft.

Acetylcholine receptors (AChR) are expressed on the surface of the motor end-plate. Morphology of the AChR is discussed in detail in Section 1.4.5. ACh diffuses over the synaptic basal lamina and binds to AChRs[25]. This binding generates an end-plate potential[26]. The AChR opens via a conformational change of its subunits[52], increasing the cell's permeability by inducing the opening of voltage-gated sodium channels (VGSC). The resultant influx of sodium and other cations depolarizes the sarcolemma to the extent where its threshold of -55mV is exceeded, thus continuing the neural action potential into the post-synaptic myofibre as it spreads along the sarcolemma[25,52].

After exerting its effect, ACh is hydrolyzed by acetylcholinesterase (AChE)[25], ensuring that its influence upon the AChR is limited, preventing prolonged contractions and liberating the receptor for ACh binding when the next AP is transferred.

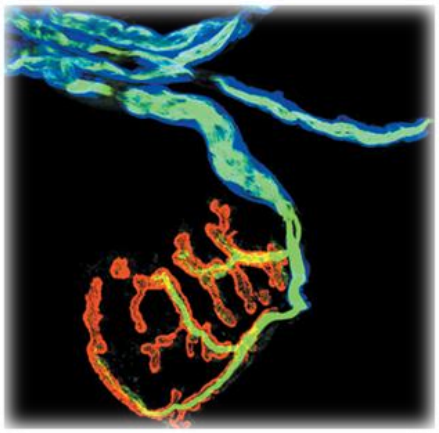

Figure 1.3 Axon (green) covered in a myelin sheath (blue) innervating the NMJ (red). From Court *et al.* (2008).

1.4.4 Associated structural and signalling molecules

1.4.4.1 Introduction

The NMJ consists of many structural and signaling components that interact and ensure the proper development and functioning of this vital communicative complex. The components that will be discussed here are all part of postsynaptic structural apparatuses and transverse the basal lamina of the myofibre[25]. These postsynaptic components are introduced in order of their coordinating signaling molecules, receptors and downstream targets (see Figure 1.4).

1.4.4.2 Acetylcholine and its receptor

Acetylcholine (ACh)

Aside from its pivotal role in signal transmission, ACh release from the nerve terminal during early development aids in 'selecting' the AChR cluster that will form a particular NMJ[25]. With the onset of neuronal activity AChR clusters that have formed spontaneously but lack agrin stabilization are dispersed[25].

Acetylcholine Receptors (AChR)

The AChR receives the ACh molecule and continues the transmission of the AP from the motor neuron to the myofibre. AChRs are the focus of this study and are discussed in detail in Section 1.4.5.

1.4.4.3 The neural agrin/Lrp4/MuSK/Dok7 signalling pathway

Neural Agrin

Neural agrin is an extracellular matrix molecule that plays a major role in the assembly of the postsynaptic apparatus through initiation of the neural agrin/Lrp4/MuSK/Dok7 signaling pathway[25]. Neural agrin pre-aggregates the AChRs opposite the nerve terminals ensuring correct organization of the motor-end plate during development as well as for maintenance in adulthood[25]. *In vitro* studies have demonstrated agrin's role in the organization of AChRs and other postsynaptic proteins into aggregates, without immediately enhancing AChR production[51].

Lipoprotein receptor-related protein 4 (Lrp4)

Neural agrin binds to Lrp4 which initiates activation of the downstream signaling pathways via MuSK and also plays a role in ensuring stabilization of the AChRs[25].

Muscle-specific receptor tyrosine kinase (MuSK)

Muscle-specific receptor tyrosine kinase (MuSK) is a key protein that orchestrates AChR pre-aggregation in the center of the developing muscle prior to innervation. This 'pre-patterning' of the uninnervated postsynaptic apparatus relies on ligand-independent activation of MuSK[25]. Ligand-dependent roles of MuSK include AChR clustering at the motor end plate and differentiation of the NMJ[25]. Upon activation, MuSK and its downstream signaling processes reorganize the actin cytoskeleton, phosphorylate the AChR β-subunit and recruit AChRs into stable clusters[12]. Along with AChR clustering, MuSK plays roles in the differentiation of the NMJ as seen in MuSK mutant mice which fail to form NMJs[31]. However, AChR clustering and NMJ formation can be restored post natally following the introduction of MuSK[31].

Downstream of kinase 7 (Dok7)

The binding of Dok7 plays a role in the aggregation of AChRs and bridges the activation of MuSK to downstream signalling pathways[25].

The Pathway

Upon secretion, neural agrin binds to laminin (specifically laminin-221) in order to incorporate itself stably into the synaptic basal lamina[25]. Its C-terminal binds to low-density lipoprotein receptor-related protein 4 (Lrp4) which activates the phosphorylation of muscle specific tyrosine kinase (MuSK), allowing for the binding of downstream of kinase 7 (Dok7)[25] and of the adaptor protein, rapsyn (see Postsynaptic components and Figure 1.4). The agrin/Lrp4/MuSK/Dok7 signalling complex has a major role in stabilization of the postsynaptic AChRs, - giving them a superior stability despite metabolic activity when compared to non-synaptic counterparts[25].

Neurotrypsin

Neurotrypsin is a protease that targets neural agrin, cleaving it at two sites and thus rendering the agrin inactive[25]. This leads to the disassembly of the entire junctional complex.

1.4.4.4 Other anchoring components

Rapsyn

Rapsyn stabilizes AChR clusters by binding to dystroglycan, mediating its binding to the f-actin cytoskeleton[25]. Rapsyn mutations can result in congenital myasthenia in humans indicating the continual role of rapsyn beyond developmental stages and well into adult life and during aging[25].

Dystroglycan

Dystroglycan plays an anchoring role, binding the AChRs, Lrp4 and ErbB receptors to the f-actin cytoskeleton and also to laminins, e.g. laminin-22124.

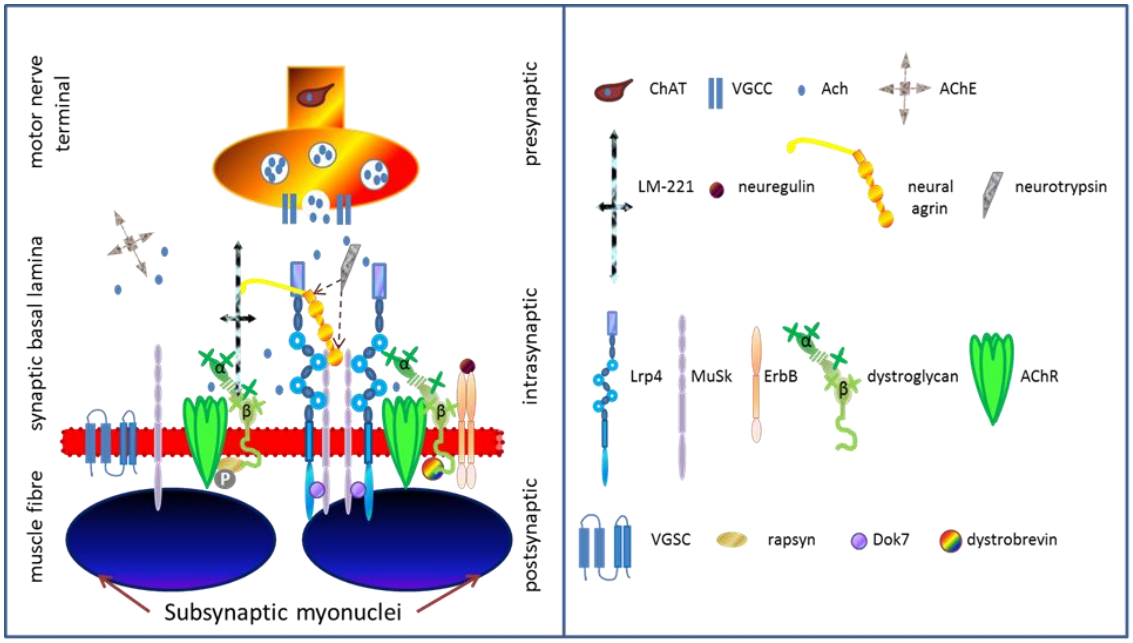

Figure 1.4 Structural and signalling components of the NMJ. Choline acetyltransferase (ChAT) synthesizes neurotransmitter, acetylcholine (ACh) which is packaged into presynaptic vesicles. Arriving action potentials (AP) open voltage gated calcium channels (VGCC) and the resultant influx of Ca^{2+} triggers the release of ACh into the synapse. ACh binds to the AChRs which open the voltage gated sodium channels (VGSC) generating an AP in the postsynaptic myofibre thus continuing the signal. Acetylcholine esterase (AChE) subsequently hydrolyses ACh. During development, neural agrin is secreted from the nerve terminal and anchors the postsynaptic apparatuses by binding to 1) laminin-221 (LM-221) for stable incorporation into the basal lamina and 2) to lipoprotein receptor-related protein4 (Lrp4) which phosphorylates muscle specific tyrosine kinase (MuSK), allowing MuSKs binding to downstream of kinase 7 (Dok7). This agrin/Lrp4/MuSK/Dok7 downstream signalling pathway is responsible for AChR aggregation at the NMJ. Neurotrypsin cleaves agrin which renders it inactive and results in the disassembly of the entire NMJ complex. Rapsyn plays a necessary anchoring role for the AChRs by binding to dystroglycan – mediating binding to the f-actin cytoskeleton. Dystroglycan in turn binds to laminins, further securing the postsynaptic AChRs. Nerve secreted neuregulin binds to Erb Receptor tyrosine kinases (ErbB) initiating the phosphorylation of α-dystrobrevin to recycle AChRs at the adult NMJ. Adapted from Punga *et al.* 2012.

1.5 Acetylcholine receptors

1.5.1 Introduction

Acetylcholine receptors (AChR) are ligand-activated cholinergic receptors – activated by the neurotransmitter AChR – and are present throughout the body, expressed by both neuronal and non-neuronal cells [53]. They are classified into two major subtypes.

The muscarinic acetylcholine receptor (mAChR) are metabotropic receptors present as second messenger, G protein-coupled seven-transmembrane proteins[53]. They are named according to their sensitivity to muscarine (a toxin from the mushroom *Amanita muscaria*) and experience relatively slow activation (milliseconds to seconds) in comparison with their nicotinic counterparts[53].

The nicotinic acetylcholine receptor (referred to as nAChR or AChR, the latter abbreviation is used throughout this study to describe nicotinic AChRs) are ionotropic cationic receptors linking directly to ion channels and without the involvement of a second messenger[53,54]. They are named according to their sensitivity to nicotine and are fast reacting (activated within micro- to sub-micro seconds). The AChRs are the focus of this study.

AChRs are broadly classified into two subtypes: neuronal- and muscle type. Their classification is determined by the combination of AChR subunits making up the specific receptor.

1.5.2 AChR subunits

Seventeen different AChR subunits exist, all homologous, but genetically distinct[52,53] (see Table 1.1). Each subunit comprises four transmembrane domains with both the N- and C-terminus located extracellularly[8] (see Figure 1.5).

Table 1.1 *AChR subtypes*

Neuronal type					Muscle type
I	II	III			IV
		1	2	3	
α_9, α_{10}	α_7, α_8	α_2, α_3, α_4, α_6	B_2, β_4	α_5, β_3	α_1, β_1, δ, γ, ε

Five subunits are arranged symmetrically around a central pore to form the AChR pentamere (280kDa)[54,55]. AChRs in the brain and autonomic ganglia consist of only α-type subunits or α- and β-type subunits. In mammalian muscle-type AChRs express α-1, β-1, δ, γ (fetal) and ε (adult)

subunits[52,53,56]. Of these five different subunits, two combinations are possible for the creation of a functional AChR heteropentamere, in a ratio of 2:1:1:1[52,53].

The first type of subunit is the fetal AChR (AChR-γ), which consists of two α-1 subunits and one β-, δ- and γ- subunit (α2βγδ). The second type of subunit is the adult AChRs (AChR-ε), consisting of two α-1 subunits and one β-, δ- and ε- subunit (α2βεδ).

The different roles of AChR-γ and AChR-ε are discussed in Section 1.4.6 and 1.4.7.

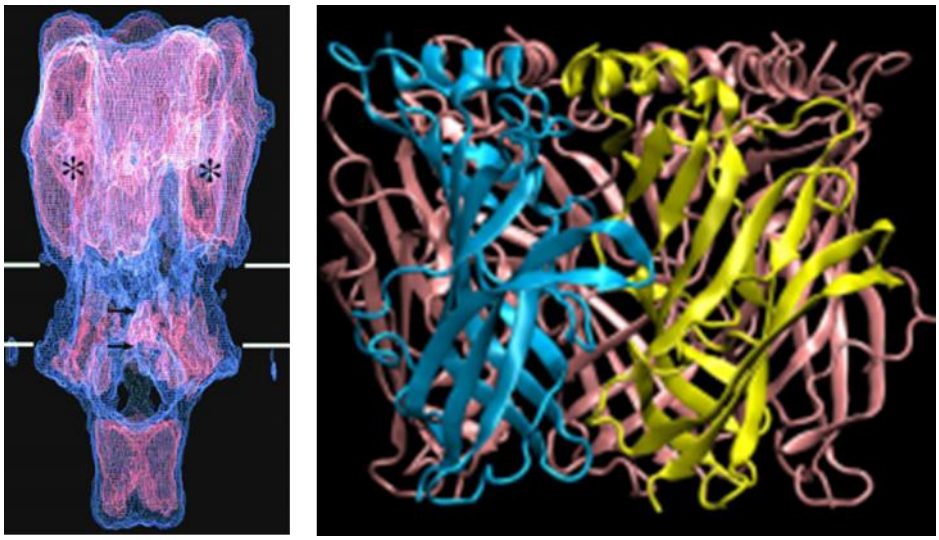

Figure 1.5 AChR atomic structure showing cryo-electron microscopy of an AChR. From the *Torpedo* electric organ at A) 9Å resolution and B) 4Å resolution. From Sine, 2012.

1.5.3 AChR numbers and distribution

The fusion of myoblasts into myotubes activates synaptic genes that produce AChRs along with the many other sub-synaptic proteins. AChR subunits are assembled into pentameres and inserted into the myotube membrane[51]. This initial production creates densities of ~1000 AChR/μm^2 (measured in rodent studies)[51], although some AChRs aggregate into higher density clusters termed 'hot spots'.

Muscle type AChRs are also categorized by their location along the myofibre. Synaptic AChRs are located directly beneath the synaptic knob, i.e. form part of the NMJ. These AChRs occupy about 0.1 - 1% of the total sacrolemmal surface[25,57]. AChRs in this region are densely packed into clusters of 10 000 – 20 000/μm^2) and assume a coral-like formation for optimal receiving ability[12,51]. Furthermore, post-synaptic AChRs are metabolically much more stable than their non-synaptic counter parts[25].

Subsynaptic myonuclei in both developing and mature muscle are known to transcribe AChR genes at higher rates in comparison with non-synaptic myonuclei[58].

Non-synaptic AChRs are located all along the other 99% of the sarcolemma (i.e. do not form part of the NMJ) at a greatly decreased negligible density of <10/µm[251].

As mentioned earlier, the motor neuron plays a major role in controlling the abundance, subunit composition and localization of AChRs in the myofibre[56] by the release of neurogenic factors as well as through its signal transduction that induces electrical activity in the myofibre[56].

1.5.4 Development of the neuromuscular junction through AChR production and aggregation

The development of the neuromuscular junction is a multi-faceted process, directed by both the myofibre and the motor neuron. Two paradigms exist concerning this development.

The traditional view edicts that the axon growing towards the myofibre releases neural stimuli[51]. This stimulus, namely neural agrin, is released into the extracellular matrix and prompts the aggregation of AChRs towards the sarcolemmal area immediately below the nerve terminal[25]. The motor neuron ignores pre-existing 'hot spots' and creates its own new clusters of AChRs along a central 'end-plate' band[51]. These spontaneous 'hot spots' subsequently disappear and the neural AChRs proceed to mold themselves in an intricate coral-like branches to surround the infiltrating branches of the nerve terminal[51].

The paradigm challenging the traditional view proposes that the axon is attracted to the muscle-produced cluster sites of AChRs and by this attraction, associated NMJs are formed[51]. The neuron then incorporates some of these aneural 'hot spots' into its NMJ design, remodeling innervated clusters to align accordingly[51]. This idea suggests that the muscle pre-patterns the area of NMJ formation to some extent and is supported by observing aneural AChRs arranging themselves into similar coral-like formations without any innervation[51].

NMJs of different muscles vary in their shape, size and distribution, as well as in their metabolism, physiology and gene expression. Two distinct patterns of NMJ formation have been defined, with regards to how AChR clusters are formed[25]:

Fast Synapsing – a mature NMJ formation is complete within one day (e.g. *tibialis anterior* or *extensor digitorium longus*)

Delayed Synapsing – NMJ formation takes up to five days (e.g. *diaphragm* or *soleus*)

In the developmental stages, i.e. embryonic and early postnatal, AChR insertion is the dominant activity on the postsynaptic membrane, promoting the proper formation and growth of the NMJ[25]. New AChRs are synthesized and inserted into the post-synaptic region largely through local gene transcription from myonuclei situated directly underneath the NMJ (subsynaptic myonuclei)[25]. Neural agrin/Lrp4/MuSK/Dok7 signaling facilitates this localized transcription in addition to its stabilizing role resulting in the superior metabolic stability of synaptic AChRs to that of their non-synaptic counterparts[25].

At birth the immature NMJ appears as an amalgamated, formless entity, but is swiftly organized into junctional folds around the innervating motor neuron. By day 14 post natally, NMJs start to resemble the classic coral-like structure of a mature NMJ[59] (see Figure 1.6).

As the NMJ matures, the need arises for renewal of old and damaged AChRs, shifting focus away from the predominant insertion of new AChRs. These old AChRs are removed and either a) repaired and reinserted (a process termed 'recycling') or b) wholly replaced by newly synthesized AChRs[25]. Neuregulin, by its alternate signaling pathway - the neuregulin/ErbB/dystrobrevin signaling pathway - is closely linked to the recycling of old and damaged AChRs[25]. The concentrated collection of postsynaptic AChRs, maintained by their constant individual insertions and removal, caters for a functionally reliable complex, fully equipped with ample receptors for ACh and neurotransmission[25].

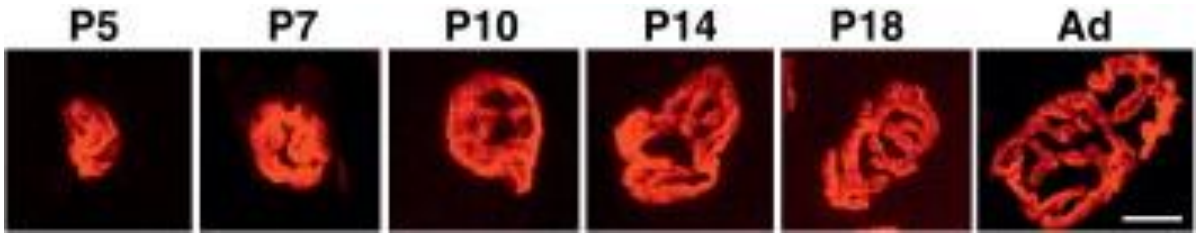

Figure 1.6 Development of the NMJ from 5 days postnatal (P5), through to adolescence (Ad). From Shi *et al*. 2012.

1.5.5 Transcriptional switch from fetal AChR-γ to adult AChR-ε

At birth, muscle expresses only the fetal AChR type (α2βγδ)[25,56], regulated by members of the MRF family of transcription factors[31]. During development, the AChR-γ subtype covers the sarcolemma and starts accumulating at the end-plate, as the nerve comes into contact with the myofibre[56]. AChR-α subunits follow the same pattern as AChR-γ subunits – with post-natal expression along the entire fibre and localization at the end-plate following innervation[56].

Increased post-natal innervation, as well as neural agrin and neuregulin secretion, gradually shifts AChR expression to the adult type (α2βεδ)[25,58], i.e. the γ-subunit is replaced by the ε-subunit, while

the α-, β- and δ-subunits are always present in both AChR types. MRF members are involved in this transcriptional change[31], indicating that it coincides with transcription of multiple muscle-specific proteins during myotube differentiation. These adult AChRs localize around the motor end-plate to create the mature NMJ[25,56]. Interestingly, in Witzemann *et al.*, the appearance of adult AChRs immediately after birth was not restricted by experimental denervation – suggesting the existence of other control mechanisms for gene activation in the myofibre itself[56].

The adult AChR is functionally superior to the fetal type with a longer end-plate channel opening mean time and better conductivity (i.e. a larger voltage)[25]. As AChR-ε subtype levels increase and AChR-γ subtype levels subsequently disappear - this is referred to as the AChR subunit switch in maturing (and regenerating) muscle[56].

1.6 NMJ Injury Models

1.6.1 Introduction

Neuromuscular injury (an injury to the nerve or muscle which affects neuromuscular transmission) is noticeable by a decrease in voluntary function. Functional assessments (e.g. by determining sciatic functional index (SFI); muscle force and power production etc.) show a decrease in muscle reactivity and function following injury with a return to normal function over time[27]. This recovery in function results from regeneration of both the muscle and the nerve, directed at themselves; one another; and the interface, the NMJ.

Although well established and constant in their operations/activity, NMJ's show remarkable plasticity after damage to the muscle or nerve and are able to reform and restore themselves to continue in their vital communicative role[26,31]. Models of denervation have frequently been used to simulate neural injury and lack of synaptic communication at the NMJ, while botulinum toxin (BoTX) injection prevents Ach binding to its receptor, thus also preventing proper synaptic communication.

Literature focusing on NMJ injury and regeneration use a variety of different *in vivo* models to induce injury (See Table 2.1 on Nerve Injuries):

A. *Nerve transection* - an incision is made in the skin covering the target area and the specific nerve (most commonly, the sciatic nerve) is located and carefully lifted from the tissue. The nerve is cut with a fine pair of scissors or a sharp scalpel. This destroys the presynaptic nerve terminal and affects both the neuron and the subsynaptic structures that rely on neural stimulation and/or secreted regulatory factors for maintenance[12,56,60,61].

B. *Surgical excision* - an incision is made in the skin covering the target area, any muscle covering nerve may be bluntly split (the gluteal muscle to expose sciatic nerve in proximal part of the thigh (P9)) and the specific neuron is located and carefully lifted from the tissue. Magnification is required for studies involving small rodents. A section of the nerve (ranging from 2 – 30 mm) is excised with fine scissors or a sharp scalpel. Nerve resection completely prevents reinnervation[12,31,60,62,63].

C. *Nerve crush* – a direct crush is performed on the innervating nerve. An incision is made in the skin covering the target area, any muscle covering nerve may be bluntly split (e.g. biceps femoris to expose the sciatic nerve[27] and the specific nerve is located and carefully lifted from the tissue. Magnification is required for studies involving small rodents. The nerve is crushed using fine-tipped forceps. This technique allows one to injure only the nerve and focuses on the degradation and regeneration of this nerve as well as the effects of the lack of neural simulation on its targeted muscle and the deinnervated neuromuscular junction structures[27,28,64].

D. *Chronic nerve compression***–** induces damage to motor neurons (chronic nerve compression injury induces a robust Schwann cell response with axonal sprouting, but without morphologic evidence of axonal injury)[65].

E. *Eccentric exercise* – target muscle is subjected to multiple lengthening contractions[26].

F. *Injection of a neuro-toxic substance* – targeted area is injected with a neurotoxin (e.g. botullinum toxin). This technique maintains the structural integrity of the nerve terminal, but interrupts neuromuscular transmission. While the method is simple, any additional effects resulting from the introduction of a foreign substance can confound findings[29–31,56,66].

G. *Chronic administration of a pharmacological substance* – substances delivered via mini-osmotic pumps either 1) throughout the body or 2) a targeted area (e.g. the sciatic nerve) via sterile silicone rubber tubing threaded under the skin ending in a silastic cuff that can be placed around the sciatic nerve[56].

1.6.2 Effect of denervation on AChR subunit transcription

In the event of denervation, AChR-γ is again expressed along the entire fibre, until reinnervation once more replaces the fetal type with AChR-ε[56]. However, ε-subunits remain fairly constant in numbers and accumulation at the end-plate, even in the absence of the nerve and electrical stimulation[56]. Interpretation of results should take into account the mechanism for lack of NMJ

function, the time course of sampling following the injury, and whether or not a modality was used to promote re-innervation.

In a study involving various methods of chronic denervation, a 30-50 fold increase in α- and δ-subunit mRNA as well as a strong relative increase in γ-subunit mRNA were seen[56]. Lesser increases were seen in β- and ε-subunits[56]. Therefore, loss of function is shown to increase sub-unit mRNA expression. When muscle was subjected to electrical stimulation following denervation, northern blot analysis showed a strong reduction in the α-, γ- and δ-subunits, whereas the ß-subunit mRNAs displayed a much smaller decrease and ε-subunit mRNA remained unchanged corresponding with their lesser changes in the denervation phase[56].

Ma *et al.* compared models: a single intramuscular injection of botulinum toxin (BoTX) in the *gastrocnemius* muscle vs. transecting the muscle's innervating tibial nerve[29,30]. Injured muscle was compared to either the saline-injected[30] or uninjured[29] contralateral leg which served as a control.

Most AChR subunits (α, γ, δ and ε) increased mRNA expression within the first week of denervation after which expression levels returned to normal by about 2 weeks. BoTX treatment influenced the number and distribution of AChRs in a similar manner to chronic denervation. However, BoTX was followed by axon sprouting facilitating the recovery of paralyzed end-plates through reinnervation[30].

In terms of a more detailed time course, AChR-α mRNA expression in BoTX injected muscles increased significantly at 3 days; peaked with a 15-fold increase at 7 days after injection and returned to normal by 15 days.[30,31] AChR-α mRNA expression in muscles from legs subjected to nerve transection showed the same pattern of increases at day 3 and peaking at day 7 although expression was still slightly elevated (but not significantly) by day 14 , returning to normal levels by day 30 indicating a longer recovery period[29].

AChR-γ mRNA followed the same pattern, but with a 50-fold increase at 7 days post injection[30]. In the nerve transection study, however, γ-subunit mRNA did not increase significantly by day 3 and showed only a 4-fold increase by day 7 – far more modest changes compared to the findings in the BoTX model[29]. This may explain the requirement for longer recovery if the initial response was diminished.

The AChR-ε subunit mRNA increased, but not significantly, at 3 days then peaked significantly at 7 days post injection (with a 3-fold increase) and also returned to normal levels by 15 days[30]. ε-Subunit mRNA after nerve transection followed the same pattern of increases and returned to normal by 14

days post injury[29]. Again the ε-subunit appears to be less affected, regardless of the model. The AChR-δ mRNA expression response was only slightly higher, peaking at 3 days following injection with only a 9-fold increase; it remained significantly higher at day 7 and gradually declined to control levels[30]. Nerve transected muscle showed a similar pattern[29]. The least affected in both models was the AChR-β subunit. No significant increases were detected in AChR-β subunit expression in the injected or nerve transected muscle throughout the duration of the study[29,30].

Table 1.2 Nerve Injury Models

Study	Species	Injury Type	Time points of Sacrifice	Other intervention	Analysis
Goldman et al.[62] **1988** ***Basel**	Sprague Dawley rats Male *Soleus*	Surgical excision (sciatic nerve, 5mm)	0, 5, 10, 20, 48- and 72 hours	Electrical stimulation (for 6 days)	mRNA: AChR subunits (α, β, δ, γ) (RNA blots; cDNA probes) Electrophysiological
Witzeman et al.[56] **1991** ***Basel**	Sprague-Dawley Rats *Triceps surae*, diaphragm, other muscles not specified	- Nerve transection (sciatic nerve) or - Pharmacological (*chronic/**single) • TTX* (sciatic nerve) • α-Btx* (soleus) • BoTX**(triceps surae) - Nerve crush (phrenic nerve)	7, 14, 30 days	Electrical stimulation (for 7 days) Or no intervention	mRNA: All AChR subunits (qPCR) *In situ* hybridization RNA protection assay Electrophysiological Northern Blots of total RNA Densitomertic (Audiogram)
Kues et al.[60] **1995** ***Basel**	Wistar and Sprague-Dawley rats, Adult *Soleus*	Surgical excision (sciatic nerve, 5mm) Chronic conduction block by TTX (sciatic nerve)	0, 1 ½ , 1, 3, 5, 7, 12, 14 days	Electrical stimulation (for 7 days or 5 days off/5 days on) Or no intervention	mRNA: All AChR subunits (qPCR) *In situ* hybridization Densitrometric evaluation
Gervasio et al.[12] **2007**	Female FVB mice 1 month post-natal *Tibialis anterior*	Surgical excision (sciatic nerve, 2-3mm) 2-3mm, sciatic nerve	0,1,4, 6, 7, 10 days	Electroporation	AChRs and Rapsyn (Confocal microscopy) FRET
Gigo-Benato et al.[64] **2010**	Wistar rats 3-month-old, Male *Tibialis anterior*	Sciatic nerve crush injury	3, 5, 7, 9, 11, 14 days	Electrical stimulation	NCAM and Neurofilament (Light microscopy) Electrical & Motor function evaluation
Pinter et al.[67] **2003**	Wistar rats Adult, Male *Soleus*	Surgical excision (sciatic nerve, 30mm) with/without Nerve reconstruction: • Autologous nerve graft • Suture	1, 3, 5, 7, 10, 21, 28, 35 days	Intramuscular notexin injection (total muscle necrosis and nerve regeneration)	H&E AChE activity Standard electron microscopy (EM)

Magill et al.[27] **2007**	Homozygous thy1-YFP mice *Tibialis anterior*	Nerve crush (sciatic nerve)	1, 2, 3, 4, 6 weeks	None	Axon, Schwaan cell, AChR (Whole mount confocal microscopy) Walking track analysis
Ma *et al.* [30] **2005 **Winston-Salem**	Sprague–Dawley rats 1 month old, Male *Gastrocnemius*	Local Botox injection (*gastrocnemius*)	3, 7, 15, 30 , 90, 180 and 360 days †2 weeks, 2 & 6 months and 1 year	None †removal of muscle segment	mRNA: All AChR subunits (qPCR) †AChR (Confocal microscopy)
Shen *et al.* [31] **2006 **Winston Salem**	Sprague–Dawley rats 1 month old, Male *Gastrocnemius*	Local Botox injection (*gastrocnemius*)	3, 7, 14, 30 , 90, 180 and 360 days	None	mRNA: α-AChR subunit; MuSK; myogenin; MRF4; IGF-1 and P21 (qPCR)
Ma *et al.* [29] **2007 **Winston Salem**	Sprague–Dawley rats 1 month old, Male *Gastrocnemius*	Nerve transection (tibial nerve)	3, 7, 14, 30 , 90, 180 and 360 days	None	All AChR subunits (qPCR)
*** and ** indicate experiments were done in the same lab (* The Physiological Institute of Basel University and ** Department of Orthopaedic Surgery, Wake Forest University Medical Center)**					

In summary, these findings outline the heavy dependence on the synthesis of fetal form of AChRs (with γ-subunit) within the initial phases of NMJ regeneration, with significant (nearly 10-fold) increases in mRNA expression by day 3 and very high increases by day 7 (50-fold), while the adult ε-subunit only started showing significant increases by day 7 with much lower fold-differences[30]. This seems to be the case for various muscles: A study involving the denervation of rat soleus muscle by excision of a portion of the sciatic nerve (Kues *et al.* 1995) revealed maximal levels of transcription for AChR ε−subunits' mRNA on day 5, specifically centrally in the muscle, where former synapses were located[60].

In a later multi-gene study by the same group, MRF mRNA expression analysis showed increases in certain MRFs following denervation by BoTX injection. At day 7 post-injury, AChR subunits α, δ and γ showed mRNA increases as expected[31] and MRF pro-differentiation genes, MRF4 and myogenin, had mRNA increases of more than 5- and 8-fold respectively.

Observing changes in MRFs over time, MRF4 increased drastically at 3 days post injection with further increase by 7 days and remained significantly higher than in the contralateral leg (which served as the uninjured control) by 14 days post injection[31]. Myogenin mRNA increased significantly from contralateral control leg at all time points up to 2 months (days 3, 7, 14, 30 and 60) with two peaks at day 7 and day 60 following injection [31]. No significant increases were seen in Myf5 and MyoD mRNA.

Furthermore, vital supporting NMJ component MuSK's mRNA increased, but not significantly, by day 3, then peaked with an over 8-fold increase at day 7 following injection. MuSK mRNA expression remained at significantly higher expression compared to the contralateral control leg when assessed at 2 weeks and even 1 month following injection[31]. This may support the theory of its less important structural role, but it also indicates that regeneration of a functional post-synaptic NMJ unit may take longer than would be expected if only AChR mRNA was investigated.

1.6.3 Relocation of AChR subunits

Apart from denervation, studies observing the effect of inactivity, ageing or absence of associated proteins and genetic disorders have all contributed to the understanding of AChR regeneration. Diseases that can affect the NMJ structure and functioning include diseases of the motor neuron (e.g. amyotrophic lateral sclerosis[68]); the junction itself (e.g. congenital myasthenia or receptor mutations)[25,69]; and the muscle (e.g. muscle dystrophy[26]).

Congenital myasthenia directly targets the AChRs resulting in muscle weakness and fatigue[25]. There is a growing interest in understanding this neuromuscular condition and an increasing amount of novel information about AChRs can be gleaned from these studies. Using techniques other than those focussing on gene transcription has yielded more information about changes in morphology. Several studies indicate that NMJ morphology is altered in dystrophic skeletal muscle[26], although, again, most studies have used denervation models.

1.6.4 Effect of denervation and disease on NMJ morphology

In normal uninjured muscle, each end-plate is innervated by a single axon. Magill *et al.* (2008) showed the degeneration/regeneration relationship between the innervating axons and their motor end-plates in the *tibialis anterior* muscle of mice subjected to sciatic nerve denervation[27]. Confocal microscopy showed denervation of all end-plates at one week following injury. At 14 days following injury, partial reinnervation had occurred and observations at 21 and 28 days saw the hyper-innervation of end-plates – with instances of more than one axon per end-plate. By 42 days, the relationship between axon and end-plate was restored to the 1:1 ratio seen in normal muscle.

However, this study did not note the number of end-plates present or assess the level of structural disorganization of the end-plates that lost their neural stimuli.

Ma *et al.* (2005) saw no influence on NMJ morphology of the *gastrocnemius* muscle (assessed by surface area and gutter depth of junctional folds) from denervation by BoTX A injection at 14 days after the intervention[30]. While NMJs became larger as the mice matured over 30 days, at 60 days after BoTX injection the gutter depth was significantly reduced in comparison to the saline injected contralateral leg which served as the control[30]. This denervation effect diminished over time and by 6 months, gutter depth of the injured *gastrocnemius* returned to near-control levels. At 360 days post injection NMJ gutter depth in control and experimental muscles was uniform again.

Hirata *et al.* (2005) reports the complete loss of accumulated AChRs in muscle 1 day after denervation by an injection of bupivacaine[14].

Pratt *et al*. (2014) depicted the morphological changes in the NMJ in intact, dystrophic and lengthening injured WT mice[26] where NMJs of dystrophic mice lack organization and were far more vulnerable to injury, losing what little organization they had and clumping into islands (see Figure 1.7).

Schmidt *et al*. (2011) observed a loss of synaptic branches in ErbB mutant mice with AChRs developing perforations – seen by presence of AChE activity in areas with no positively stained AChR[69]. This study created 3D images by means of combining confocal image stacks.

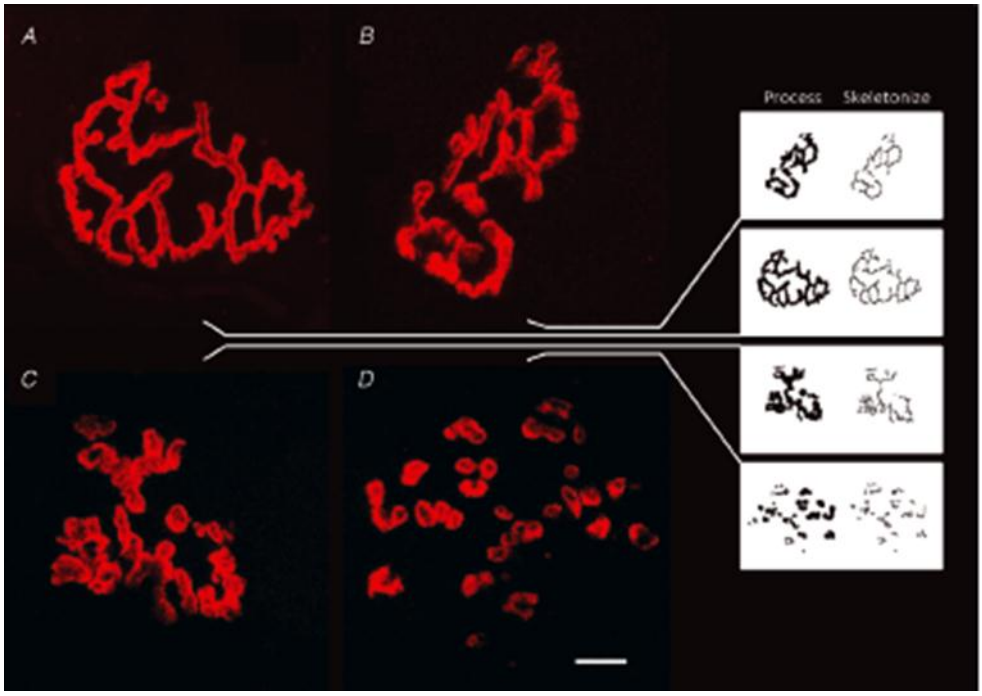

Figure 1.7 NMJ morphology of normal (wild type) mice (A, B) and dystrophic (mdx)mice (C, D) in uninjured *quadriceps* muscle (A, C) and *quadriceps* after injury induced by lengthening contractions . Image from Pratt *et al.,* 2013.

1.7 The muscle contusion injury model

1.7.1 Definitions of different muscle injury models

In light of this study, additional injury models involving the muscle were investigated. As with nerve injury models, different categories of *in vivo*, mechanical muscular injuries also exist:

A. *Laceration* - a cut of any nature that severs muscle fibres

B. *Elongation* - caused when a muscle is stretched beyond its capacity – common in activities demanding eccentric contractions[26]. Certain muscle fibres can also become torn in this manner

C. *Strain* - caused when intense and rapid contraction is demanded of a muscle. Such contractions can be too strong for muscle fibres to resist

D. *Muscle denervation* – (same as in Nerve Injury models) is also used as an intervention for muscle damage and regeneration studies[43]

E. Muscle contusion injuries – can be classified as either invasive or non-invasive and include:

F. *Muscle crush* - a precise surgical procedure where the skin is incised and exposed muscle is clamped, for example between a pair of tweezers, and a pre-determined force is exerted onto the structure[60,70,71]

G. *Mass drop injury* - caused by impact from a blunt object onto the muscle. The limb containing the target muscle (either surgically exposed prior to injury or unexposed) is carefully positioned on a specially designed apparatus that causes a crushing blow to that area[3,46](see Figure 1.8)

Invasive contusion injury models (muscle crush or mass drop injury with exposed muscle) include the likelihood of local and systemic inflammatory responses to the surgery which may complicate findings. This model, however, would be appropriate for crush injuries occurring in workplace or car accidents when lacerations may indeed be present. In the arena of contact sports, the majority of impact injuries are non-invasive. Therefore this study uses the non-invasive mass drop injury model to assess muscle damage and regeneration which will henceforth be referred to as the muscle contusion injury.

1.7.2 Introduction

According to the American Journal of Sports Medicine, contusion and strain injuries make up approximately 90% of all muscle-related sports injuries[72]. Muscle contusion injuries result from events where a blunt non-penetrating object impacts on the skeletal muscle, crushing the local tissue[3]. Muscle groups in the arms, hands, legs, feet, and buttocks are most commonly affected[3], and contusion injuries are especially prevalent in the *quadriceps* and *gastrocnemius* muscle groups in the legs[73].

Contusion injury leads to a weakening of the muscle tissue's structural components therefore decreasing functional efficiency - to a greater or lesser degree depending on the extent of the injury. An injury sustained by skeletal muscle can also impair or alter bone healing and dictate the long term success of prosthesis, if the magnitude of the injury is such to include skeletal system damage[74].

Not only does a contusion injury cause mechanical damage to the muscle fibres, it can also rupture the surrounding capillaries and harm or restrict the motor neurons that innervate the impacted

muscles. These events lead to further complications such as blood pools in the area through the ruptured capillaries forming painful haematomas[3] and impaired neurons and associated structures result in ineffectual communication between the nerve and the muscle[25].

1.7.3 Muscle regeneration following contusion injury

Muscle tissue has developed remarkable ways of repairing itself, a process known as skeletal muscle regeneration. When a muscle is subjected to an injury it suffers disruption of fibre structures, decay of cellular structures and cell rupture. In response to these injuries debris is cleared (by immune cell activity) and the existing fibre/s are either rebuilt or new replacement fibres are generated. Satellite cells are key role players in these events providing additional nuclei and muscle protein synthetic potential to the cause. Extensive research tracks the activation and migration of these cells to injured sites[3,36–38,43,46,49,71,75,76].

1.7.4 Characteristics of the contusion injury jig

The muscle contusion injury model with a specified apparatus – the contusion injury jig – has previously been used by our research group. The jig was designed and produced by our engineering faculty[3,77] and met the criteria for use in rat models: The exact height was determined in order to generate a moderately severe contusion injury, without creating further complications such as limping or compartment syndrome[3]. Later, an adapted apparatus allowed for contusion studies in mouse models[77]. The adapted apparatus for mice was used in this study.

The specialized contusion injury jig consists of a narrow, cylindrical tube set on a heavy platform (see Figure 1.8 and 2.3). The design involves releasing a pin, holding up a small weight (35 g) from the desired height (ranging from 10 – 30 cm). This weight falls onto another weighted cylinder (4.5 mm^2), carefully positioned on the desired muscle, with a small circular platform (of same diameter) positioned under the muscle to ensure the desired impact without a momentum-derived movement of the lower limb[3,77].

1.7.5 Selection of muscle group

The majority of research for both neuromuscular components and satellite cells has utilized the *soleus*[19,60,62,67] the *tibialis anterior* [9,11–13,20,27,64,78,79] or the *gastrocnemius* muscle[10,29–31,40]. Given the nature of the contusion injury jig, the size and accessibility of the *gastrocnemius* muscle made it the prime choice for this investigation, without incurring complications such as bone damage.

Figure 1.8 The mass-drop contusion injury jig

1.7.6 Selection of Time points

For selecting relevant time points for AChR analyses, the literature employing nerve injury models was carefully considered (see Table 1.2).

Early studies selected sampling time points within hours of nerve injury (by a 5mm surgical excision of the sciatic nerve), e.g. Goldman *et al.* (1988) analysed mRNA expression of AChR subunits α, β, δ and γ (by RNA blotting) from male Sprague Dawley rats selected time points at 0, 5, 10, 48 and 72 hours post injury[62]. Later, the same research group (indicated with *) performed qPCR analysis of AChR subunit expression - with the addition of adult type ε-subunit – in time points that extended into several weeks post injury (7, 14 and 30 days)[56]. In this study, groups of male Sprague Dawley rats were subjected to various nerve injury models, namely: i) nerve transection; ii) chronic blockade of impulse conduction by tetrodotoxin (TTX); iii) chronic blockade of neuromuscular transmission by α-bungarotoxin (α-btx); iv) single injection of botulinum toxin (BoTX) or v) nerve crush.

Following on from these studies, Kues *et al.* (1995) from the same research group used a combination of time points from the previous studies, performing similar qPCR analysis on various days focussing on more early time points: 0, 1 ½, 3, 5, 7, 12 and 14 days post injury. Both male Sprague Dawley and Wistar rats were used and were subjected to nerve injury either by surgical excision (5 mm) of the sciatic nerve or chronic conduction block to the sciatic nerve by TTX[60].

For microscopy studies, Gervasio *et al.* (2007) selected a similar combination of time points from 0 to 10 days post injury (2-3 mm surgical excision of sciatic nerve) for confocal microscopy and confocal

Fluorescence Resonance Energy Transfer (FRET) visualisation of AChRs and rapsyn in female FVB mice[12].

Gigo-Benato *et al.* (2010) performed light microscopy analysis for neural cell adhesion molecule (NCAM) and neurofilament protein on samples from male Wistar rats subjected to a sciatic nerve crush injury with time points commencing 3-4 days later than those of Gervasio *et al.*, i.e. at 3, 5, 7, 9, 11 and 14 days post injury [64].

Pinter *et al.* (2003) selected days ranging from 1, 3, 5, 7, 10, 21, 28 and 35 days post injury for H&E as well as AChE analysis of samples from male Wistar rats subjected to an extreme surgical excision (length of 30 mm) from the sciatic nerve[67]. Magill *et al.* (2007) again followed a period of weeks post sciatic nerve crush injury (1, 2, 3, 4 and 6 weeks) and visualisation was done on whole mount samples of the *tibialis anterior* of homozygous thy1-YFP mice, using confocal microscopy to identify axons, AChRs and Schwann cells[27].

Studies by Ma and Shen *et al.* (2005, 2006, 2007) use time points that extend up to 1 year (3, 7, 14 or 15, 30, 90, 180 and 360 days) post injury, either by local BoTX injection (*gastrocnemius*)[30,31] or nerve transection (tibial nerve)[29]. Their analysis included qPCR of all AChR subunits[29,30] as well as MuSK, myogenin, MRF4, IGF-1 and P21[31]. Ma *et al.* (2005) performed additional confocal microscopy analysis of NMJ morphometry (assessed by AChR staining) on muscle segments taken from the *gastrocnemius* (taken adjacent to the motor end-plate area) at 2 weeks, 2 months, 6 months and 1 year after local BoTX injection[30].

Taken together the above studies have selected time points that included early response, early regenerative response and long-term recovery. In our laboratory, we have previously focussed on early time points: Macaluso (2009) made use of the following time points: 0 (control), 4 hours and 1, 2, 3, 5 and 10 days to assess the mouse specific contusion injury jig[77]. Rotter *et al.* (2008) used a muscle crush injury model and chose time points: 1, 7, 14 with an extra, far later point of 42 days[70].

Considering these time points, this study elected a combination of 1, 3, 5, 7, 10, 14, 21, and 28 days for post-injury analyses.

1.8 Linking Satellite cells to the Neuromuscular Junction

There are some studies have investigated the possible involvement of satellite cells in the regeneration of injured NMJ[14,43,71,80].

Vigue *et al.* (1997) counted of satellite cells in denervated rat muscle by means of electron microscopy and demonstrated a 2- to 3-fold increase in their number during the first few weeks

following denervation[80]. Later, Borisov *et al.* (2005) observed long term SC regeneration efforts in denervated muscle at 1, 2, 4 and 7 months post denervation by identifying and quantifying the presence and number of small myotubes (products of SC differentiation)[43]. They found a significant increase (12- to 14-fold that of the control muscle) by the end of the first month following denervation. By 2 months after denervation, an extraordinary 44-fold increase over the control was noted. The presence of these small myotubes decreased by 30% and 60% from the level observed in 2 month denervated muscle after 4 and 7 months of denervation, respectively[43].

Increased densities of satellite cells have been detected at the NMJ[3,5] with about 20-fold greater frequency than at non-junctional regions in adult rat and human muscles[5]. A review by Zammit *et al.* (2006) included a sterling image of an immunohistochemically stained isolated *soleus* myofibre, displaying Pax7 stained SCs distributed in the proximity of the NMJ[37] (see Figure 1.9). This accumulation of SCs can be explained by factors secreted by the nerve which attract the SCs[58]. In return, when the nerve suffers damage and disconnection from the NMJ, it is credible to hypothesise that the SCs are activated (through muscle signals and perhaps the sudden lack of neural signals) and accelerate the NMJ regeneration process especially of the endplate.

Hirata *et al.* (2005) presented one of the few studies to use immunohistochemical techniques to assess both the NMJ with α-btx and SCs with BrdU in regenerating muscle (*tibialis anterior*) after denervation. However, staining for these two role players was performed separately on consecutive sections and no $BrdU^+$ myonuclei were shown in the vicinity of the NMJs[14].

Court *et al.* (2008) conducted a different study that also used immunohistochemical staining with both α-btx for AChRs and BrdU for SCs. Again, they used separate, consecutive sections. Interestingly, they investigated a cell that covers, or 'caps', the NMJ by using novel cytoskeletal antibody 2166[57]. Failure of M-cadherin, N-CAM and desmin staining to label these cells ascertained that the NMJ capping cells were not in fact satellite cells.

Numerous studies exist that investigate the effects of denervation on gene expression of AChR sub-units of the AChR[12,27,29–31,56,60,62,64,67] (See Table 1.2 Nerve injuries and time points). However, there is a lack in literature reporting the effects of injuries of a different nature on the AChR subunit mRNA expression. Furthermore, while some studies have considered a role for SCs in NMJ regeneration[5], visual proof of this has yet to be presented. On the one hand, this allowed for a novel model to be used. On the other hand, this also posed methodological issues that needed to be resolved.

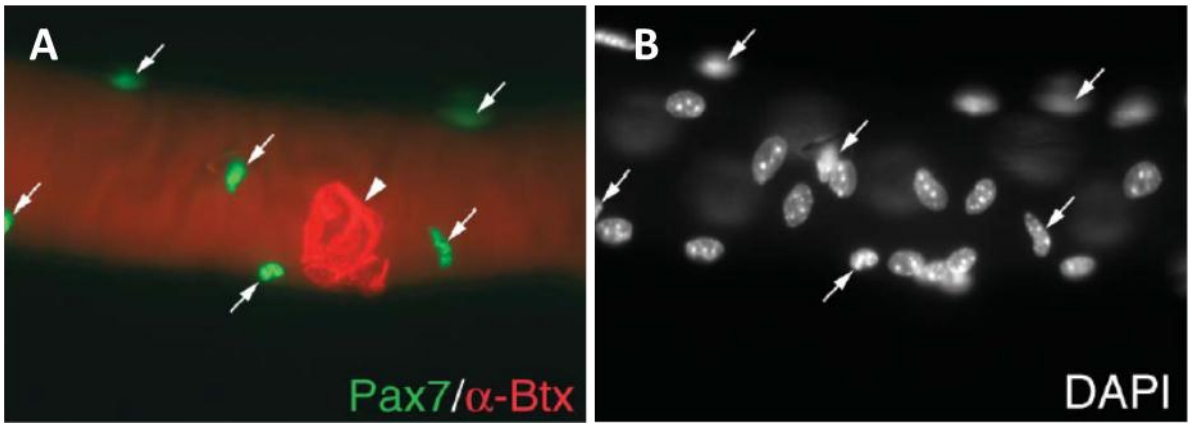

Figure 1.9 Satellite cells' distribution in proximity to NMJ in soleus muscle. A) Soleus myofibers usually have an accumulation of satellite cells (Pax7, green) around the motor end plate (α-btx, red) where the motoneuron contacts the myofibre (B) All nuclei present were identified using 4,6-diamidino-2-phenylindole (DAPI) counterstaining (blue). From Zammit *et al. (*2006).

1.9 Study Design Considerations

1.9.1 Introduction

This study required the selection and use of antibodies and techniques that were not familiar to our research group. These novel components warranted additional investigation and the factors to consider are discussed below.

1.9.2 Super-resolution imaging of NMJ structure

1.9.2.1 Previous super-resolution studies

NMJs are a popular structure for the community of neurophysiology researchers using immunofluorescent techniques; however most super resolution experiments are focused on the developing and diseased NMJ[26,34,69].

Shi *et al.* (2012) beautifully illustrated the development of the NMJ from 5 days postnatal to the matured adult NMJ[81] (see Figure 1.6).

Pratt *et al*. (2014) depicted the morphological changes in the NMJ in intact, dystrophic and muscle-lengthening injured WT mice[26] where NMJs of dystrophic mice lacked organization and were far more vulnerable to injury. Upon injury, these poorly organized NMJs were disrupted and dispersed into scattered islands of signaling proteins (see Figure 1.7).

Schmidt *et al*. 2011 observed a loss of synaptic branches in ErbB mutant mice with AChRs developing perforations – seen by presence of AChE activity in areas with no positively stained AChR[69]. This study created 3D images by means of combining confocal image stacks.

Although such advances are appearing in the literature, the study in this thesis was the first to focus in depth on the NMJ degeneration and regeneration using immunohistochemistry, as well as observing the effects of injury on the surrounding muscle tissue.

1.9.3.2 Selection of antibody for NMJ visualization

Nicotinic acetylcholine receptors are the best-studied of the ionotropic receptors[53,54]. Two discoveries have allowed for the extensive study of these receptors, namely:

A. The finding of the AChR-rich electric organ of the fish, *Torpedo californica*. This provided an abundance of AChRs for receptor purification[53,54].

B. The discovery of α-bungarotoxin (α-btx) - a neurotoxic component of krait snake (*Bungarus multicinctus*) venom. α-Btx binds to the α-subunit of the AChR and inhibits its function, resulting in debilitation of the NMJ and paralysis of the affected myofibres[53,82]. The advantage is that the binding is quite specific.

The efficacy of α-btx in labelling AChRs has made it the trade mark probe in immunohistochemical analyses[12,26,36,76,80,57,83–85]. The tetramethyl-rhodamine α-bungarotoxin probe (from Molecular Probes™) alone boasts over 100 publications in its product bibliography that have utilized this probe. The popularity of this probe may be a substantial reason for the synonymy of AChRs and the NMJ in immunofluorescent research.

Other antibodies used in NMJ research include various antibodies against presynaptic (e.g. neuregulin[78], syntaxin[12], synaptophysin[69] and neurofilament[69]) and postsynaptic (e.g. Lrp4[85]) components. Another popular method involves staining for AChE activity which involves a very simple, but effective staining protocol[56], although immunohistochemical staining for AChE is also used[69].

For this thesis, an AlexaFluor® 488 conjugate of α-btx (Life Technologies, B13422) was used due to the preferred fluorescent brightness; pH insensitivity and greater photo stability than other variants of α-btx[82].

1.9.3 Satellite Cell detection

1.9.3.1 Introduction

SCs were originally detected in frog skeletal muscle by means of electron microscopy in 1961[36,86]. Fortunately, scientists have described a number of molecular markers expressed by quiescent, activated and proliferating SCs, allowing researchers to illuminate the role of these dynamic cells under light microscopy. Below are some of the popular SC markers used in many laboratories:

- *CD56/NCAM* – a membrane marker that recognises the neural cell adhesion molecule (NCAM) and stains both quiescent and activated SCs. CD56 also stains lymphocytes (natural killer cells); nerves, neuromuscular junctions and the cytoplasm of the occasional myofibre[3,40,41]. This multi-staining does not allow for specificity unless co-stained.
- M-cadherin – a transmembrane protein that's expression is upregulated in activated SCs[41]
- *Pax7* – is a popular marker for SCs and specifically labels quiescent and activated SCs[37]
- *The myogenic regulatory factors (MRFs)* – staining with antibodies for these SC markers (Myf5, MyoD, Mrf4 and Myogenin) allows one to ascertain which phase the identified SC is presently undergoing.

Many immature cells, such as SCs, go through proliferation prior to differentiation. During DNA replication nucleotide insertion can be tracked, for example using administration *in vivo* of bromodeoxyuridine (BrdU) with subsequent analysis of samples using an anti-BrdU AlexaFluor® 555 conjugated antibody.

1.9.3.2 Definition of Bromodeoxyuridine

Bromodeoxyuridine (BrdU) is a synthetic thymidine analogue which incorporates itself into a cell's DNA when the cell is dividing (during the S-phase of the cell)[87–89]. BrdU is commonly used in the detection of proliferating cells in living tissues or as a cell cycle marker. It is administered to animals either shortly before euthanasia or as a chronic treatment[88–90]. A common reason for chronic administration is to monitor the proliferation of experimentally administered stem cells[90].

1.9.3.3 Selection of method of Bromodeoxyuridine dose administration

BrdU (molecular weight 307.1) has a half-life of roughly 5-6 hours, according to Harvard Department of Stem Cell and Regenerative Biology[88], although this will vary depending on the dose given. BrdU doses range mostly from 50 mg/kg up to 200 mg/kg for rodents (see BrdU *in vivo* dose table in Appendix I).

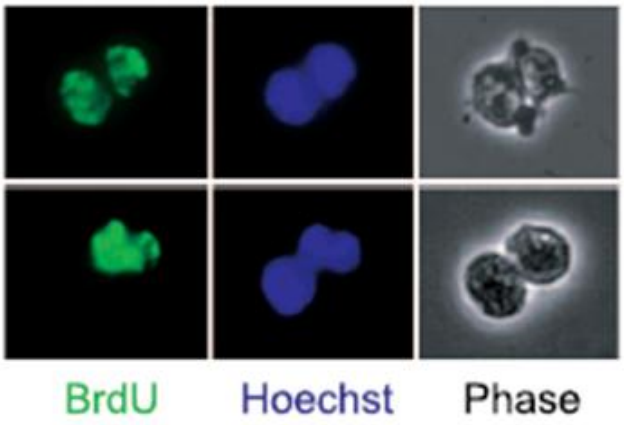

Figure 1.10 BrdU incorporation into dividing cells. From Conboy *et al* 2007

Methods of BrdU administration considered for this study included:

- ***Intra-peritoneal method*** – Animals receive a single or multiple BrdU injections over the course of the experiment. Boston Guidelines recommend daily IP injections (~ 2 mg in 100 µl of sterile saline) for mice[90]. This method is relatively simple and effective, although repeated injections can cause stress to the animals. (See Appendix I for a table of BrdU *in vivo* doses used in different studies.)

  Since satellite cells start proliferating a few hours after injury[37], an initial IP injection at the time of injury is a good start – especially considering that the animal is under anaesthetic at that time so discomfort is minimized.

  Drinking Water method - A daily dose of between 0.25-1mg/ml is recommended for up to 6 weeks before sacrifice/analysis[88], This method is preferred for longer term studies where BrdU incorporation can be detected in proliferated cells for up to 70 days (after a design of receiving 9 consecutive days of drinking water containing BrdU; followed by a no further administration)[87]. However, this mixture must be prepared daily, and discarded BrdU solution from the previous day renders this method both wasteful and expensive[87]. In addition, oral administration may lead to lower plasma levels than IP administration and thus eliminates the chance to precisely control the exact time and level of BrdU ingested – introducing variability into the experiment[88].

  Osmotic pumps - insertion of mini-osmotic pumps (either IP or subcutaneously) filled with a BrdU solution of desired concentration allows for consistent administration of BrdU (releasing a certain tiny dose every hour). This overcomes the 5 - 6 hour time limit of BrdU in the blood system and thus proves to be more consistent, effective and superior to both of

the above-mentioned methods. Although expensive, this method is far less invasive than daily IP injections.

BrdU incorporation is detected in areas such as the small intestine, thymus and bone marrow just 30 minutes post-injection, while in other tissues it can usually be detected within 24 hours[87]. It is important to determine the amount of time it takes for BrdU to incorporate into the tissue in question (in our case, skeletal muscle) as this, along with the short *in vivo* half-life of BrdU and the invasiveness of IP injections forces one to make critical decisions in order to settle for the best number and timing of injections delivered.

1.10 Aims and Hypothesis

Methodological Aims

The study in this thesis includes a number of methodological aims for the establishment of the desired animal model and sample analysis.

A. To induce a standardised skeletal muscle contusion injury in mice using a non-invasive technique
B. Depicting muscle fibres in longitudinal section in a) intact and b) injured skeletal muscle
C. Identifying the most effective method of BrdU administration for the tracking of proliferated satellite cells by quantifying number of $BrdU^+$ stained myonuclei per myofibre
D. Successfully imaging $BrdU^+$ cells and NMJs (represented by α-bungarotoxin stained AChRs) in the same myofibre with immunofluorescent microscopy and counting number of $BrdU^+$ cells residing beneath each NMJ as well as in the surrounding area

Thereafter the following hypotheses could be tested:

Injury to both muscle fibres and associated peripheral NMJs will result in:

A. Elevated mRNA levels of fetal (γ) but not adult (ε) AChRs, measured by qPCR, in injured but not in non-injured mouse *gastrocnemius* muscle in days following muscle contusion injury that will be similar to that found with other models of denervation.
B. Altered a) morphology and b) arrangement of the NMJ end-plate will be visible on relatively intact muscle in the border zone of the injury
C. Different morphologies for the intact, injured and regenerating NMJs in *gastrocnemius* muscle are visible under immunofluorescent microscopy
D. Decreases in surface area and volume of the NMJ with injury and, upon regeneration, increases towards normal levels as seen in the intact NMJ.
E. Proliferation of SCs (quantified by counting of $BrdU^+$ myonuclei) in *gastrocnemius* muscle in days following muscle contusion injury
F. $BrdU^+$, proliferated satellite cells located beneath the NMJ in *gastrocnemius* muscle in the later days following muscle contusion injury

Chapter 2 Materials and Methods

2.1 Study Design

2.1.1 Animals

Male BALB/C mice were bred at the University of Cape Town Research Animal Facility. Once weaned, animals were housed in the Small Animal Unit in the Department Physiological Sciences at Stellenbosch University. Animals were divided and housed in groups of six for the duration of the study, with the exception of the mice implanted with mini-osmotic pumps containing BrdU, for the labelling of satellite cells. These mice were housed individually after their pump implantation surgery. All animals had access to food and tap water *ad libitum* and were exposed to a 12 hr light/dark cycle (lights cycle starting at 6:30am). Ambient temperature was controlled at 21 - 24°C, and rooms ventilated at 10 changes/hour. Mice were handled regularly and cages were cleaned once a week (minimum). All experimental protocols were approved by the Animal Ethics Committee of Sub-Committee B of Stellenbosch University, (SU-ACUM12-00025).

All mice were allowed to reach maturity (>8 weeks; mean weight: 24.16 ± 2.66g) before subject to any intervention.

2.1.2 Experimental groups

Preceding the onset of the implantation surgery and contusion injury, experimental mice were randomly divided into the following groups:

A. Mice for PCR analysis (PCR; n = 48; 6 mice per time point) – subjected to injury only.

B. Mice for immunohistochemistry (IHC) analysis (BrdU; n = 42; 6 mice per time point) – subjected to pump implantation surgery and injury.

The mice in each group were further divided according to the specific time-points that they would be sacrificed after the contusion injury. These time points were set at 1, 3, 5, 7, 10, 14, 21 and 28 days post-injury. The 21 day time point was excluded from the BrdU group due to limited availability of mini-osmotic pumps.

The contralateral non-injured leg served as the control for all animals. As the insertion of mini-osmotic pumps is a standard BrdU administration technique (see Appendix I), no sham group was included.

2.1.3 Intervention protocols

The study included 2 intervention protocols:

A. Implantation surgery of mini-osmotic pumps for BrdU administration (BrdU group only)

B. Muscle contusion injury

Briefly, the pump implantation was followed immediately by the mass-drop contusion injury, after which the animals were allowed to recover and muscle samples were collected at the specified time points after injury for subsequent analysis.

In the BrdU groups, BrdU delivery via the pumps continued throughout, up to the point of sacrifice, with the exception of the 28 day group: these pumps were removed after 14 days to avoid complications of a depleted pump.

Mice were weighed before anaesthesia in both groups and were weighed again just before sacrifice.

The study design is outlined in Figure 2.1.

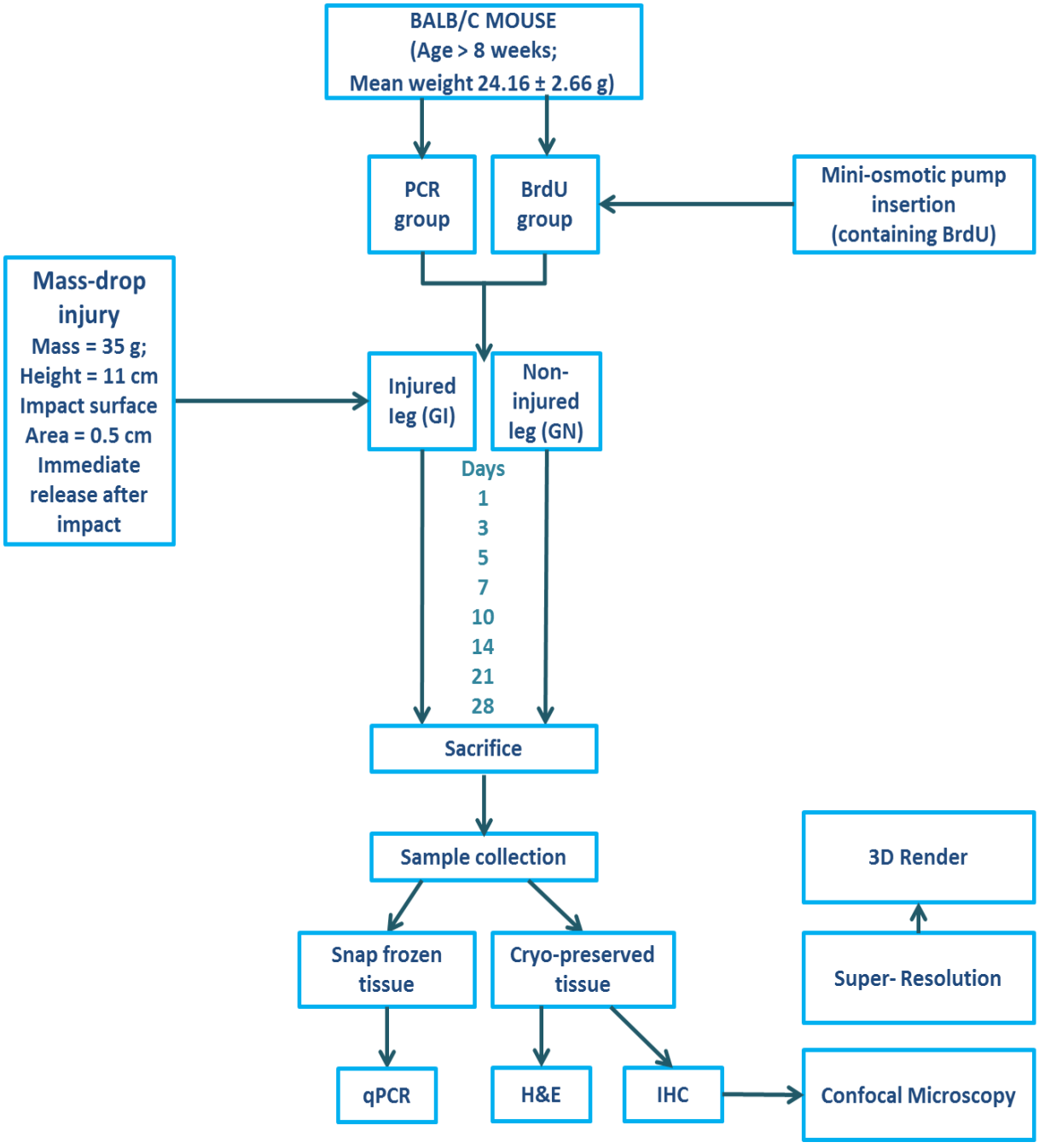

Figure 2.1 Study Design. Mice were divided into two groups –PCR and IHC (with BrdU). The BrdU group received pump implantation surgery and both groups were subjected to a contusion injury by a mass-drop technique in one leg only (injured leg).The contralateral leg served as control (non-injured leg). Animals were sacrificed on days 1, 3, 5, 7, 10, 14, 21 and 28 post injury. *Gastrocnemius* muscles from both legs were collected and either snap frozen (PCR group) or cryo-preserved (BrdU group). Histology for the BrdU group included H&E as well as IHC staining. IHC stained tissue was analysed by confocal microscopy, super resolution imaging and 3D renders of images.

2.1.3.1 Pump implantation

Pump Priming

Alzet® mini-osmotic pumps (model 2001, 1.0 µl.h^{-1} release rate and 200 µl volume) were prepared in a sterile environment the evening before implantation. Priming was performed according to instructions on www.alzet.com/. Pumps were filled with 50 mM BrdU (Sigma-Aldrich, Inc.; B5002, CAS 59-14-3, dissolved in 1x PBS) and left to prime overnight at 37°C (See Figure 2.2).

Anaesthesia

Mice were anaesthetised (Ohmeda Isotec 4) in a pyrex container, inhaling 3% Isoflurane (Isofor, Piramal Health Care; 28/2.1/0165) in 100 % oxygen for induction. Following onset of anaesthesia, the mouse was placed in prone position on the work board, with its head placed in a mobile tube connected to the Isofluorane supply. Flow rate was reduced to 2 % isoflurane for maintenance of anaesthesia.

Implantation surgery

Surgery instruments were sterilised with 70% alcohol commencing each surgery step and in between each surgery. Pump insertion was performed in groups of 6 mice each at 9am on the specified day assigned to each time group (7 groups in total) – spanning a period of two weeks. Pumps were implanted according to Reyskens (Ethics Application 11NF_REY01), under the guidance of animal technician, Mr Noel Markgraaff.

An area ± 2.0 cm long and 1.5 cm wide was shaved slightly posterior to the scapulae and sterilised with 10% iodine solution (Dismed Pharma; Q/13.1/65) followed by an alcohol swab.

Skin was lifted up with a pair of wide-tipped forceps and a section of ± 1.0 cm was cut horizontally above the pelvis. A haemostat was inserted under the incision to spread superior subcutaneous tissue and create a pocket 0.5 cm longer than the pump (each pump is 3 cm in length and 0.7 cm in diameter). The pump was inserted snugly with the open end of the pump furthest from the incision to prevent the escape of BrdU solution through the healing incision wound (See Figure 2.2).

It was ensured that the bottom end of the pump fits in at a lower level than the incision area. It was closed with two sutures in order to create an elevation of the stitched area. This was done to prevent the mouse from gnawing the stitches loose. Mice received a 1 ml injection of buprenorphine (Schering-Plough, Temgesic®, Nr. L/2.9/157.56) to relieve any pain resulting from surgery.

Additionally, mice were housed individually to prevent any potential violent behaviour or gnawing out of each other's stitches and were carefully monitored for post-operative complications.

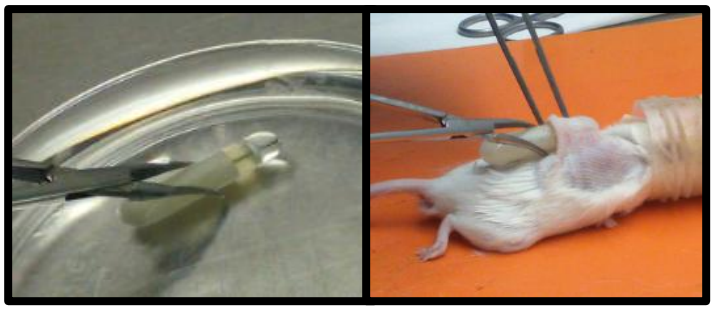

Figure 2.2 Alzet® mini osmotic pump priming (left) and insertion into mouse (right).

2.1.3.2. Injury

Apparatus

Contusion of the hind limb was created by a non-invasive apparatus (see Figure 1.7 and 2.3).

Briefly, the lower section of the apparatus comprised a large metal platform, with a small cylindrical platform in the centre, on which the hind limb of the animal rested just prior to and during injury. A plastic tube fastened perpendicularly to and directly above the smaller platform directed the passage of the flat, circular weight (mass = 35 g; impact surface area = 4.5 mm^2) from the desired height (11 cm) to the area of the muscle identified for injury. A steel peg placed in one of the holes in the plastic tube kept the mass in place at the desired height above the muscle, so that its removal resulted in a standardised mass dropping speed (see Figure 2.3).

A string is attached to the weight which is held loosely during injury and pulled tight immediately on impact to prevent a rebounding, second contusion injury.

Procedure

Mice were placed under anaesthesia as described in section 2.1.3.1. The left leg was shaved to prevent the weight from slipping off the sleek fur. This was done just before the injury was performed for PCR animal group, and prior to the pump insertion for the BrdU animal group. The injury immediately followed the pump implantation surgery for the BrdU animal group, while they were anaesthetised.

Mice were turned to supine position with left hind limb held at a right angle to create a bulge in the calf and expose the medial portion of the *gastrocnemius* muscle. The calf was positioned on the

platform, with the leg moderately extended away from the animal to prevent injuring the underlying bone. The positioning weight was placed slightly distal from the belly of the *gastrocnemius* muscle to target the maximum number of neuromuscular junctions, located in this central area of the muscle (see Figure 2.4).

*S*amples are referred to as GI (injured *gastrocnemius*) and GN (non-injured *gastrocnemius*).

Directly post-injury, mice were allowed to recover in their respective cages and monitored until regaining consciousness.

2.2 Sacrifice and sample collection

2.2.1 Sacrifice

Entry of mice into the intervention protocols was staggered so that no more than 2 groups were sacrificed on a single day. All sacrifice procedures took place between 09:00 and 11:00 in the morning to ensure accuracy of time point. All experimental animals were weighed prior to sacrifice and killed by cervical dislocation. The chest was observed to ascertain no signs of heart beat and toes were pinched to ensure no toe-spreading reflex occurred. After sacrifice, both left injured and right control gastrocnemius muscle were excised (see Section 2.2.2).

2.2.2 Muscle collection

Within 5 minutes of cervical dislocation, each mouse was laid in supine position. The gastrocnemius muscle of the each hind leg was exposed by an incision made across the shin and the skin and connective tissue surrounding the muscle was removed.

One arm of a fine tipped forceps was inserted at the attachment of the Achilles tendon and slid up to separate the calf muscle complex (*gastrocnemius, soleus* and *plantaris*). The connecting fascia (top) and Achilles tendon (bottom) were cut to free the calf complex from the leg. Remaining fascia was cut and soleus and plantaris muscles were pulled away from the gastrocnemius. The gastrocnemius was trimmed before cryostorage so only the injured central area and a sufficient amount of surrounding muscle tissue remained.

For preliminary histology and IHC work, the *gastrocnemius, soleus* and *plantaris* muscles were stored for analysis.

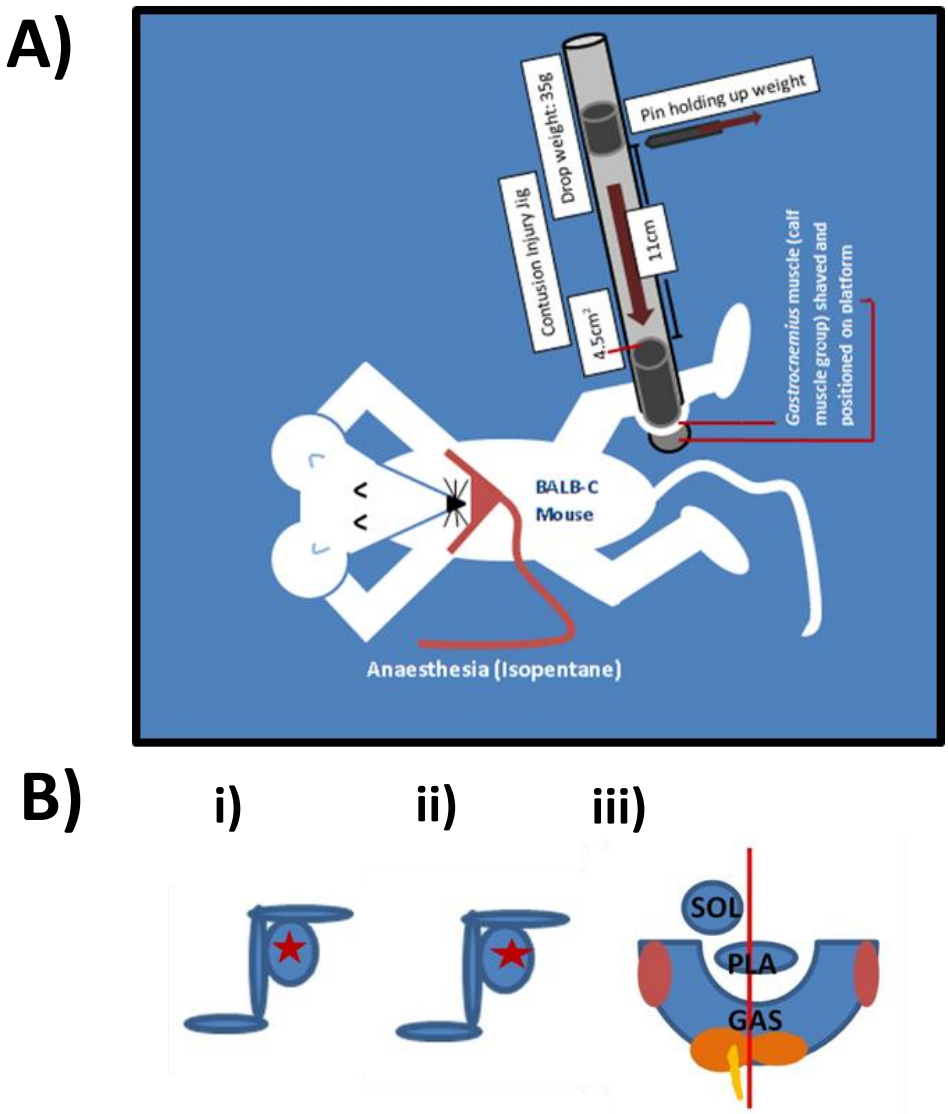

Figure 2.3 A) Position of mouse with contusion injury jig. B) Location of Contusion Effect of different impact areas on the Calf Muscle Complex. i) Standard belly of muscle impact (red star) affects the lateral and medial portion of the *gastrocnemius* (red areas in image iii) better for cross-sectional muscle injury studies. ii) Posterior positioning of impact area adapted to target the middle portion of the muscle (orange areas in image iii). This positioning was used for this longitudinal section study targeted at the neuromuscular junctions. (Positioning the weight too close to the bone results in the contusion impact affecting the *soleus* (SOL) and *plantaris* (PLA) muscles rather than the *gastrocnemius* (GAS). This also runs the risk of fracturing the bone. The red line indicates the midline of the calf complex with the medial head of the *gastrocnemius* on the left and the lateral head on the right. The yellow line indicates the impact point of the contusion injury weight. Visual interpretation from verbal descriptions by Dr Filippo Macaluso).

Muscles from the BrdU group were laid in longitudinal orientation on a square of cork, immediately coated in Tissue Freezing Medium® (Jung; 03702259) and immersed in pre-cooled isopentane (Merck KGaA, Darmstadt, Germany; 1.07177.1000). Muscles destined for PCR analysis were placed in 1.5ml eppendorf tubes and snap-frozen in liquid nitrogen. All samples were carried in a tank of liquid nitrogen and stored at – 80 °C.

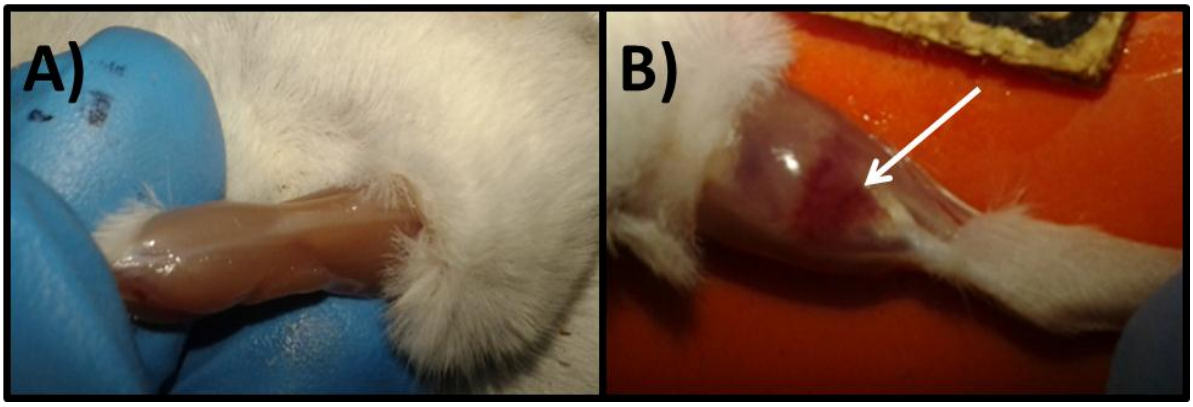

Figure 2.4 Exposed *gastrocnemius* muscle 5 days post-injury showing A) non-injured and B) injured leg (white arrow shows impact area).

2.3 Sample analysis

Three different analytical procedures were used:

A. mRNA isolation and RT-PCR analysis were performed on snap-frozen muscle tissue

B. Histological staining and visualization of muscle sections

C. Immunohistochemical analysis of muscle sections and individual neuromuscular junction (NMJ) complexes

2.3.1 Cryo-sectioning

Muscle samples were placed in the cryostat (Leica CM1860 UV Cryostat) at 25°C to adjust to the cryostat temperature for 1 hour. Each sample was fixed to a specimen platform with Tissue Freezing Medium® (Jung, 03702259) – applying either the cork square base of the BrdU samples or directly placing the muscle onto the specimen platform for snap frozen samples undergoing PCR analysis. Samples were securely frozen to the platform within a minute and were secured in the specimen cylinder for cryo-sectioning.

BrdU samples were sectioned longitudinally at a thickness of 10 µm. Sections were then pressed onto a slide coated with poly-L-lysine (Sigma Aldrich; P4707) and stored in a sealed container at -20 °C until staining.

PCR samples were sectioned longitudinally at a thickness of 20 µm, placed in a 1.5 ml eppendorf tube and weighed until 30 - 40 mg of tissue was obtained. Tissue was suspended in 750 ml of TriPure Isolation Reagent (Roche Diagnostics GmbH; 11667165001). Eppendorf tubes were placed on ice until stored at - 80°C for further use. The remainder of the tissue was placed back into its original eppendorf tube and kept at – 80 °C for possible further analysis.

2.3.2 PCR

2.3.2.1 RNA preparation

Cryosectioned muscle tissue was homogenised (Kinematica; Polytron PT2100). Chloroform (Sigma Aldrich, C2432) was added and the sample was left to stand for 10 minutes before being centrifuged at 12 000 g for 15 minutes to separate tissue mRNA from DNA and protein. mRNA was carefully removed and added to a new eppendorf tube containing 2-propanol (Sigma Aldrich, I9516). The mRNA sample was shaken, left to stand for 10 minutes at room temperature and then centrifuged at 12 000 g for 10 minutes to separate mRNA from the liquid. The supernatant was removed and the mRNA pellet was left to dry before being resuspended in 70% ethanol (Sigma Aldrich, E7023). It was then centrifuged at 8500 g for 6 minutes to remove any excess 2-propanol from the pellet. Ethanol was removed and pellet left to dry. Once dry, the pellet was resuspended in Tris/Borate/EDTA (TBE) buffer (Ambion®; AM9849) for subsequent mRNA quantification. See Appendix A for detailed protocols.

2.3.2.2 RNA quantification

1 µl mRNA was added to RNAse free water (Sigma® Life Sciences; W4502) at a concentration of 1:20 and was quantified using the Nanodrop Lite Spectrophotometer (Thermo Scientific), according to Appendix B.

2.3.2.3 Reverse transcription (RT)

Residual genomic DNA was eradicated by incubating samples at 30°C for 20 minutes with the use of the DNAse 1 enzyme from the DNAse 1 recombinant RNAse free treatment kit (Roche Diagnostics; 04716728001). 0.2M EDTA (Ambion®; AM9260G) was added and the sample was heated to 75°C for 10 minutes to inactivate the DNAse 1 recombinant. mRNA was reverse transcribed into cDNA using a Transcriptor first strand cDNA synthesis kit (Roche Diagnostics; 04896866001). Random Hexamer

primers were added and sample heated on a Thermal Cycler 2720 (Applied Biosystems) for 10 minutes at 60°C to denature any secondary structures present in the mRNA. Buffer (5x); Reverse Transcriptase Enzyme; protector RNAse and deoxynucleotide triphosphate (DNTP) were added and samples underwent the following heat treatments: 10 minutes at 25°C (for random hexamer binding to mRNA); 60 minutes at 50°C (for RT enzyme conversion of mRNA into cDNA) and 5 minutes at 85°C (for inactivation of the RT enzyme). See Appendix C for RT protocol.

2.3.2.4 Quantitative Real Time Polymerase Chain Reaction (qPCR)

Targeted genes were the adult and fetal AChR isoforms - AChR-ε and AChR-γ respectively - as well as glyceraldehyde-3-phosphate dehydrogenase (GAPDH) as a house-keeping gene. Samples were analysed in 96 well plates, running 2 plates per gene to accommodate the amount of samples (i.e. 6 plates in total). Each plate included 2 control samples (from non-injured leg of a mouse from the practise group) as reference samples for mRNA calculation (see Section 2.3.2.5).

Two-Step qPCR was performed on the StepOne Plus™ Real time PCR System (Applied Biosystems). Samples were run in duplicate at a concentration of 50 ng cDNA for GAPDH and 100 ng cDNA for AChR-ε and AChR-γ.

Genes were primed using TaqMan® Probes (Applied Biosystems; Mm00437411_m1 (for AChR-ε); Mm00437419_m1 (for AChR-γ); Mm03302249_g (for GAPDH)). Each PCR reaction contained cDNA of sample, primer, H_2O and TaqMan® Gene Expression Master Mix (Applied Biosystems; 4369016) according to Table 2.1.

Table 2.1 Reagents for PCR reaction for GAPDH, AChR-ε and AChR-γ genes and RT-PCR cycle conditions.

Gene	cDNA	Primer	H_20	Master Mix
GAPDH	1 µl	1 µl	8 µl	10 µl
AChR-ε	2 µl	1 µl	7 µl	10 µl
AChR-γ	2 µl	1 µl	7 µl	10µl

Cycle conditions for qPCR were:

A. 95°C for 5 min for DNA denaturation and synthesis of 1st cDNA strand

B. 40 cycles at 60°C (1min) (primer binding and reading) and 95°C for 15 seconds for completion of 2nd cDNA strand, PCR amplification of cDNA

In the reverse transcription (RT) step, cDNA is reverse transcribed from RNA. In the PCR step, PCR products are quantitatively synthesized from cDNA samples using the TaqMan Gene Expression Master Mix.

Fluorescence was measured after each cycle according to the equation:

$$\Delta R_n = R_n \text{ (post-PCR read)} - \text{Rn (pre-PCR read)}$$

where R_n refers to the normalized reporter dye. The ΔR_n is henceforth referred to as the cycle threshold (CT).

Days 21 and 28 were omitted from qPCR analysis due to financial constraints of running extra plates.

2.3.2.5 Calculation of 2ddct values

Quantification was plotted by the 2(-Delta Delta (CT)) calculation according to Livak & Schmittgen (2001)[91].

CT values were plotted on Microsoft Excel and 2ddtt values were determined by the following calculations:

$$dct = Mean\ AChRe(CT1, CT2) - Mean\ GAPDH(CT1, CT2)$$

$$ddct = dct(Sample) - dct(Reference\ Value)$$

2^{-ddct} = Final value

E.g. of calculation (Sample: Mouse 1, Day 1):

$$M1\ D1\ dct = Mean\ AChRe(32.39, 32.21) - Mean\ GAPDH(22.93, 23.09)$$

$$M1\ D1 dct = 32.3 - 23.01$$

$$dct = 9.29$$

$$ddct = dct(Sample) - dct(Reference\ Value)$$

$$ddct = 9.29 - 5.985$$

$$ddct = 3.395$$

2^{-ddct} = 0.095061

2.3.3 Histology

Longitudinal sections (L/S) (10 µm) were stained with haematoxylin and eosin (H&E) (see Appendix D) to subjectively visualise the injured area by observing the extent of immune cell infiltration, fibre oedema and damaged myofibres (see Figure 2.6).

2.3.3.1 H&E staining

Briefly, frozen sections were left in their respective coplin jars to thaw at room temperature (RT) for 3 minutes. Sections were then rinsed in distilled deionised water (ddH_2O) before being stained with Haematoxylin Solution (Merck Chemicals (Pty) Ltd; SAAR282200ILC) to stain the basophilic structures (i.e. structures containing nucleic acids such as cell nuclei). Differentiation from background staining was achieved by bleaching with acid alcohol (280ml 100% ethanol, 120ml ddH2O; 1,2ml HCl). Scott's Tap Water (2g $NaHCO_3$ + 20g $MgSO_4.7H_2O$ + 1l dH_2O) was used to give haematin structures a blue appearance[92]. Cells were stained with eosin (5 wt % solution in H2O) (Sigma Aldrich; 318905) to visualise intra- or extracellular proteins (mostly cytoplasm and red blood cells)[3].

2.3.3.2 Image analysis

Sections were imaged using a Nikon ECLIPSE E400 microscope. Images were captured using the 4x, 10x, 20x and 40x objectives to gain better overview and more detailed images on contusion injury in longitudinally sectioned muscle samples.

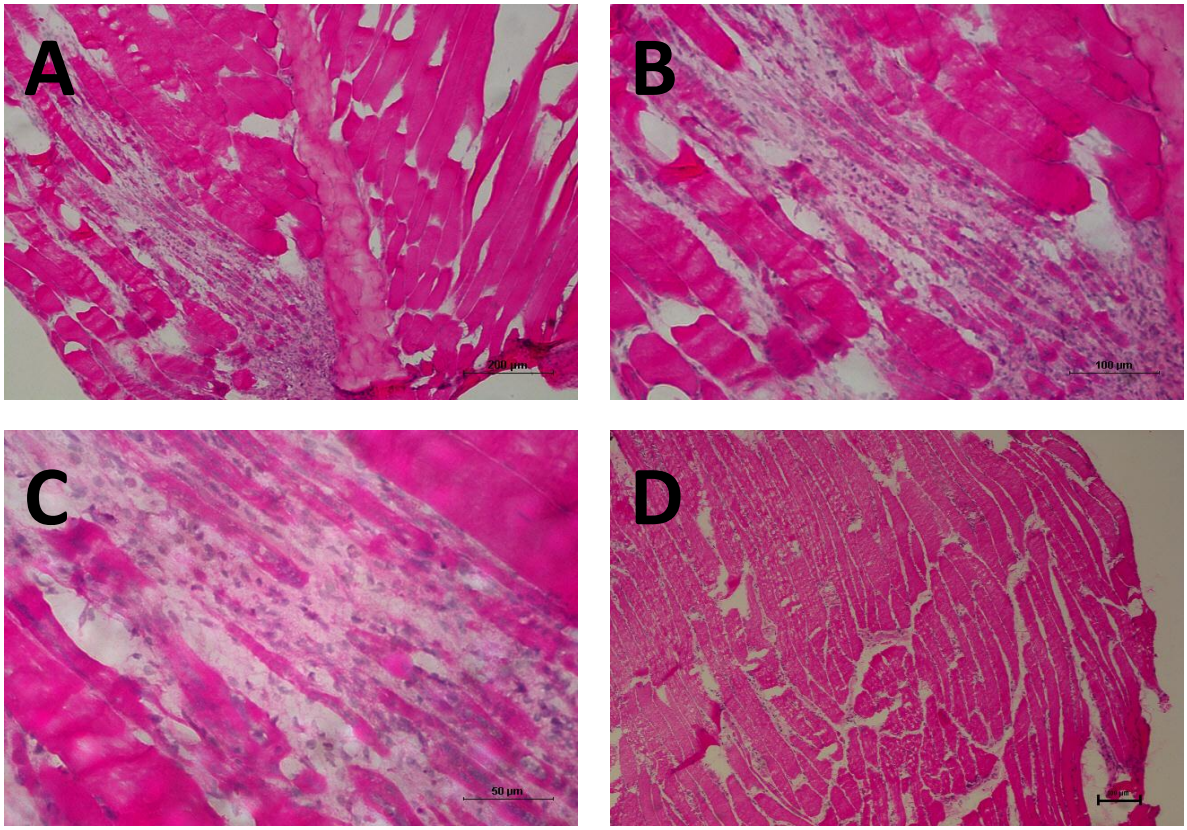

Figure 2.5 H&E staining trials to observe myofibres in longitudinal sections using *plantaris* muscle, 7 days post-contusion injury. A) 10x magnification depicting infiltrating immune cells on left hand side of connective tissue (scale bar: 200 µm) B) 20x magnification of new, thinner myofibres being regenerated (scale bar: 100 µm) C) 40x magnification of individual nuclei of cells involved in the regeneration processes (scale bar: 50 µm) D) Non-injured *plantaris* muscle (10x magnification) (scale bar: 100 µm). Imaged on Nikon Eclipse E400.

2.3.4 Immunohistochemistry (IHC)

2.3.4.1 Reagents

The following markers were used in IHC studies:

A. α-Bungarotoxin (α-btx) - stains the acetylcholine receptors of the neuromuscular junction

B. anti-Laminin – stains laminin, a structural protein of the sarcolemma, which delineates boundaries of nascent and mature myofibres

C. anti-BrdU – stains $BrdU^{+}$, proliferated nuclei , i.e. satellite cells and white blood cells

D. Hoechst – stains all nuclei (e.g. myonuclei, satellite cells, white blood cells)

All dilutions were made with 10x phosphate buffered saline (PBS).

Details of the primary and secondary antibodies used for immunohistochemistry are summarised in Table 2.2 below:

Table 2.2 Antibodies used to identify muscle membrane (laminin), acetylcholine receptors (α-btx), satellite cells (BrdU) and myonuclei (Hoechst).

Antibodies	Species	Dilution	Cat. Nr	Supplier
Primary antibodies				
Anti-BrdU Clone MoBU-1 AlexaFluor® 555 Conjugate	Mouse monoclonal	1:50	B35131	Invitrogen, Life Technologies, Molecular Probes
α-bungarotoxin AlexaFluor®488 Conjugate	*Bungarus multicinctus*	1:1000	B13422	Invitrogen, Life Technologies, Molecular Probes
Laminin	Rabbit polyclonal	1:250	Z0097	Dako
Secondary antibodies				
AlexaFluor® 594	Donkey anti-rabbit	1:250	A21207	Life Technologies
Nuclear stain				
Hoechst	/	1:500	14533	Sigma-Aldrich, Schnelldorf, Germany

2.3.4.2 Procedure

Detailed procedures for IHC staining are listed in Appendix E.

Briefly, slides were dried and sections were encircled with a wax pen to confine the reagents within the area of the section. Non-specific binding sites were blocked by incubating the sections with a combination of 5 % donkey serum (Jackson ImmunoResearch Laboratories, Inc.; 017-000-001) and 10% Bovine Serum Albumin (Roche Diagnostics, Mannheim, Germany; 10735086001) at room temperature for 60 minutes. The serum was then drained off and sections requiring DNA denaturation were treated with 4 M hydrochloric acid (HCl) (Merck (Pty) Ltd,; SAAR3063040LP) for 30 minutes. HCl was washed off and sections neutralised with PBS for 10 minutes. Primary antibody was added to the slides and left to incubate overnight at 4 °C in a humidified environment to prevent drying out. From here on slides were kept in the dark in a humidified environment. Slides were washed with 0.1 M PBS (1 ℓ of 1 M phosphate buffer, 90 g NaCl, 9 ℓ ddH_2O; pH 7.4) prior to addition of the secondary antibody (raised in donkey). After 60 minutes of incubation at RT, slides were

washed with PBS and a nuclear stain, Hoechst 33342 (Sigma-Aldrich, Schnelldorf, Germany; 14533), was added for 15 minutes. Sections were washed with PBS and coverslips were mounted on labelled slides with fluorescent mounting medium (Dako, North America, Inc.; 53023). Throughout the staining protocol, slides were kept in the dark in a humidified environment. PBS controls were used to test the specificity of the antibodies.

PBS controls were used to test the specificity of the antibodies.

Combinations with other antibodies can be seen in the 'trouble-shooting' section in Appendix H.

Earlier work was imaged using a wide field microscope (Olympus IX81 Wide field) at magnifications of 4x, 10x and 20x for L/S laminin trials and α-btx optimization. Sections stained with anti-BrdU AlexaFluor® 555 conjugate and confocal images for NMJ morphology were imaged on a confocal microscope (Carl Zeiss LSM 780 with Elyra S.1 super-resolution platform).

A diode laser was used to detect Hoechst-stained nuclei; an argon laser was used to detect AlexaFluor™488 and a helium-neon laser was used to detect AlexaFluor™555 and 594. Ranges for detection of the various wavelengths for confocal images of NMJs were 410-515 nm for Hoechst; 490-586 nm for AlexaFluor™488; and 623-753 nm for AlexaFluor™594. In BrdU images, the ranges for AlexaFluor™555 and AlexaFluor™594 were slightly different with (560 – 595 nm and 618-654 nm respectively) to avoid overlap between their closely associated fluorescent spectrums.

2.3.4.3 Tile scan analysis of NMJs arrangement on longitudinal muscle sections

Samples from the day 14 group for both GI and GN muscles (n = 6 per GI/GN group) were selected for NMJ analysis over the whole muscle. Samples were cryosectioned and sections were stained immunohistochemically in a two-step manner (see Pilot study 3). Firstly slides were stained with for α-btx, anti-laminin and Hoechst (see Appendix E with options 10.1 and 12.1). Coverslips were mounted temporarily using 1x PBS. Tile scans were taken at 10x magnification on a confocal microscope. Number of tiles ranged from 4 by 4 to 7 by 7, depending on the size of muscle sample.

Using the tile scan as a reference, separate images were taken of all the NMJs on each section at 40x magnification for better visualisation of NMJ shape and structure as well as number of subsynaptic nuclei. Coverslips were then removed and sections underwent the second staining step with anti-BrdU and Hoechst (step 6.3 of Appendix E, option 10.2 and 12.2).

Slides were re-mounted with fluorescent mounting media and images were taken in the same view as individual NMJ, located by use of the initial tile scan as well as laminin and light transmission for topographical similarities. Single colour stained controls were used to optimise detection settings, in

order to eliminate spill over between the dyes, especially AlexaFluor™555 and AlexaFluor™594 fluorescence separately.

2.3.4.4 Analytical method for NMJ classification and presence of subsynaptic nuclei

NMJs in each section were counted and categorised according to appearance as Over (O), Around (A), Side (S) or Tip (T).

For each NMJ the following was counted:

- Subsynaptic nuclei
- Subsynaptic nuclei enclosed by laminin
- Number of NMJs per number of fibres in view

Once re-stained with BrdU, number of $BrdU^+$ subsynaptic nuclei was also investigated.

2.3.4.5 3D analysis of NMJ morphology

NMJ selection

Separate longitudinal sections from mice at day 5, 7 and 14 post-injury were stained immunohistochemically with α-btx for NMJ visualisation; anti-laminin for myofibre membrane visualisation and Hoechst for nuclei (according to Section 2.3.4.2). NMJs representing the various regenerating states and orientations on the sectioned myofibre were selected from the different samples. Confocal images (40x magnification) of the area containing the selected NMJs for each chosen position on each section were taken in order to select NMJs with various characteristics (e.g. *en face*, side view, injured). After confocal imaging, these NMJs were located and imaged with Super Resolution Microscopy.

Super Resolution Imaging

Selected NMJs were imaged using the super-resolution platform of the microscope. Z-stacks were acquired to include the whole neuromuscular junction in the section. Super-resoluiton images were processed using Carl Zeiss ZEN2011 software and visualised as 3D constructs. 3D images of each NMJ were produced through Structured Illumination using Zen Black 2011 software.

Surface Area Measurement

Surface area of each NMJ was measured using Image J version 1.47. Positive threshold was determined and surface area measurement was provided in μm^2

3D Rendering and Volume Measurement

3D Rendering and volume measurements were performed using VGStudioMax 2.2 software.

TIFF files of each Z stack image were analysed as 16-bit images to create a 3D model of each super resolution image. A region of interest (ROI) was selected per NMJ for images containing more than one NMJ and surface area was determined by measuring all positive signal within each image (images with only 1 NMJ) or ROI (images containing more than one NMJ). Edge threshold was determined to exclude any autofluorescence surrounding the NMJ structures. Background was extracted and volume was analysed by surface determination across the three planes. The angle of the image was then rotated to produce an image that showed the most informative view of the NMJ.

Analysis

NMJs were categorised according to 1) their appearance on the sectioned myofibre; 2) their integrity and 3) organisation of surrounding laminin and nuclei. Surface area and volume were compared across the time points post injury as well as in intact samples and between categories of NMJ orientation (e.g. side view; *en face*; diagonal section).

2.4. Statistical analysis

Statistical analysis was done using GraphPad Prism 5 software. Column analyses were performed for PCR data using one way analysis of variance (ANOVA) with Bonferroni post hoc tests, comparing all columns. $p<0.05$ was accepted as significant. Outliers of more than 2.5 times the standard deviation were omitted from analyses. The Means of each time point were calculated in Prism. Weights at time of Injury (WtI*) and at Sacrifice (WtS*) were compared separately for each time point and two tailed T-tests were done between each pair of weights.

2.5 Pilot studies

Due to the variability in methods reported in the literature to administer 5-Bromo-2'-deoxyuridine (BrdU), it was necessary to optimise the experimental procedure. In order to achieve this, two pilot studies were carried out. These are discussed below.

2.5.1 Pilot study 1: Comparison between two different BrdU brands (Sigma and Life Technologies) in C2C12 cells and BALB/C mice

2.5.1.1 Introduction

The use of BrdU incorporation into the satellite cells is a new method for our research group and two popular brands of BrdU were chosen to compare in order to obtain the best BrdU results possible. These products were:

A. Sigma - 5-Bromo-2'-deoxyuridine (B5002)

B. Life Technologies - 5-Bromo-2'-deoxyuridine (B23151)

We tested the efficacy of these two brands in both *in vitro* (C2C12 cells) and *in vivo* (BALB/C mice) models (see Appendix I for a summary of BrdU doses from the literature).

2.5.1.2 Materials and Methods

Immunocytochemistry (ICC)

First, the BrdU was tested in cell culture on C2C12 (ATCC CRL-177 D57962; Yaffe and Saxel, 1977) muscle cells. Cells were routinely cultured in Dulbecco's modified Eagle's medium (DMEM) (Sigma Aldrich, Schnelldorf, Germany; D5796) supplemented with 10% Fetal Bovine Serum (FBS), 1% Penicillin Streptomycin (Gibco® from Life Technologies; 15410-122) and 1% L-glutamine (Sigma® Germany; G7513) in a 37°C humidified incubator (Shell Lab) with a 5% CO_2 (see Appendix F). Two T75 flasks of cells were cultured for 2 days, allowing them to reach 60% confluency. Sigma BrdU was added to one flask and Life Technologies BrdU to the other, at a concentration of 10µM for both brands (see Appendix J). Cells were left to proliferate for 12 hours. Cells were stained according to Appendix G with various concentrations of anti-BrdU antibody (1:50; 1:100; 1:200; 1:500 and 1:1000).

Immunohistochemistry (IHC)

Mice were given intraperitoneal (i.p.) injections of both brands of BrdU on days 0 and 1 post-injury (injury as in section 2.1.3.2.3 and muscle harvesting as in section 2.2). Cryo-sectioned muscle was stained according to section 2.3.4.2 with anti-BrdU 555 conjugate and Hoechst to view $BrdU^+$ cells co-localised with Hoechst-stained nuclei to confirm positive staining.

Imaging for both cells and mouse muscle was performed on a Confocal Microscope. Nuclei stained by both Hoechst and anti-BrdU were accepted as cells that had already proliferated or were in the process of proliferating.

2.5.1.3 Results

No quantitative data was obtained for images captured.

In the *in vitro* studies, only the Sigma brand at a 1:50 concentration showed successful BrdU incorporation (see Figure 2.6).

In the *in vivo* studies, both brands showed BrdU positivity, but the Sigma BrdU displayed brighter fluorescence than Life Technologies (see Figure 2.7), in agreement with the ICC trial.

2.5.1.4 Conclusion

We found the Sigma brand superior as a high concentration (1:50) of the Sigma anti-BrdU antibody achieved positive BrdU staining in proliferating C2C12 myonuclei *in vitro,* while the Life Technologies brand showed no BrdU positive stained myonuclei. Although the most potent brand and concentration were clear, this study was performed before adding a step of incubation in HCl (see Appendix I). The importance of the HCl step is to depermeabilize the nuclear membrane in order for the anti-BrdU antibody to penetrate the nucleus and bind to the BrdU incorporated in the DNA. The HCl step is discussed further in Pilot Study 3 in Section 2.5.3.

However, the sections obtained in the *in vivo* study were stained with the improved immuno-staining protocol, which included the HCl step (see Appendix E). Here the superiority of the Sigma brand is observed and henceforth decided to proceed with the Sigma BrdU for the upcoming experiments.

2.5.2 Pilot study 2: Viability of intraperitoneal (i.p.) injection method for delivery of BrdU

2.5.2.1 Introduction

The injection time points for BrdU needed to be optimised in order to determine which combination of days before and after contusion injury would label the greatest number of proliferating cells. The literature concerning injection time points for satellite cell studies varies greatly as seen in Appendix I. Frequency of i.p. injections range from once before injury[93], on combinations of days post injury[7], daily[75] and even twice per day[9] following injury (see Appendix I for BrdU Dose Tables).

As BrdU remains in the body for 5-6 hours, and our facilities do not have suitable restraining facilities for the rather invasive daily i.p. injections, it was important to determine which combination of days would yield the most BrdU incorporation into the greatest number of dividing satellite cells.

2.5.2.2 Materials and Methods

Mice (n = 6) were administered i.p. injections of 0.3256M BrdU on different combinations of days before and after contusion injury (see Section 2.1.3.2.) as seen in Figure 2.9. The mice were restrained manually and received their injections without anaesthesia. A single mouse per time point combination was used due to the large number of combinations and the limited amount of BrdU available for time point determination.

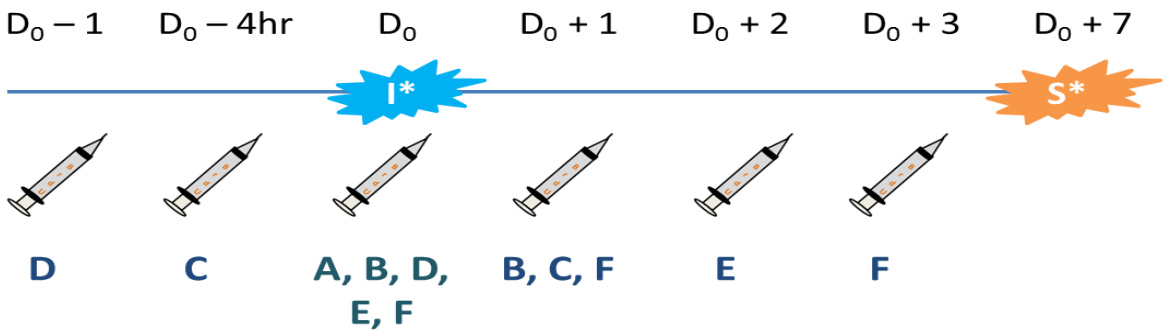

Figure 2.8 Study Design with combinations of BrdU injection treatments for mice A – F. D_0 denoted the day of contusion injury (I*), negative values represent days before contusion injury and positive values represent the number of days after contusion. Animals were sacrificed (S*) 7 days post injury ($D_0 + 7$).

Mice were sacrificed at 7 days post injury and muscle was excised and preserved as per Section 2.2.1 and 2.2.2. Sections were stained according to the BrdU steps in the IHC protocol (see Appendix E) and analysed on the confocal microscope.

2.5.2.3 Results

No quantitative data were obtained for the images captured.

'Mouse F' - which received intraperitoneal (i.p.) BrdU injections on days 0, 1 and 3 post-injury - showed the greatest occurrence of $BrdU^+$ cells(see Pilot 3 for images of BrdU in tissue from Mouse F).

2.5.2.4 Conclusion

Treatment combination for Mouse F was considered the best combination for i.p. administration of BrdU. However, through observations on Mouse F during its treatment, it was decided that the regular i.p. injections were too stressful for the animal and we investigated the option of inserting mini-osmotic pumps, an invasive, but once-off procedure. This would ascertain a constant delivery of BrdU to the muscles and overcome the obstacle of the limited time BrdU is available in the body.

A trial of the mini-osmotic pumps was run in BALB/C mice (n = 2) to learn pump insertion surgery as well as to determine the efficiency of BrdU delivery via the pumps. Pump implantation was as per Section 2.1.3.1 and mice were sacrificed at 14 days post injury. Immunohistochemically stained *gastrocnemius* muscles from the injured and non-injured leg showed satisfactory $BrdU^{=}$ results (See Figure 2.10 and 2.11).

2.5.3 Pilot study 3: HCl trials to permeabilize nucleus for BrdU visualisation

2.5.3.1 Introduction

In order to visualise BrdU in the nucleus, nuclear DNA must be denatured into single-strands. This allows the antibody to bind to the BrdU, incorporated into the nucleotide sequence. Failure to reach the BrdU results in no specific binding and fluorescence, as seen in Figure 2.12. Various methods to denature DNA exist, including subjection to acid, microwave treatment, rapid heating, or DNase treatment (Magavi *et al.* 2008). Hydrochloric acid is a popular, simple and readily available agent for nuclear depermeabilization (see Appendix I). We opted for treatment with hydrochloric acid (HCl) for this study.

While most literature suggests treatment in 2M HCl for 30 minutes (see Appendix J), little success was seen with this method and it was decided to investigate various combinations to ascertain the best method for this study.

2.5.3.2 Materials and Methods

Sections from Mouse F (Pilot Study 2) were analysed and stained according to the IHC protocol in Appendix E, using HCl (Merck (Pty) Ltd; SAAR3063040LP) in Step 6 in the following dose/time combinations:

A. 2M HCl for 30 min

B. 2M HCl for 60 min

C. 2M HCl for 90 min

D. 3M HCl for 60 min

E. 4M HCl for 30 min

Samples were tested in duplicate with one section receiving treatment with Sudan Black instead of 1x PBS for the acid neutralising Step 7 in Appendix E.

2.5.3.3 Results

The most successful DNA denaturation was observed with 2M HCl for 90 minutes. Treatment with 4M HCl for 30 minutes resulted in the brightest $BrdU^+$ fluorescence, but the Hoechst stain was compromised (see Figure 2.12 E,F).

2.5.3.4 Conclusion

Treatment with 4M HCl exhibited brighter fluorescence, but the intense acidity compromised the Hoechst stain, which was necessary to ascertain specificity of BrdU staining. Therefore, treatment with 2M HCl for 90 minutes was chosen as the best method for DNA denaturation.

However, in IHC work the following year on mice used for this study, the chosen treatment was not effective and 4M HCl for 30 minutes option was revisited. This treatment proved effective, without compromising the Hoechst stain and was continued henceforth.

An important discovery was made in further trials to image $BrdU^+$ satellite cells and NMJs together, when it was realised that treatment with HCl destroyed the α-bungarotoxin stained AChRs (see Figure 2.13).

HCl trials using concentrations as low as 0.5M and 1M for 30 minutes resulted in complete lack of AChR staining. Alternative DNA denaturing was attempted with 1:1 methanol/acetone. But this proved ineffective for BrdU staining.

A two-step staining protocol was created to overcome this problem (see Section 2.3.4.3). Briefly, cryosectioned muscle was initially stained with α-btx, anti-laminin and Hoechst; imaged to locate the NMJs; incubated with HCl (which destroyed the NMJ fluorescence) and stained with anti-BrdU and, once again, Hoechst to ensure brightness of myonuclei to determine colocalization of BrdU within the myonucleus.

Other options like using DNAse as a nuclear permeabilizing agent offer an attractive solution for imaging BrdU and the NMJ together as opposed to the two step method mentioned above. However, time constraints prevented the exploration of these options.

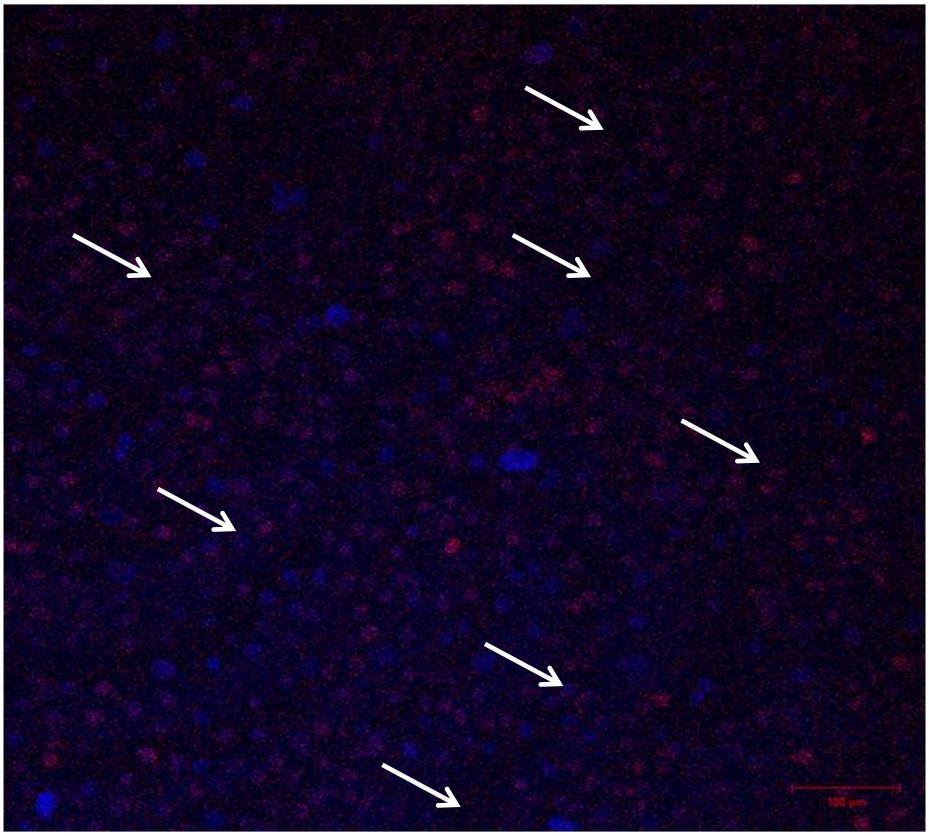

Figure 2.6 **Sigma BrdU fluorescence in C2C12 cells.** Myoblasts 12 hours after of proliferation in BrdU supplemented growth media. Hoechst (blue) stains every nucleus while BrdU+ nuclei (red) represent nuclei of daughter cells from a divided myoblast.

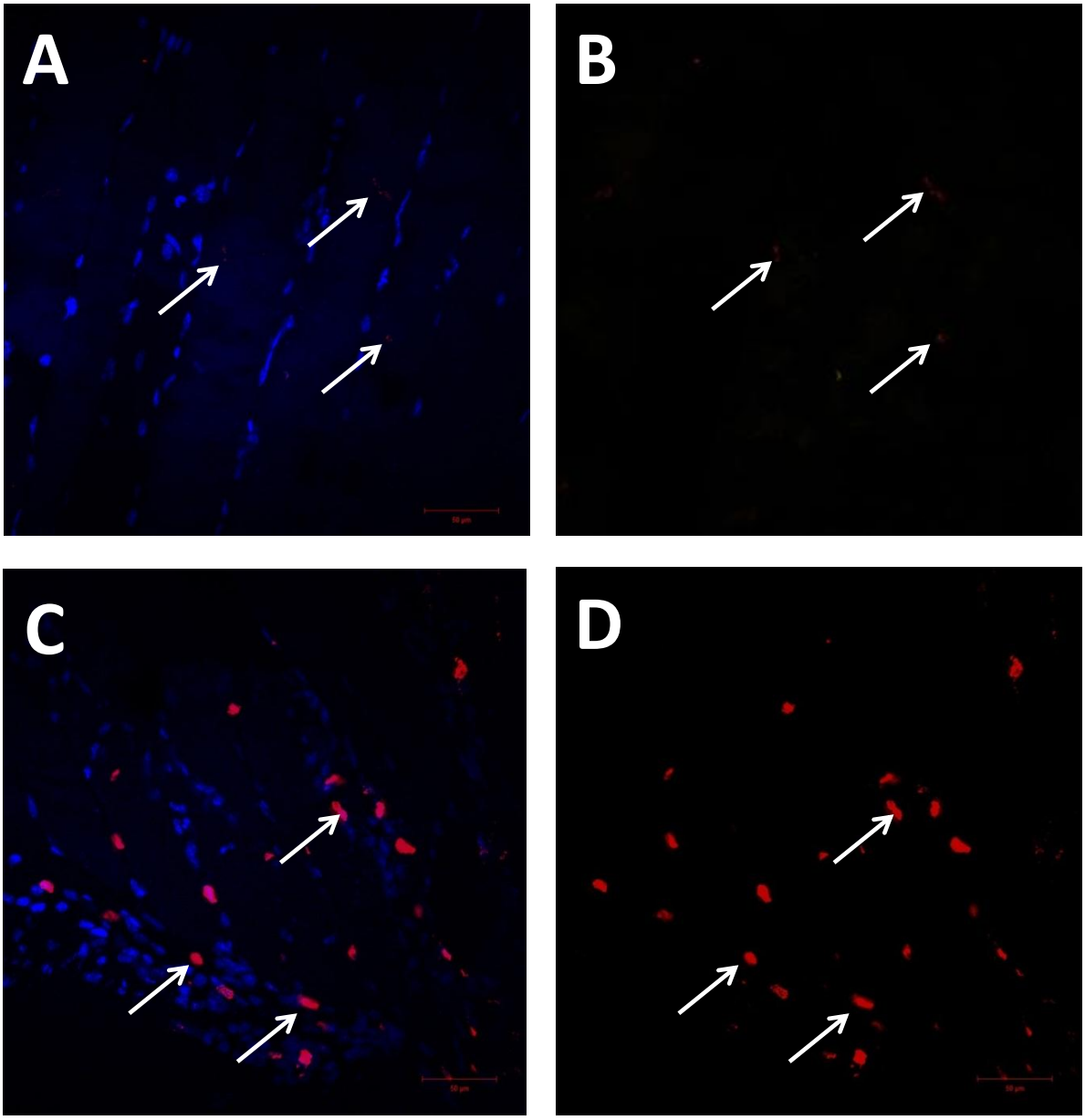

Figure 2.7 **IHC staining of BrdU from Life Technologies (A, B) and Sigma Aldrich (C, D).** Two mice received equal concentrations of the respective brands' BrdU in equal doses and were stained with the same IHC protocol. Sigma Aldrich's product displayed brighter fluorescence and specificity in BrdU+ cells than Life Technologies' product, in agreement with the ICC trial.

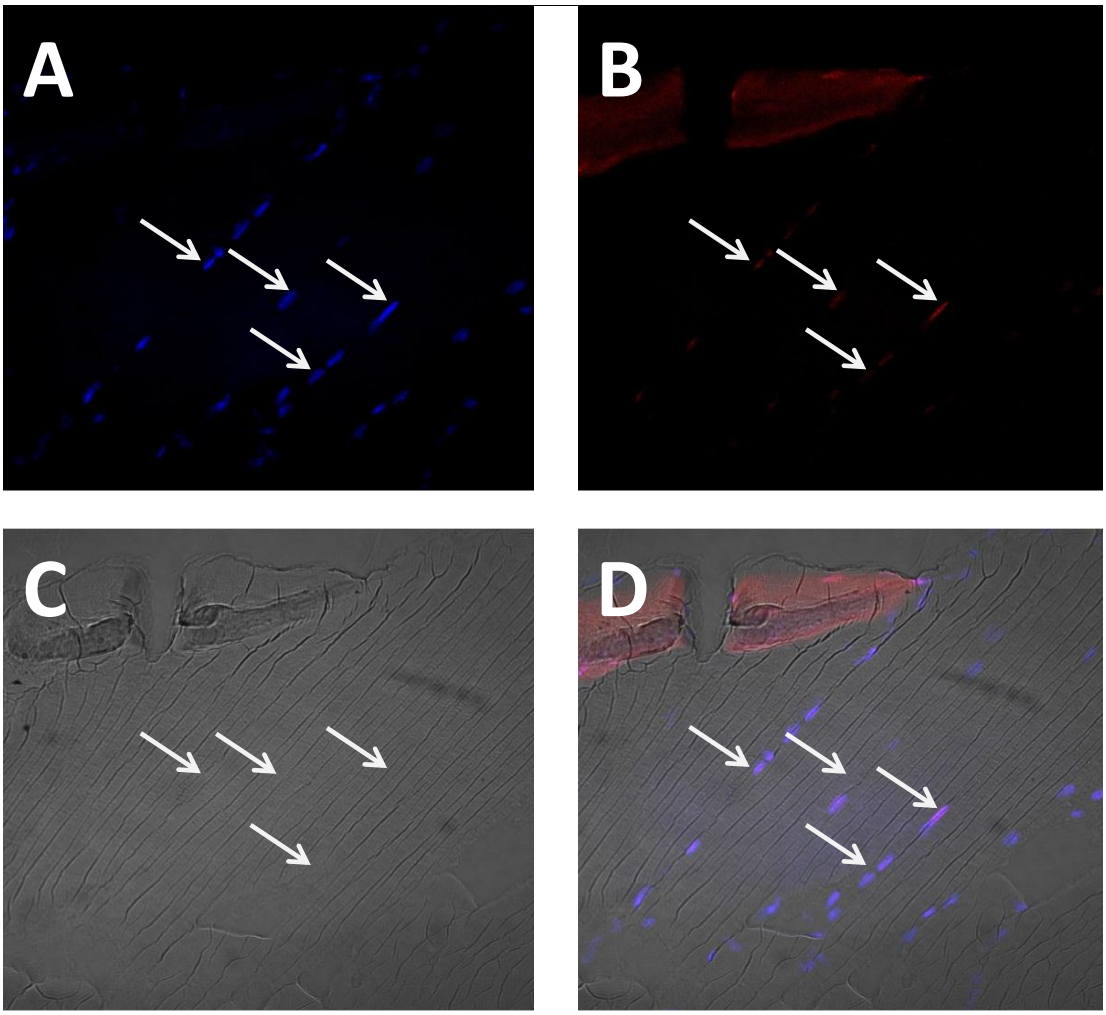

Figure 2.9 BrdU administration via mini-osmotic pump delivery showing presence of proliferated myonuclei in non-injured *gastrocnemius* muscle.

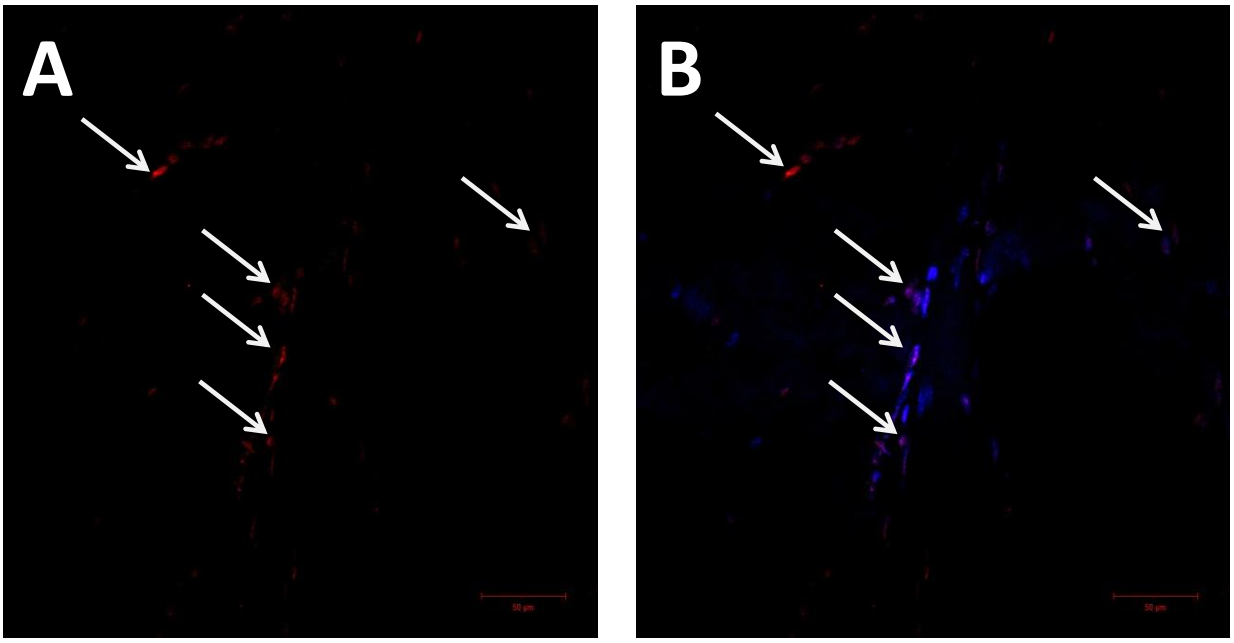

Figure 2.10 **BrdU administration via mini-osmotic pump delivery in injured *gastrocnemius* muscle**, 14 days post injury. Hoechst stained nuclei (blue) co-stained with BrdU (red).

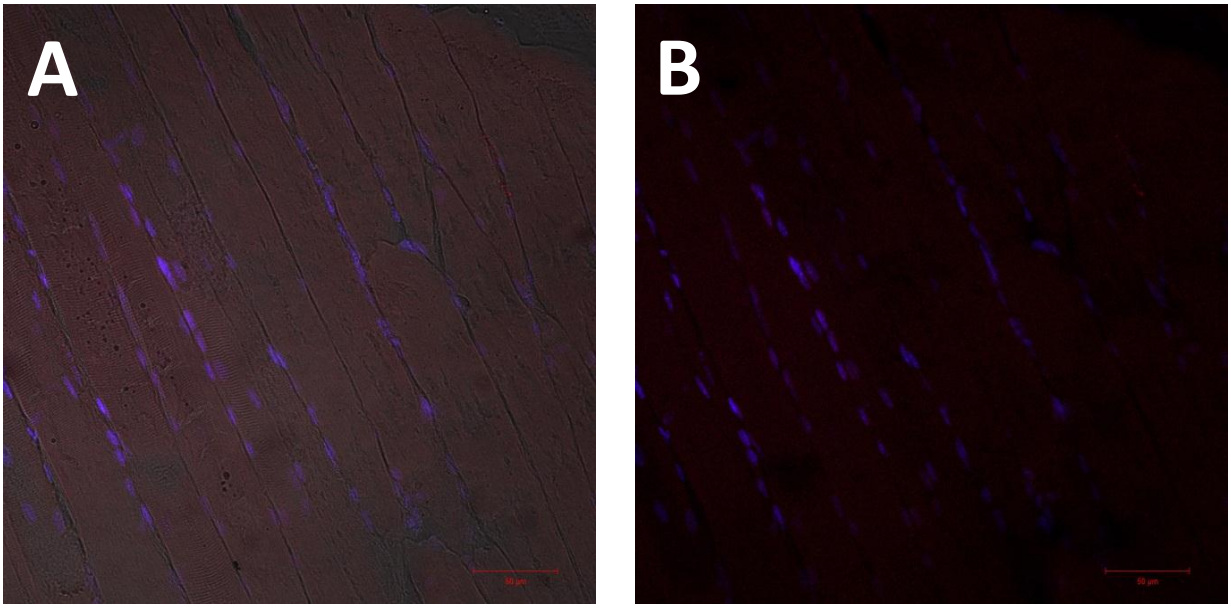

Figure 2.11 **No presence of BrdU^{+} cells in tissue not subjected to DNA denaturing step.** Injured *gastrocnemius* stained for BrdU, without the HCl step showing A) light transmission, Hoechst (blue) and BrdU (red) and B) Hoechst and BrdU. No positively stained BrdU cells are observed.

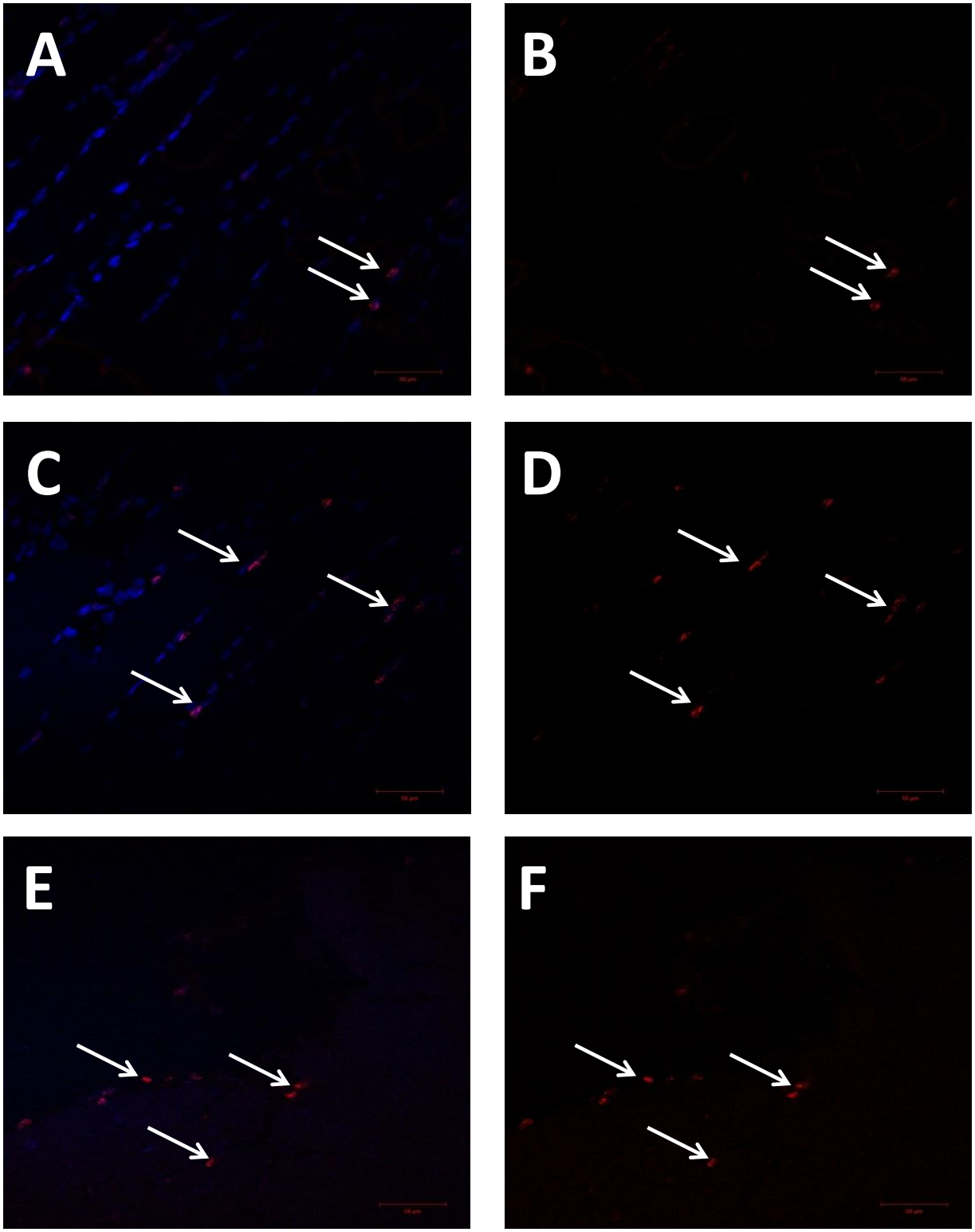

Figure 2.12 **BrdU^{+} presence after different concentrations of HCl and incubation periods in *gastrocnemius* muscle, 7 days post injury. A,B)** 2M HCl for 30 minutes; **C,D)** 2M HCl for 90 minutes and **E,F)** 4M HCl for 30 minutes. A, C and E) BrdU^{+} cells (red) co-localised with Hoechst stained nuclei (blue) and B, D, F) BrdU^{+} cells only.

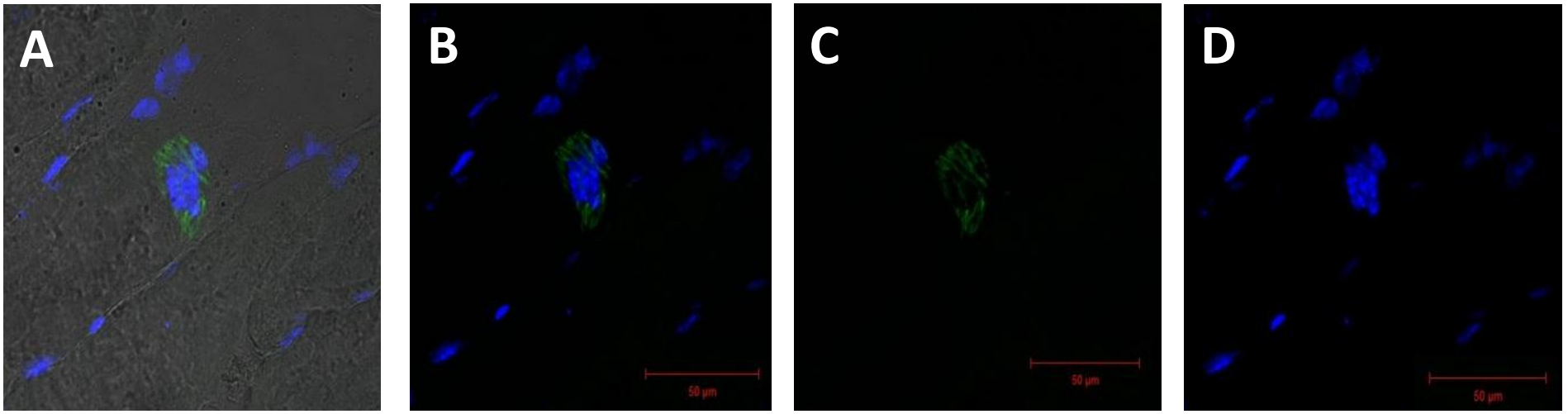

Figure 2.13 **Presence of NMJ without HCl.** A section that did not receive HCl treatment showed NMJs that were not visible on consecutive sections treated with HCl. NMJ visible **with A)** light transmission, α-btx (green) and Hoechst (blue) and **B)** α-btx and Hoechst at 40x magnification. Note: **C)** the immaculate network structure of this NMJ and D) the particularly dense cluster of subsynaptic nuclei (blue). Scale bar = 50 µm.

Chapter 3 Results

Mice used to investigate mRNA expression of AChR subunits did not receive BrdU administration or have osmotic pumps surgically inserted. These mice are discussed in Section 3.1.1. Mice used in histological experiments (with the exception of the *plantaris* muscle used for initial intact NMJ studies seen in Section 3.6.2, 3.6.3 and 3.6.4) did receive osmotic pump insertion surgery and subsequent BrdU administration. These mice are discussed in Section 3.1.2.

(**Please Note:** All Results microscopy figures can be found at the end of the Results chapter.)

3.1 Body mass of mice

3.1.1 Without osmotic pump insertion

The mean weight of mice at the time of injury was 24.1 g**.** There were no significant differences in mean body mass between mice from different groups. For most of the groups, there were also no significant increase in body mass between the day of injury and the day of sacrifice. However, there was a significant increase in body mass between injury and sacrifice in the 28 day group (+ 3.7 g; $p < 0.0001$), which could be expected.

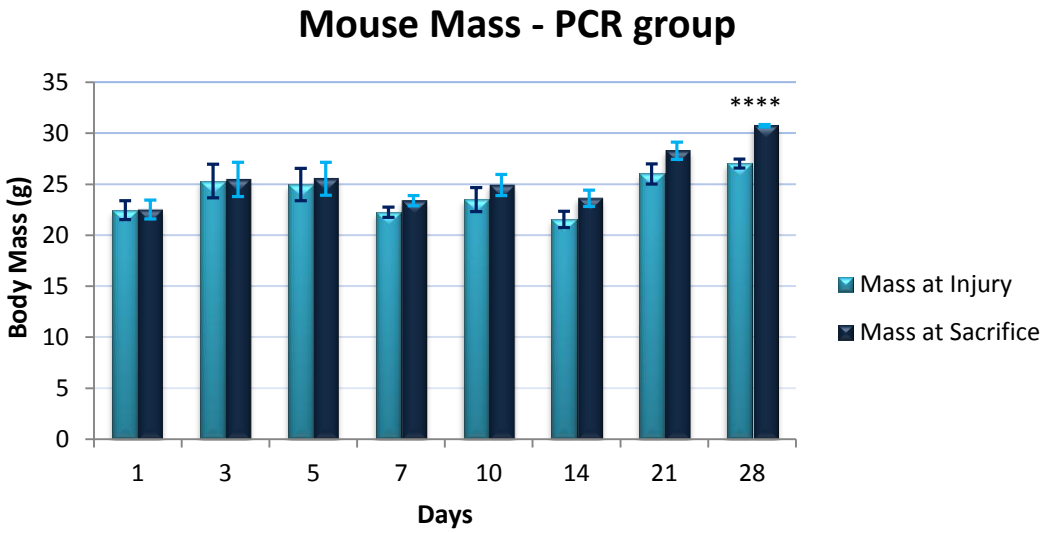

Figure 3.1.1 **Changes in mouse body mass over time, for mice sacrificed between 1 and 28 days post-injury.** Data are presented as means of body mass (n = 6 mice per time point), with Standard error. Each group was weighed on the day of injury (pale blue) and the day of sacrifice (dark blue). Stars indicate degree of significance: **** (p<0.0001) within group from pre-injury to sacrifice.

3.1.2 Before osmotic pump insertion and at sacrifice

Mean weight of mice at the time of injury was 24.3 g. There were no significant differences between groups at this point in time.

Mean weights in most groups of mice increased in proportion with the number of days post-injury, with an additional increase of ± 1.1 g - contributed by the weight of the mini-osmotic pump inserted at the time of injury (see Figure 3.1.2).

Changes in differences between means in time points that were less than 1 week between day of injury and day of sacrifice (days 1, 3 and 5) were smaller (< 2.0 g). Of these, only the day 3 group showed a significant increase (1.21 g; $p < 0.05$). Larger increases (>2.0 g) were seen in time points that extended for 1 week or longer (days 7, 10, 14 and 28). These increases in body mass (2.28 g; 2.74 g; 3.27 g and 4.88 g respectively) were all significant ($p < 0.01$).

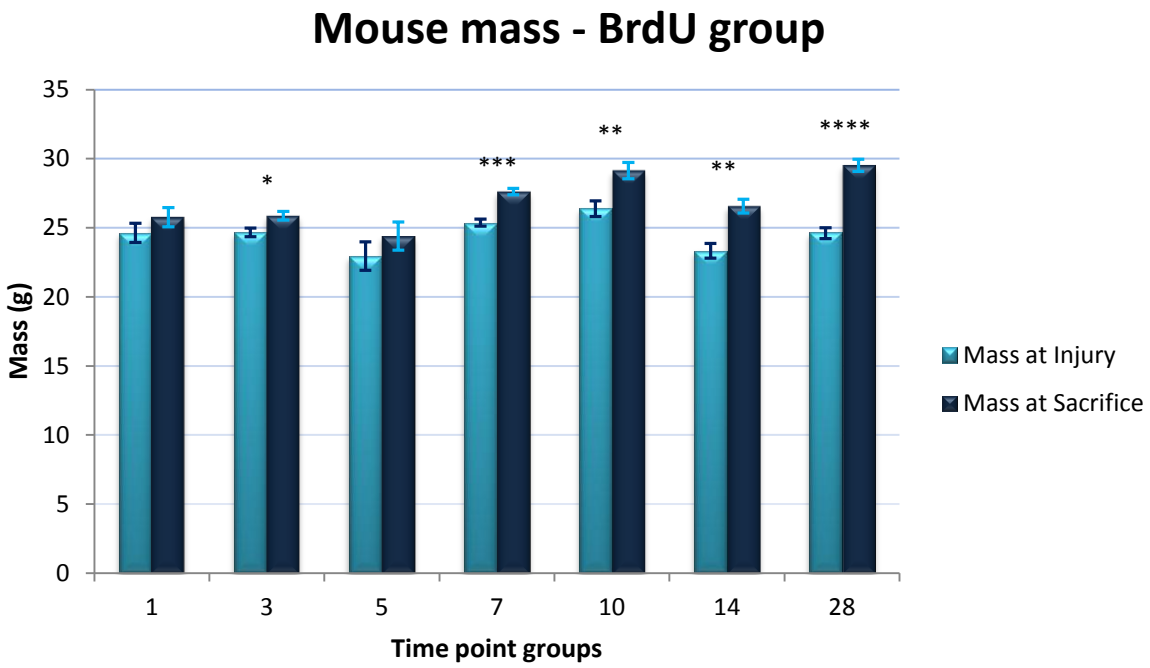

Figure 3.1.2 **Changes in body mass over time, for mice sacrificed between 1 and 28 days post-injury**. Data are presented as means of body mass for n=6 mice per bar, with Standard error. Each group was weighed on the day of injury (pale blue) and the day of sacrifice (dark blue). Stars indicate degree of significance: * (p<0.05); ** (p<0.01); *** (p<0.001) within group from pre-injury to sacrifice.

3.2 Gene expression

3.2.1 AChR-γ: qPCR readings

Plates run for target gene AChR-γ contained very few acceptable cycle threshold (CT) readings (see Figure 3.2.1).

All other groups had n ≥ 2 acceptable readings. Thus data for AChR-γ was not analysed further.

3.2.2 AChR-ε: qPCR readings

In the first week following muscle contusion injury, the expression of AChR-ε subunits in the injured (GI) remained low (See Figure 3.2.2). However, CT values for AChR-ε subunit mRNA in the injured *gastrocnemius* were significantly higher 7 days post-injury (1.598; $p < 0.01$) compared to earlier time points, with nearly a 5-fold increase from day 1 (0.3327; $p < 0.0001$) and a >3-fold increase from days 3 (0.5237) and day 5 (0.4143) to day 7 ($p < 0.01$). Expression levels in GN decreased on day 10 to similar levels to the earlier time points. However, at day 14 levels increased significantly again (day1 vs D14 and day 5 vs day 14; $p < 0.05$) (see Figure 3.2.2).

In the non-injured *gastrocnemius* (GN) expression levels remained low for the first 5 days (CT values were 0.4832; 0.4347 and 0.4725 for days 1, 3 and 5 respectively).As with the GI group, AChR- ε subunit expression peaked at day 7, with more than 3 fold increase in comparison to the earlier time points (1.507; $p < 0.05$). Levels further decreased by day 10, remaining significantly different to days 1, 3 and 5 (1.536; $p < 0.01$), with a slight increase at day 14 (0.9813), which did not differ significantly from any of the other groups.

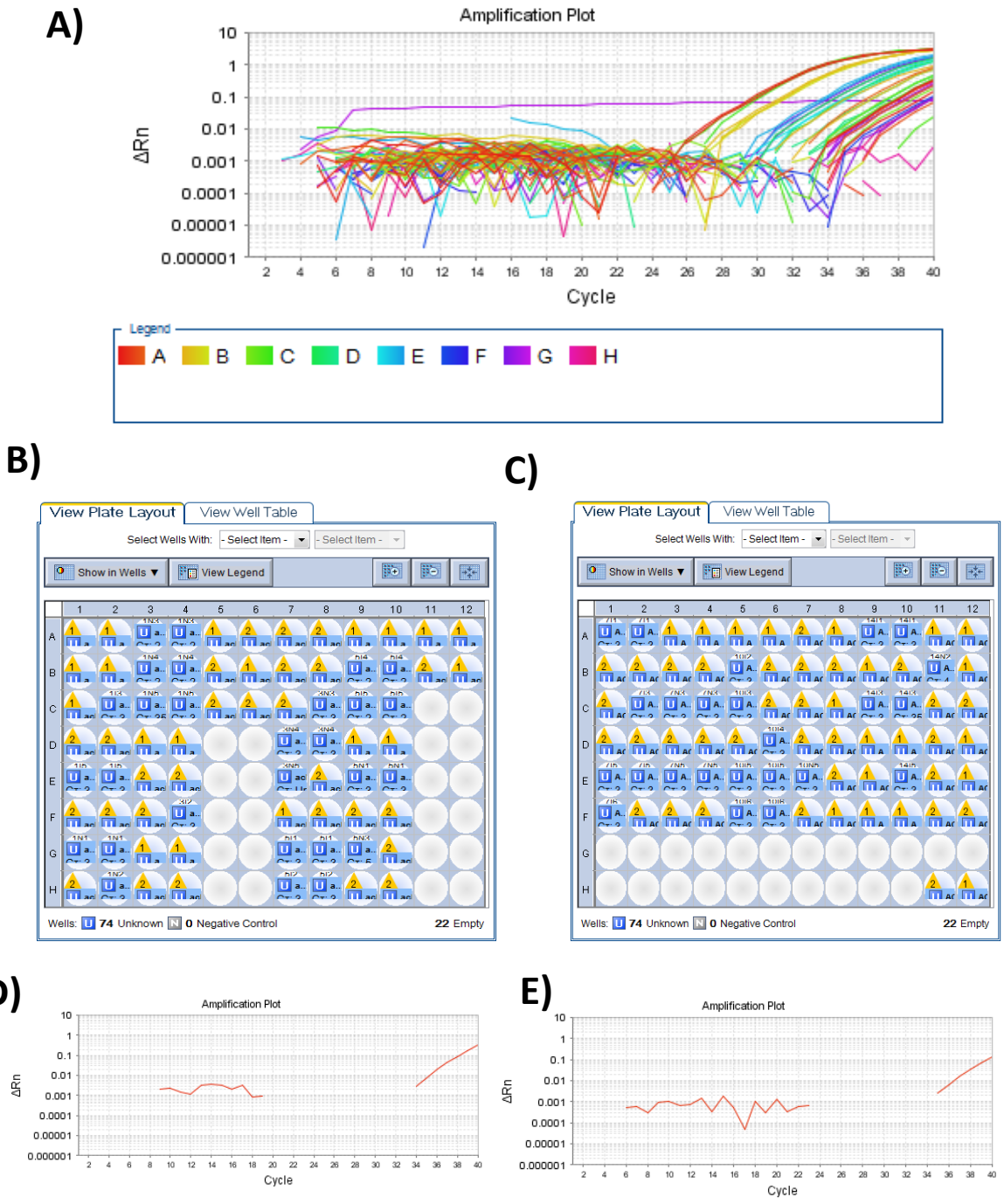

Figure 3.2.1 StepOne® PCR readings of target gene AChR-γ on Plate 1 and 2 (both injured (GI) and non-injured (GN) *gastrocnemius* samples). A) Combined amplification plot of readings of all the plated samples (Plate 1). B) Plate 1 (days 1 – 5) and C) Plate 2 (days 7 - 14) layouts showing sample numbers and outcome of each samples PCR reaction. Yellow flags indicate readings with error. "1" indicates cycle threshold values of sample duplicates differed by ≥1 unit; "2" means CT value was undetermined. Graphs in D and E) show a successful amplification plot for duplicates of the same sample of a single sample of an uninjured gastrocnemius from the day 1 group.

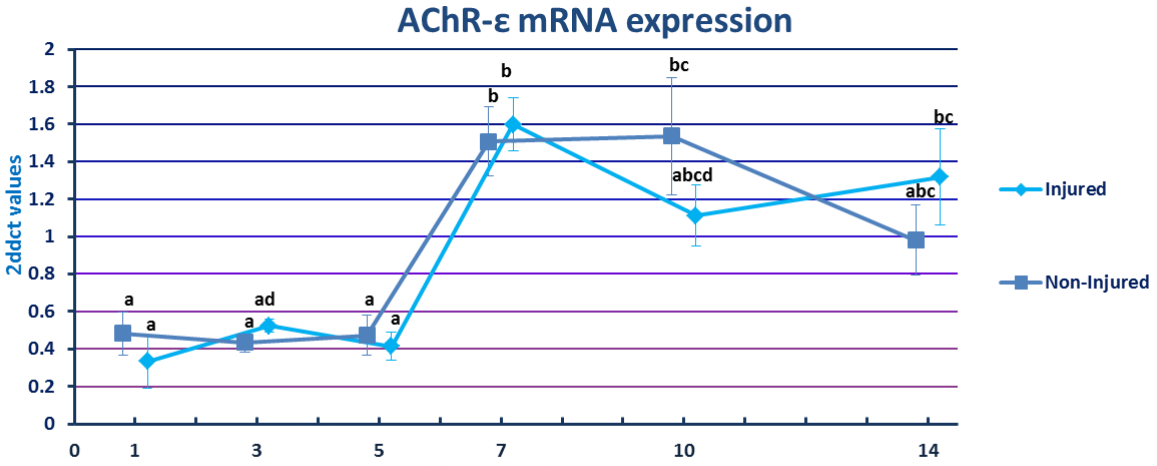

Figure 3.2.2 AChR-ε mRNA expression in the gastrocnemius muscle following muscle contusion injury, with contralateral leg serving as non-injured control. AChR-ε subunit expression in the gastrocnemius muscle following muscle contusion injury in mice. The epsilon subunit levels remained low in the early time points then dramatically increased at 7 days post-injury for both injured and non-injured groups ($p < 0.05$). Injured group decreases on day 10 then increases slightly by day 14. Non-injured group increases marginally on day 10 then decreases noticeably by day 14. GN data is set 0.2 units before and GI 0.2 units after the correct day for ease of viewing.

3.3 Effects of the injury on the structure of the muscle

3.3.1 Effects of the injury on the structure of the non-injured *gastrocnemius*

Non-injured contralateral leg showed organized longitudinal fibres running parallel to one another. Groups of diagonally- and/or cross-sectioned myofibres were visible in the distal areas (near the origin or insertion points or on the borders of the section) in most of the samples. Eosin stained fibres appeared intact, with the exception of some samples that exhibited freeze fracture, particularly on the exterior portions of the cryo-preserved muscle. Connective tissue separated medial and lateral heads of the *gastrocnemius* and tendons were visible as large circular entities with dark pink-stained, wavy interiors of collagen fibres, surrounded by a lighter stained tendon sheath. Haematoxylin stained oval shaped myonuclei were present, spaciously arranged along the borders of the myofibres while rounded blood cell nuclei were only present in large numbers inside the blood vessels (visible as dark pink-stained rings of epithelium brimming with purple-stained nuclei) (See Figure 3.3.1.1).

Longitudinally sectioned *gastrocnemius* samples stained immunohistochemically for laminin and nuclei showed clear, straight, largely uninterrupted lines of laminin, lined with rows of myonuclei – adequately spaced from one another (see Figure 3.3.1.2).

3.3.2 Effects of the injury on the structure of the injured *gastrocnemius* (GI)

3.3.2.1 Border zones

The border zone surrounds the area that received direct impact from the muscle contusion injury. The tissues in this zone are also affected by the injury but to a lesser extent than those receiving the direct injury. The border zone shows predominantly intact, organised fibres with some evidence of fibre tearing and regeneration (see Figure 3.3.3 A). Nuclei of blood cells are restricted to blood vessels although some smaller collections of infiltrating immune cells may be found in regenerating areas.

3.3.2.2 Medial head - impact area

The medial head of the *gastrocnemius* received the greatest impact from the contusion injury. Figure 3.3.3 B shows a severely impacted area, 14 days post injury, where Eosin-staining shows gaps and tears in the myofibres as well as multiple fragments of impacted fibres. Disorganisation and discontinuity of myofibres is evident in these samples. Great immune cell infiltration is observed and close series of Haematoxylin-stained myonuclei align along the longitudinally sectioned, but still fragmented, myofibres.

3.3.2.3 Lateral head – impact area

At 14 days post injury lateral head of the *gastrocnemius* showed more fibre organisation than in the medial head, with a more advanced stage of muscle regeneration and fewer myofibre fragments (see Figure 3.3.4). Larger numbers of infiltrating immune cells are present in comparison to the medial head. Numerous areas where myonuclei have lined up in series along the regenerating myofibre are seen.

Injured samples from the impact zone of the medial head, were prepared immunohistochemically and imaged to reveal sections with discontinuous portions of damaged fibres. Swelling fibres with large areas of oedema are evident. Sealing off of torn myofibres, scar tissue formation (parenthesis) and fibrosis occur in some areas (see Figure 3.3.2.3).

3.4 BrdU incorporation

Mice in Group B were injured on one limb after mini-osmotic pump insertion. More $BrdU^+$ nuclei were seen in blood cells than in the pool of myonuclei in the first few days, although later, more myonuclei were stained positively for BrdU. All images shown in this section are from injured *gastrocnemius* muscle.

3.4.1 Blood cells indicating BrdU uptake

At 3 days post injury, the proportion of $BrdU^+$ cells in the blood stream is low (see Figure 3.4.1). By 7 and 14 days post injury $BrdU^+$ nuclei represent about half of the total blood cell nuclei visible (see Figure 3.4.2 and 3.4.3 as well as Video 1 on accompanying disc).

3.4.2 Presence of BrdU positive nuclei in myofibres

At 3 days post injury, very little $BrdU^+$ cells were observed along the myofibres (see Figure 3.4.1). At day 5, individual satellite cells commencing the process of division and proliferation can be located (see Figure 3.4.4). By day 14, scores of oval shaped $BrdU^+$ myonuclei occupy regenerating and regenerated myofibres (see Figure 3.4.5). $BrdU^+$ satellite cells can be seen between the ends of torn myofibres, (see Figure 3.4.6).

3.5 Neuromuscular junction appearance and location

3.5.1 Cross-sectional view

NMJs appeared as crescent-shaped entities in muscle cross sections, curving around the cylindrical myofibres (see Figure 3.5.1). NMJs of myofibres were present in sections taken from the middle portion of the cryo-frozen muscle sample.

3.5.2 Longitudinal view

NMJs visible in their classic coral-like formations in longitudinally sectioned muscle samples. NMJs are arranged along a central band - easily demonstrated in smaller muscles such as the *plantaris* (see Figure 3.5.2 and Video 4 on accompanying disc). Tile scans of entire *gastrocnemius* muscle showed NMJs also aligned in bands, but it proved more difficult to show the central position of NMJs in the larger muscle (see Figure 3.5.3).

Some NMJs where only the top or bottom ends of the structure were present on that particular section were noted as small articles of fluorescence where only one or two junctional folds were evident (see 3D Figures in Section 3.5.4).

3.5.3 3D imaging to investigate the relationship between NMJs and subsynaptic nuclei

3D images of Hoechst stained myonuclei's linear arrangement outlines the borders of the individual myofibres (see Figure 3.5.4). NMJs are visible on their respective fibres in close proximity to one another denoting the central band along which they are arranged. Close up views from various angles as well as videos created by linking the z-stack images in sequence reveal the subsynaptic myonuclei and how the NMJs are moulded over and around these supporting nuclei (see Video 2 and 3 on accompanying disc).

3.5.4 3D imaging to investigate NMJ structure

Close up 3D images of intact NMJs reveal the intricate organisation of its junctional folds (see Figure 3.5.5, A and B). Most NMJs observed portrayed the classic coral-like formation, while some NMJs displayed straighter processes with less folding (see Figure 3.5.5, C and D). Upon closer inspection, thin lines are etched out along the NMJ surface (see Figure 3.5.6).

3.5.5 Changes in NMJ structures in contusion injured muscle

Injured NMJ were discernible by their lack of organised (mature) structure as well as presence of scattered AChRs on the sarcolemma on either side of the myofibre (see Figure 3.5.7), or in the general area of the damaged NMJ if the surrounding membrane was disorganised.

3.6 Time-dependent changes in NMJ morphology post contusion injury

Uninjured and injured NMJs from mice days 0, 5, 7 and 14 (mouse: n = 1; slide: n = 1) were imaged and classified into categories in order to describe and compare the morphology of an intact, damaged and regenerating NMJ. A total number of 21 NMJs were analysed.

3.6.1 Coral-like structure of NMJs in intact uninjured muscle (n = 1)

The intact NMJ structure is well-organised, displaying clear junctional folds (see Figure 3.6.1). Surfaces seen on the 3D render appear smoother than in NMJs visualized on injured samples.

3.6.2 Different degrees of fracturing and damage, 5 days post injury (n = 5)

Two NMJs in see Figure 3.6.2 appear visible along the edge of the sarcolemma appear long, straight and thin with few junctional folds in confocal microscopy (referred to as Side view). A 3D rendered image reveals some junctional folds on both NMJs viewed in the side orientation. NMJ 1 displays a more scattered version of an NMJ in side view than NMJ 2.

NMJ 1 and NMJ 2 in Figure 3.6.3 show a cohesive structural arrangement in *en face* view, but reveal a more jagged appearance in the 3D render than that of the intact NMJ. NMJ 2 shows scattering of AChRs on the far ends of the structure. NMJ 3 shows complete fracturing of the structure while retaining traces of the junctional fold arrangement.

3.6.3 Severe damage and disintegration of NMJs, 7 days post injury (n = 4)

NMJs appear scattered, are faint and show little form in confocal and super-resolution images (see Figure 3.6.4). The 3D rendered image reveals severe fragmentation as well as separation of entire sections of AChRs, as in NMJ 2. In NMJ 4 - the smallest structure - only three tiny clusters of AChRs are seen. These NMJs demonstrate the worst signs of damage between the injured groups.

3.6.4 Varying degrees of repair and regeneration of NMJ structure, 14 days post injury (n = 11)

In Figure 3.6.5 *en face* NMJ 1 shows some regained structure but lacks organisation. Increased magnification shows lack of complex organisation in NMJ 1 and scattered laminin deposits. 3D rendered images reveal deeper levels of organisation, but also expose scatterings of AChRs.

The confocal and super-resolution images in Figure 3.6.6 show two *en face* NMJs that appear organised and robust, but denser than the uninjured NMJ from Figure 3.6.1. 3D renders reveal a considerable structural depth for these NMJs, indicating a greater number of AChRs in these regenerating NMJs than in the uninjured NMJ. NMJ 1 in Figure 3.6.6 shows some extending processes combined with its traditional junctional folding. The NMJ in Figure 3.6.7 exhibits solely extended processes (i.e. no junctional folds), but occupies similar space and depth as its *en face* counterparts.

In Figure 3.6.8, *en* face NMJ 1 has repaired itself robustly and with some organisation although it appears to still be in the process of regrouping its fragments. It is likely that the strip of NMJ 2 could be fragments separated from the NMJ 1 upon injury, but not completely destroyed.

The NMJs in Figure 3.6.9 are scarcely visible, identified by minute, separated assortments of AChRs reaching across the myofibres. 3D renders revealed very little depth to these NMJs and they were categorised as Tip NMJs.

NMJs in different orientations were also seen in the day 14 group. NMJ 2 in Figure 3.6.5 shows a NMJ in a diagonally sectioned orientation. This NMJ's shape is sharply concave and 3D render shows considerable depth of structure, along with a great deal of scattered AChRs – characteristic of a damaged NMJ. An NMJ sectioned in a position in between a side view and an *en face* view was

captured with its processes wrapping around the myofibre (see Figure 3.6.10 A). However, these curved processes were not visible in the super resolution image and thus also not visible in the 3D render (see Figure 3.6.10 B and C).

3.7 Time-dependent changes in NMJ surface area and volume measurements post-contusion injury

A trend of decreased surface area and volume was seen in the injured day 7 NMJs in comparison with the intact NMJ. However, in regenerating day 14 NMJs surface area and volume measurements were higher than the intact sample. Table 3.1 contains surface area and volume measurements for all the NMJs analysed in this study.

3.7.1 Surface area

In comparison over time (see Figure 3.7.1), the day 5 group's NMJ surface area was similar to that of the uninjured specimen (Uninjured NMJ average = 96.4 μm^2; Day 5 Injured NMJ average = 103.5 μm^2); surface area was markedly decreased on day 7 (39.9 μm^2); and was highest overall on day 14 post injury (average = 160.0 μm^2).

Considering the various categories of NMJ views, the *en face* NMJs possessed the greatest surface areas with measurements ranging from 96.4 μm^2 to 222.9 μm^2 (See Table 3.1 and Figure 3.8.1), with the exception of sample from day 5 NMJ 3 (53.5 μm^2). NMJs in other orientations/categories (namely, Around, Side and Diagonal Section) fell within a decreased surface area range (between 25.9 – 57.3 μm^2).

NMJs in Tip categories represented incomplete structures and were henceforth excluded from further comparison with the NMJs showing complete structures.

3.7.2 Volume

The intact NMJ in *en face* orientation occupied the lowest volume in their category with a measurement of 10 762 μm^3, which fell generally in the lower overall range of the NMJ volumes (see Table 3.1 and Figure 3.9.2). At day 5 post injury, *en face* NMJ 1 and 3 remained level with the uninjured NMJ (15 283 μm^3 and 12 767 μm^3 respectively), while NMJ 2 displayed an inflated value of 43 961 μm^3. Day 7 NMJs showed a slightly decreased range (averaging 8 670 μm^3) - the average being drastically increased by NMJ 2, adding a volume of 200 90 μm^3 to the equation. The remainder of the NMJs 1 3 and 4 showed lower values (6 436 μm^3; 6 241 μm^3 and 1 914 μm^3 respectively) -

depicting a trend in agreement to what is seen in the surface area measurements. Volumes for day 14 NMJs larger (averaging 27 299 μm^3) and were more uniform than the aforementioned groups.

The two Side NMJs from day 5 and the Around NMJ from day 14 had low values (Side: 5 825μm^3 and 12 748 μm^3; Around = 7380 μm^3), while the Diagonally sectioned NMJ had a remarkably large volume (22 449 μm^3).

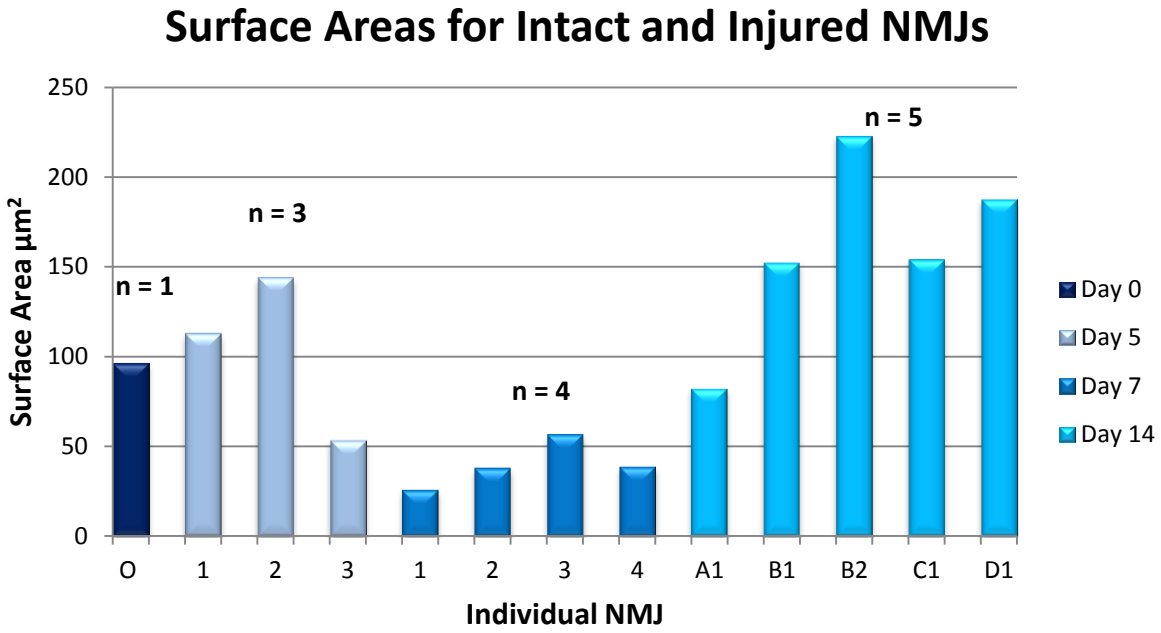

Figure 3.7.1 **Comparison of surface areas for intact and injured NMJs over time.** Surface areas for *en face* NMJs at day 5 post injury remain constant, then decrease on day 7 with an exaggerated increase by day 14, in comparison to the uninjured NMJ. NMJ numbers correlate with those seen on the microscopy images. NMJs were selected from n = 1 mouse (muscle section: n =1) for each time point. In the day 14 group, A refers to Fig. 3.7.5; B to Fig. 3.7.6; C to Fig. 3.7.7 and D to Fig. 3.7.8. Surface area was determined by measuring positive threshold on Image J version 1.47 software.

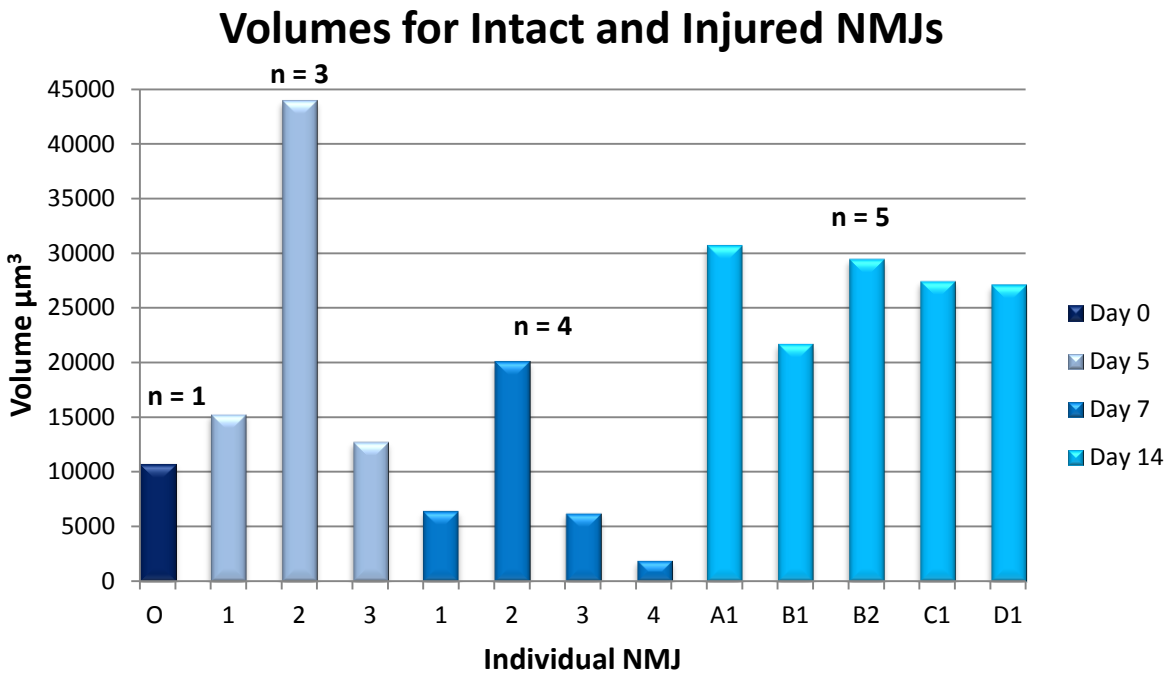

Figure 3.7.2 **Comparison of volumes for intact and injured NMJs over time.** Surface areas for *en face* NMJs at day 5 post injury remain constant (with the exception of NMJ 2), and then decrease on day 7 (except NMJ 2), where after there is an exaggerated increase by day 14, in comparison to the uninjured NMJ. NMJ numbers correlate with those seen on the microscopy images. NMJs were selected from n = 1 mouse (muscle section: n =1) for each time point. In the day 14 group, A refers to Fig. 3.7.5; B to Fig. 3.7.6; C to Fig. 3.7.7 and D to Fig. 3.7.8. Volume was determined by measuring positive threshold of a 3D render of the image on VGStudioMax 2.2 software.

3.7.3 Variation of z-stacks

Volumes were divided by the number of z-stacks they encompassed obtain the average volume per Z-level. This illuminates the compactness or density of NMJs within the third dimension.

The intact NMJ now had one of the highest densities in comparison with the other NMJs, presenting a value of 357 μm^3 per Z layer. NMJ C from 14 days post injury had a density of 517 μm^3 per Z-layer – a value far above the remainder of the NMJs in the day 14 Group as well as the uninjured NMJ.

Day 7 post injury NMJs had lower densities: NMJ 4 had the lowest value of the day 7 post injury group at 70 μm^3 and NMJ 3 had the highest value at 231 μm^3. The diagonally sectioned NMJ 2 had the lowest normalized volume with 21 μm^3.

Table 3.1 Surface area; volume, z-stack number and volume/z-stack values of categorised NMJs

NMJ Identity	Category	Area μm^2	Volume μm^3	z-Stack nr	V^3/ZS
Uninjured	*En face*	96.4	10 726	30	357
Day 5 NMJ 1	*En face* /Border zone	112.9	15 283	52	293
Day 5 NMJ 2	*En face*, Border zone	144.0	43 961	57	771
Day 5 NMJ 3	*En face*, Border zone	53.5	12 767	57	223
Day 7 NMJ 1	*En face*, Scattered	25.9	6 436	46	139
Day 7 NMJ 2	*En face*, Scattered	38.0	20 090	93	216
Day 7 NMJ 3	*En face*, Scattered	56.8	6 241	27	231
Day 7 NMJ 4	*En face*, Scattered	38.7	1 914	27	70
Day 14 NMJ A1	*En face*	82.4	30 715	102	301
Day 14 NMJ B1	*En face,* Crushed	152.6	21 740	89	244
Day 14 NMJ B2	*En face*	222.9	29 477	89	331
Day 14 NMJ C	*En face,* Extended	154.4	27 450	53	517
Day 14 NMJ D1	*En face*	187.6	27 112	83	326
NMJs in different categories					
Day 5 NMJ 1S	Side	57.3	5 825	91	64
Day 5 NMJ 2S	Side	44.7	12 748	91	140
Day 14 NMJ 1A	Around	29.3	7 380	28	263
Day 14 NMJ 1T	Tip	12.0	4 290	51	84
Day 14 NMJ 2T	Tip	3.5	1 274	51	24
Day 14 NMJ 3T	Tip	15.6	4 277	51	83
Day 14 NMJ A2D	Diagonal Section	49.2	22 449	104	210

3.8 Visualising BrdU and NMJs together

After changing to a two-step staining procedure for α-btx and BrdU as described in Pilot 3 (Section 2.5.3.4), proliferating satellite cells and NMJs could successfully be imaged in the same sample. Due to time constraints, only two samples (the injured and contralateral, non-injured *gastrocnemius* muscles from a mouse in the 14 days post-injury group) was imaged. This time point was selected, because it is expected that the most $BrdU^+$ cells would be found when significant time has passed for cells to have proliferated.

These images show $BrdU^+$ nuclei occupying the same location as some of the subsynaptic nuclei (Figure 3.8.1). In certain areas, NMJs are surrounded by $BrdU^+$ cells in addition to their subsynaptic $BrdU^+$ nuclei. Figure 3.8.2 shows a NMJ with one $BrdU^+$ myonucleus directly beneath it. This myonucleus is enveloped by a covering of laminin, proving that it is a true satellite cell residing beneath the NMJ.

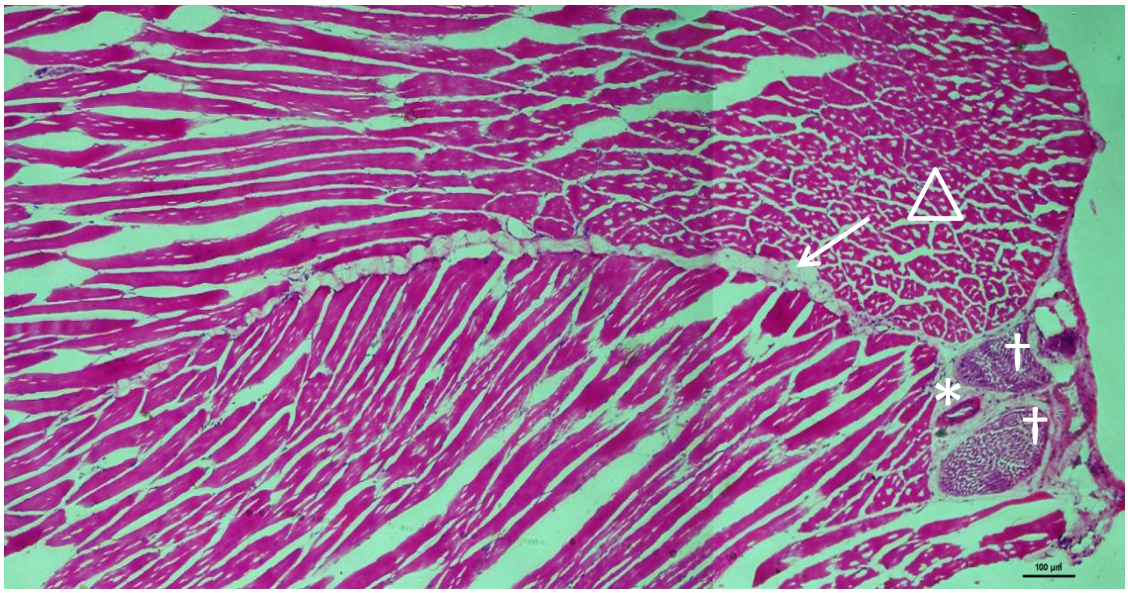

Figure 3.3.1 **Longitudinal section of non-injured *gastrocnemius* muscle** (10x). An arrow indicates the layer of connective tissue dividing the medial and lateral head of the *gastrocnemius*. Some fibres are seen in cross section (Δ). The origin of the muscle shows the cross section of a blood vessel (*) as well as two tendons (†). Scale bar = 100 µm.

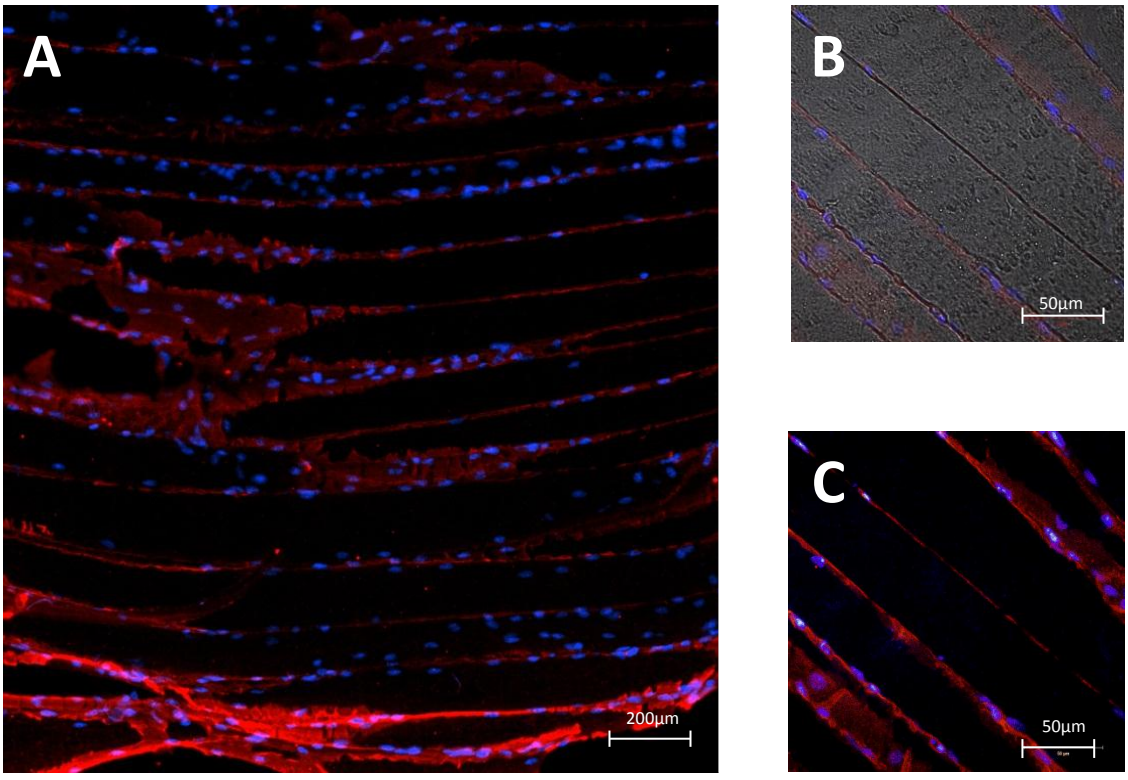

Figure 3.3.2 **Immunofluorescent image of non-injured *gastrocnemius* muscle.** IHC staining with anti-laminin (red) and Hoechst for nuclei (blue) at A) 10x (Scale bar = 200 µm); and B) and C) at 40x magnification (Scale bar = 50 µm). Image B) includes light transmission. Fibres show organised myofibres and myonuclei. Immune cells (*) are restricted to blood vessels.

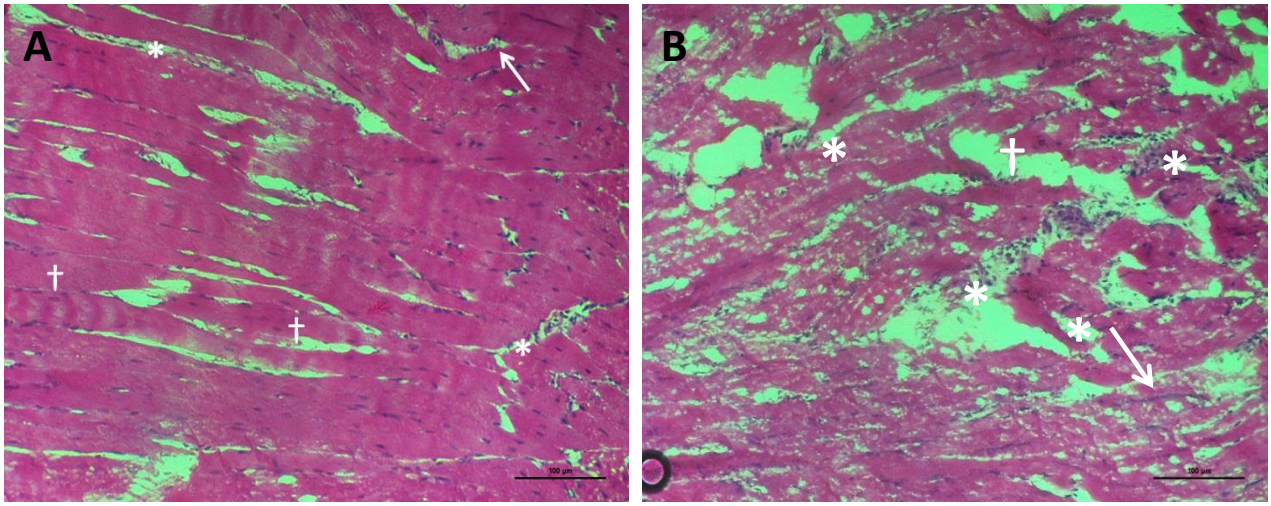

Figure 3.3.3 **H&E stained medial head of injured *gastrocnemius* muscle, 14 days post injury, during regeneration after severe damage (10x magnification).** A) The Border zone shows minor damage. Fibres show a good level of organisation. Immune cells (*) are mainly restricted to blood vessels, although some smaller clusters of infiltrating immune cells are present (arrows). A few central myonuclei (†) are seen while the majority of the myonuclei line myofibre membranes in a normal fashion. B) In the impact zone, severe damage is evident. Fibres are discontinuous and lack organisation. Great numbers of infiltrating immune cells (*) show that debris is still being cleared and presence of central myonuclei (†) indicate myogenesis is at its infant stages. Some myotube formation is perceived along the periphery (white arrows). Scale bar = 100 µm.

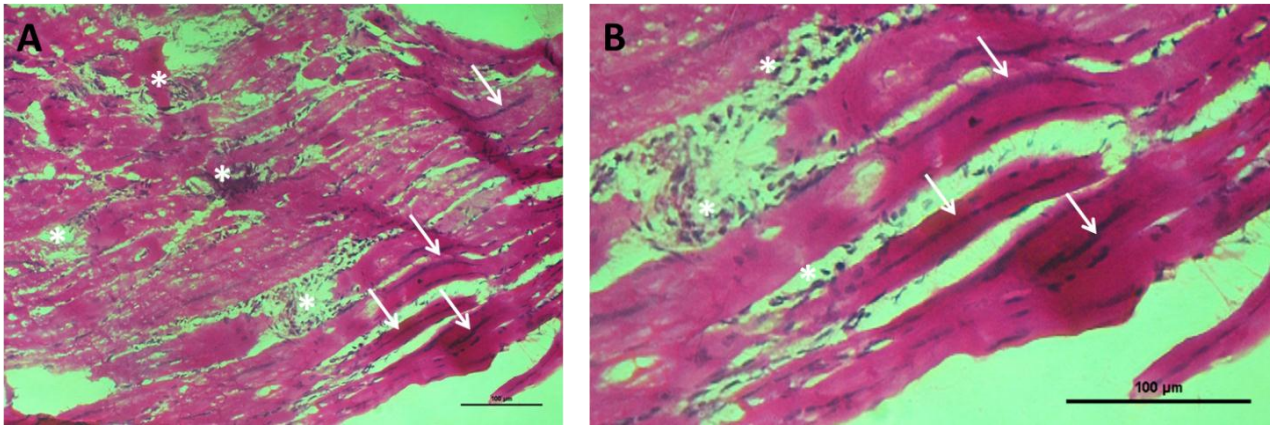

Figure 3.3.4 **H& E stained tissue from the lateral head of injured *gastrocnemius* muscle, 14 days post injury in the impact zone, during regeneration following severe damage (A)** 10x and **B)** 20x magnification**.** Great numbers of nuclei from both infiltrating immune cells (*) and satellite cells/myonuclei (†) are present. Organisation of regenerating fibres is imminent. Some fibres exhibit central alignment of myonuclei along regenerating myofibres (white arrows). Scale bar = 100 µm.

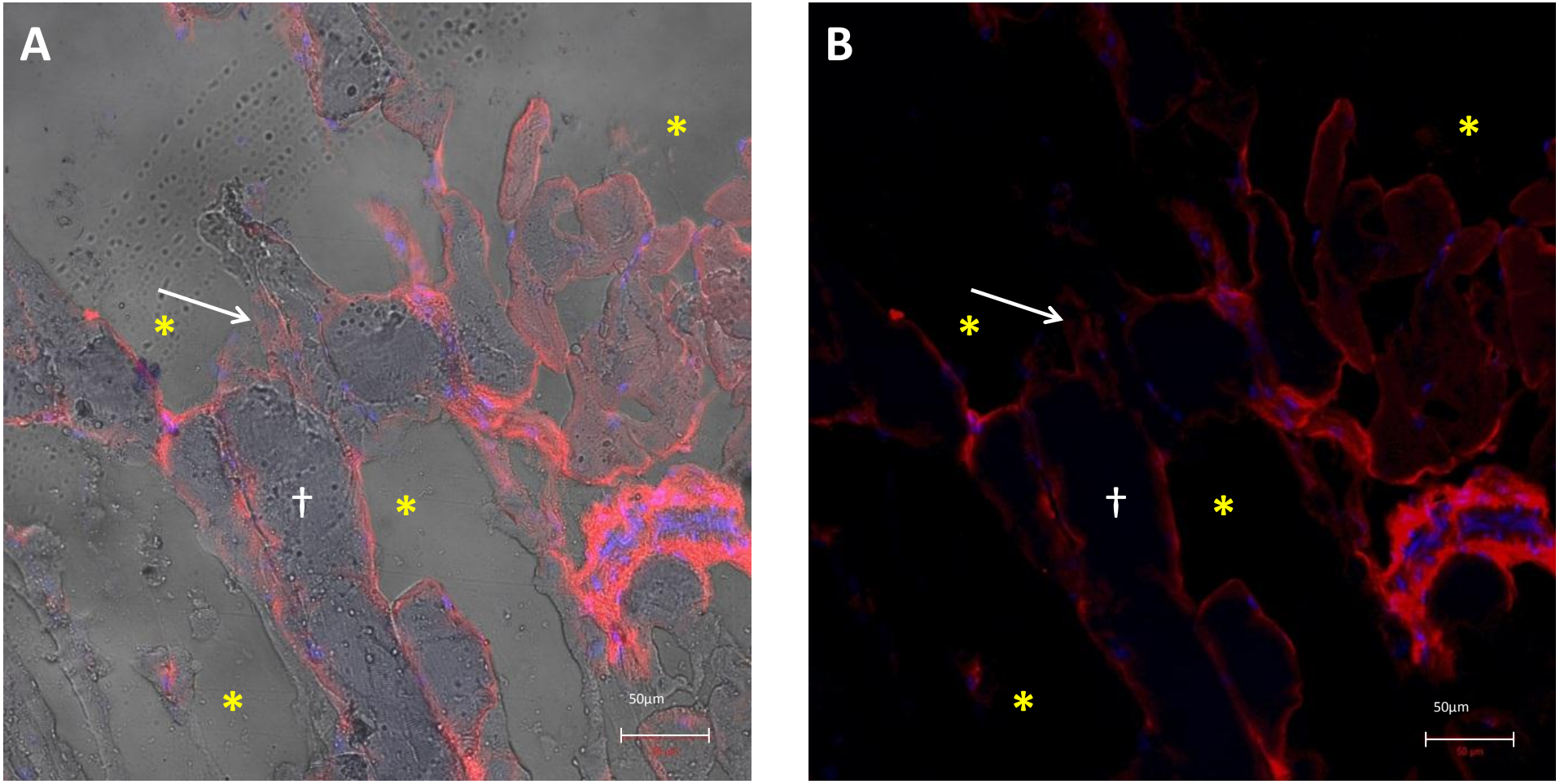

Figure 3.3.5 **Characteristics of a contusion-injured myofibre.** *Gastrocnemius* muscle in longitudinal section 14 days post-injury with immunofluorescence A) with and B) without light transmission. Large areas of oedema (*) with sealing off of injured myofibre (arrows) are present. Necrotic myofibres experience swelling (†). Scar tissue formation (parenthesis) and fibrosis are evident. Scale bar = 50 µm.

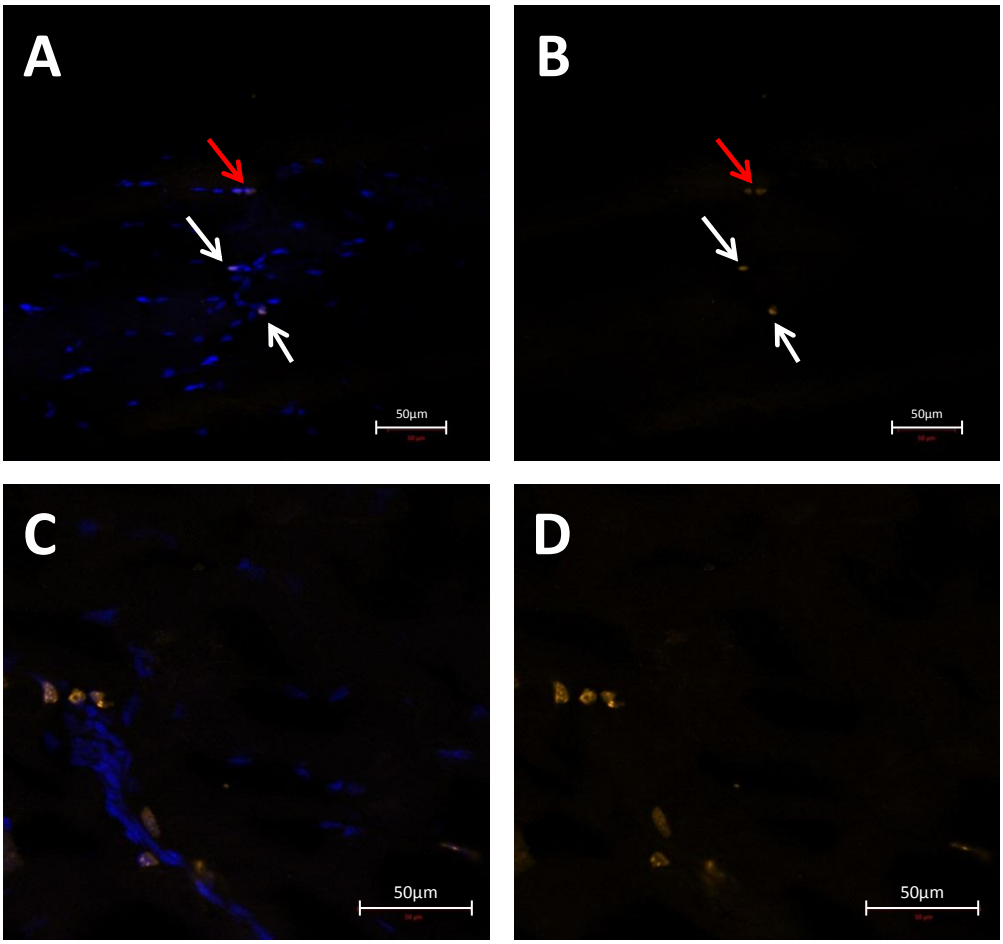

Figure 3.4.1 **BrdU presence in the blood stream in injured *gastrocnemius* muscle tissue, 3 days post injury.** IHC stained with anti-BrdU (orange) for proliferated nuclei and Hoechst (blue) for all nuclei. **A)** and **C)** show both anti-BrdU and Hoechst; **B)** and **D)** shows only anti-BrdU. **A)** and **B)** 20x magnification showing some $BrdU^{+}$ cells (arrows). Red arrow shows two $BrdU^{+}$ cells adjacent to one another indicating that they are daughter cells from the same proliferated satellite cell. **C)** and **D)** 40x magnification showing a blood vessel with relatively few $BrdU^{+}$ cells in comparison with later time points. Scale bar = 50 µm.

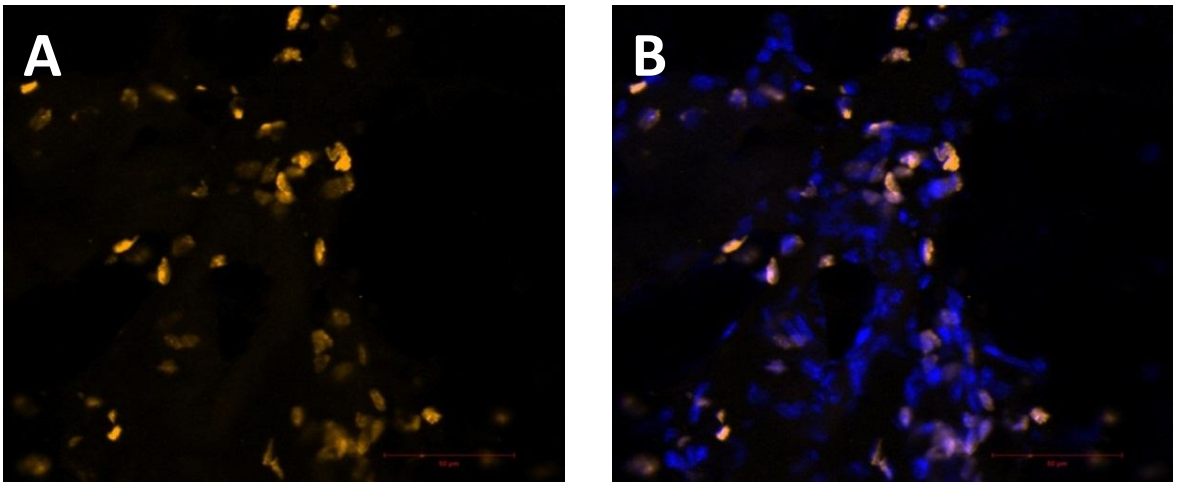

Figure 3.4.2 **BrdU incorporation in blood cells in injured *gastrocnemius* muscle tissue, *7* days post injury.** More nuclei (blue) and BrdU (orange) presence shows a dramatic increase in the efforts of infiltrating immune- and satellite cells to repair myofibre damage and clear debris. Scale bar = 50 µm.

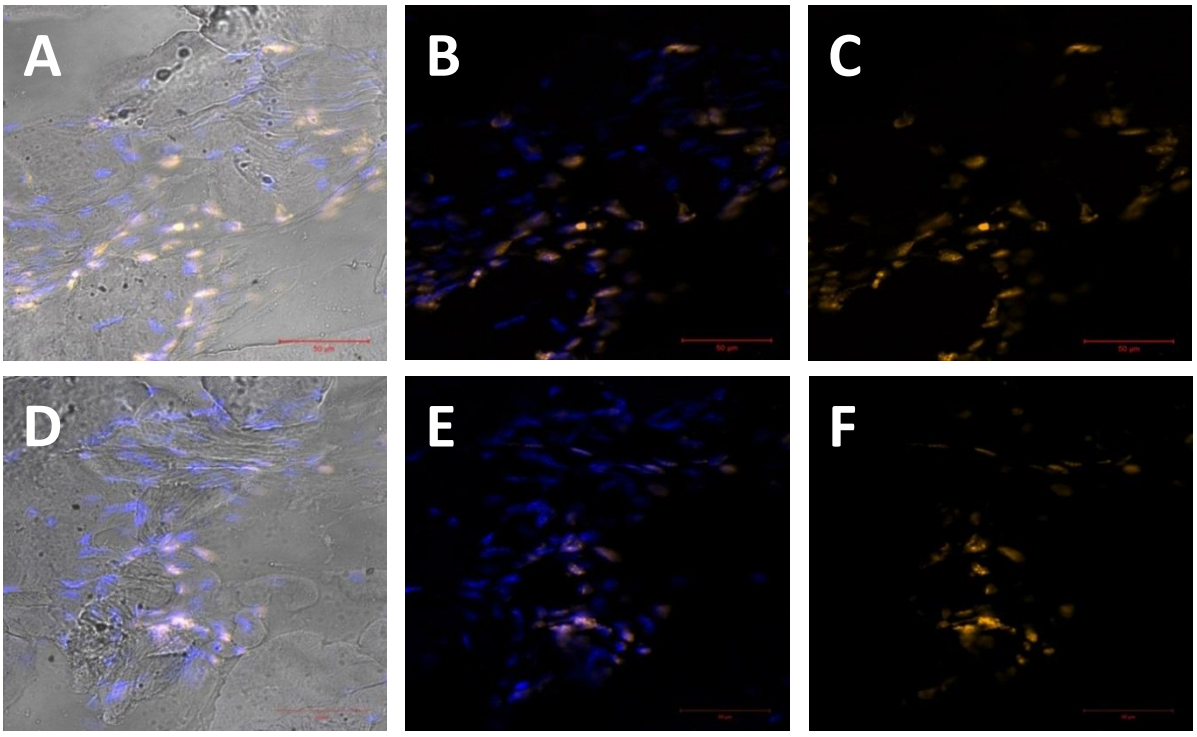

Figure 3.4.3 **BrdU incorporation in blood cells in *gastrocnemius* muscle tissue, 14 days post injury. A)** and **D)** show light transmission, Hoechst (blue) and anti-BrdU (orange); **B) and E)** show Hoechst and anti-BrdU; **C)** and **F)** show only anti-BrdU. An increased presence in $BrdU^{+}$ cells alludes to continued efforts as most of the debris has been cleared away and satellite cells are starting to lay foundations to rebuild damaged myofibres and form new ones if necessary. Scale bar = 50 µm.

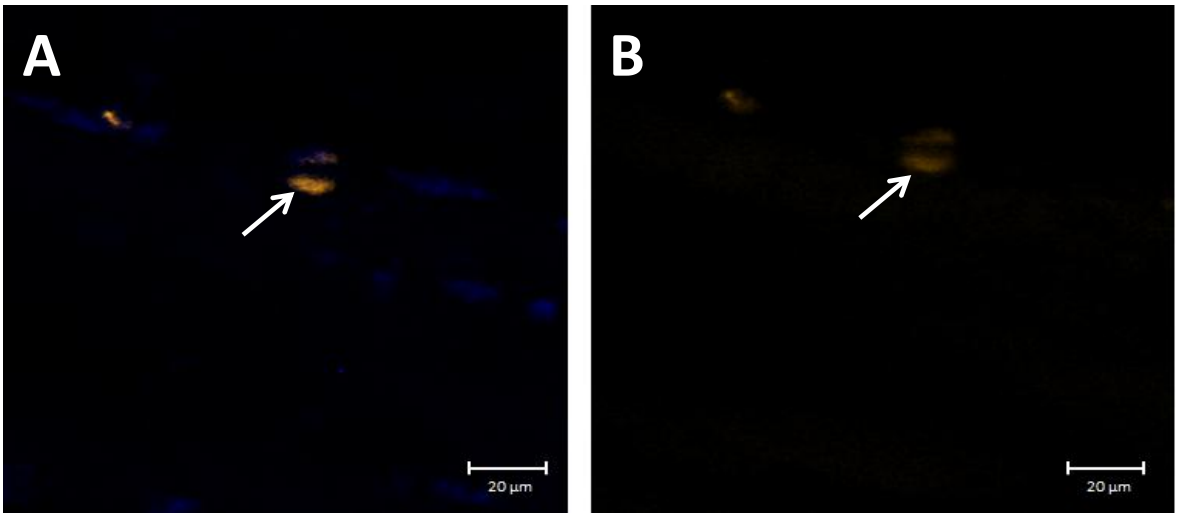

Figure 3.4.4 **A satellite cell undergoing division (white arrow) in *gastrocnemius* muscle, 5 days post injury (40x magnification)**. Two characteristically oval shaped $BrdU^{+}$ nuclei (orange) of satellite daughter cells soon after splitting in order to multiply and repair myofibre damage. **A)** With Hoechst stained nuclei (blue) to overlap BrdU stain confirming accuracy of BrdU detection and **B)** only BrdU. Scale bar = 20 µm.

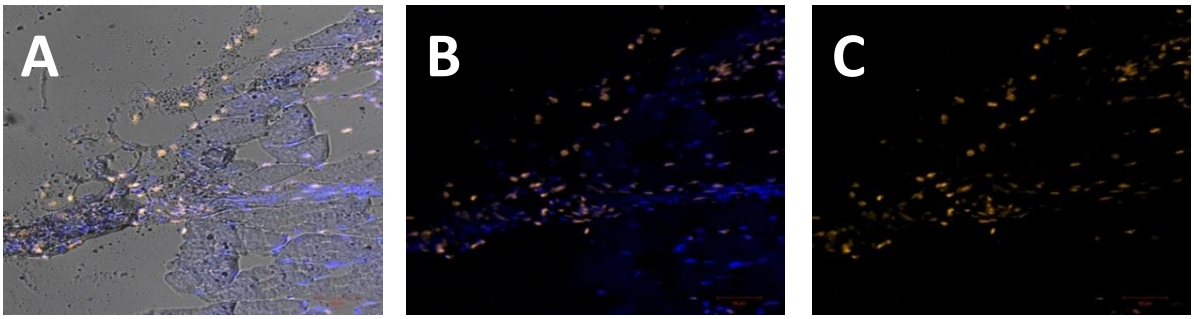

Figure 3.4.5 **BrdU presence in severe contusion injury, 14 days post injury (20x magnification).** Severe damage demands great efforts from the regenerative cells as infiltrating immune cells stream in and satellite cells proliferate considerably to seal off the injured myofibres and undergo recovery construction. Scale bar = 50 µm.

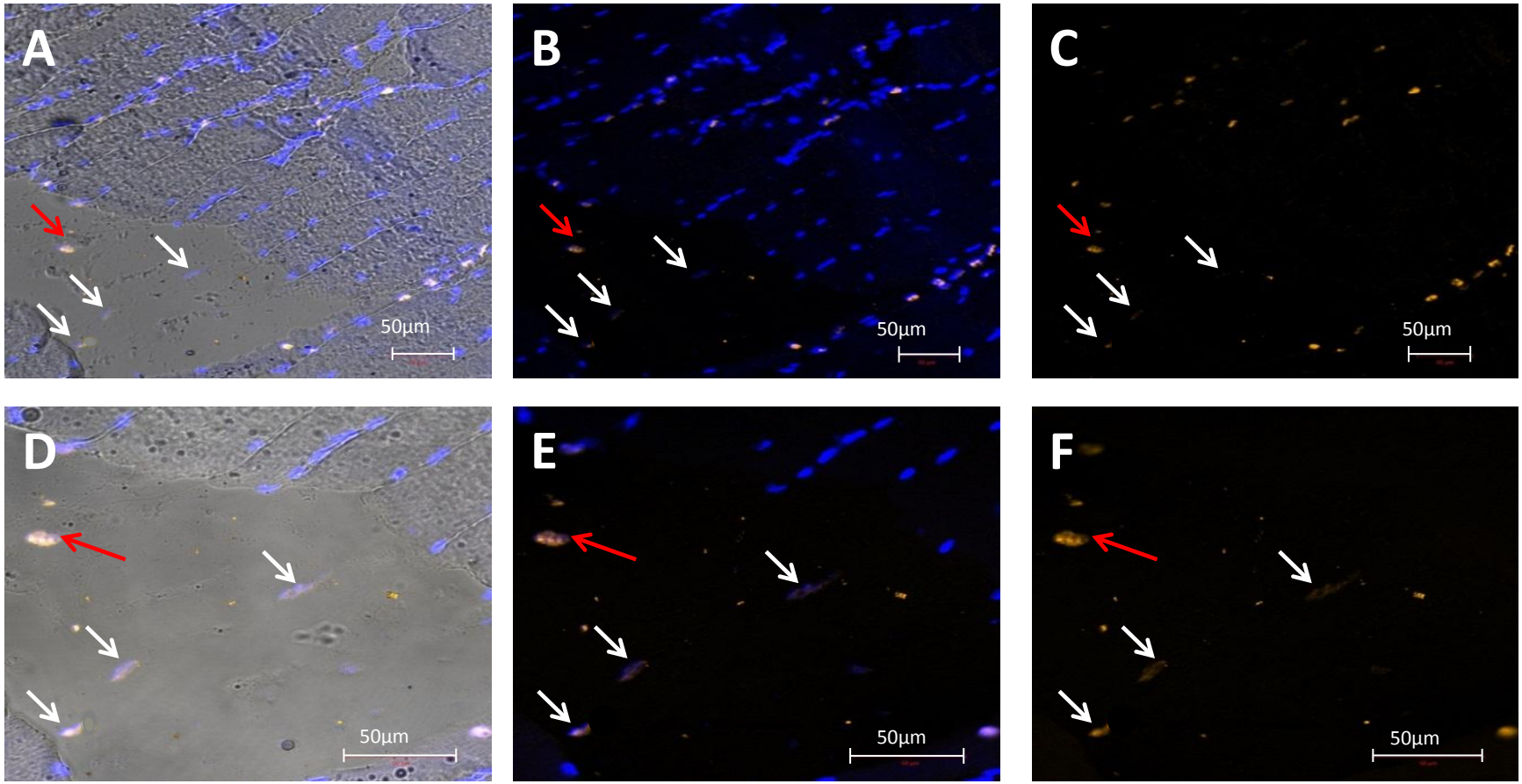

Figure 3.4.6 **Satellite cells in the interstitial space between the ends of damaged fibres**. **A)**, **B)** and **C)** show a 20x magnification and **D)**, **E)** and **F)** show a 40x magnification of the split in myofibres of the medial head of a *gastrocnemius* muscle 14 days post contusion injury. Images show $BrdU^{+}$ satellite cells (white arrows) forming new myotubes to bridge the expanse in an effort to reconnect the opposite ends of torn myofibres. **A)** and **D)** include light transmission while **B)**, **C)** , **E)** and **F)** show only IHC staining with anti-BrdU (orange) and Hoechst (blue). Red arrow shows and $BrdU^{+}$ immune cell, which is distinguishable from the satellite cells due to its rounded (instead of oval) shape. Scale bar = 50 µm.

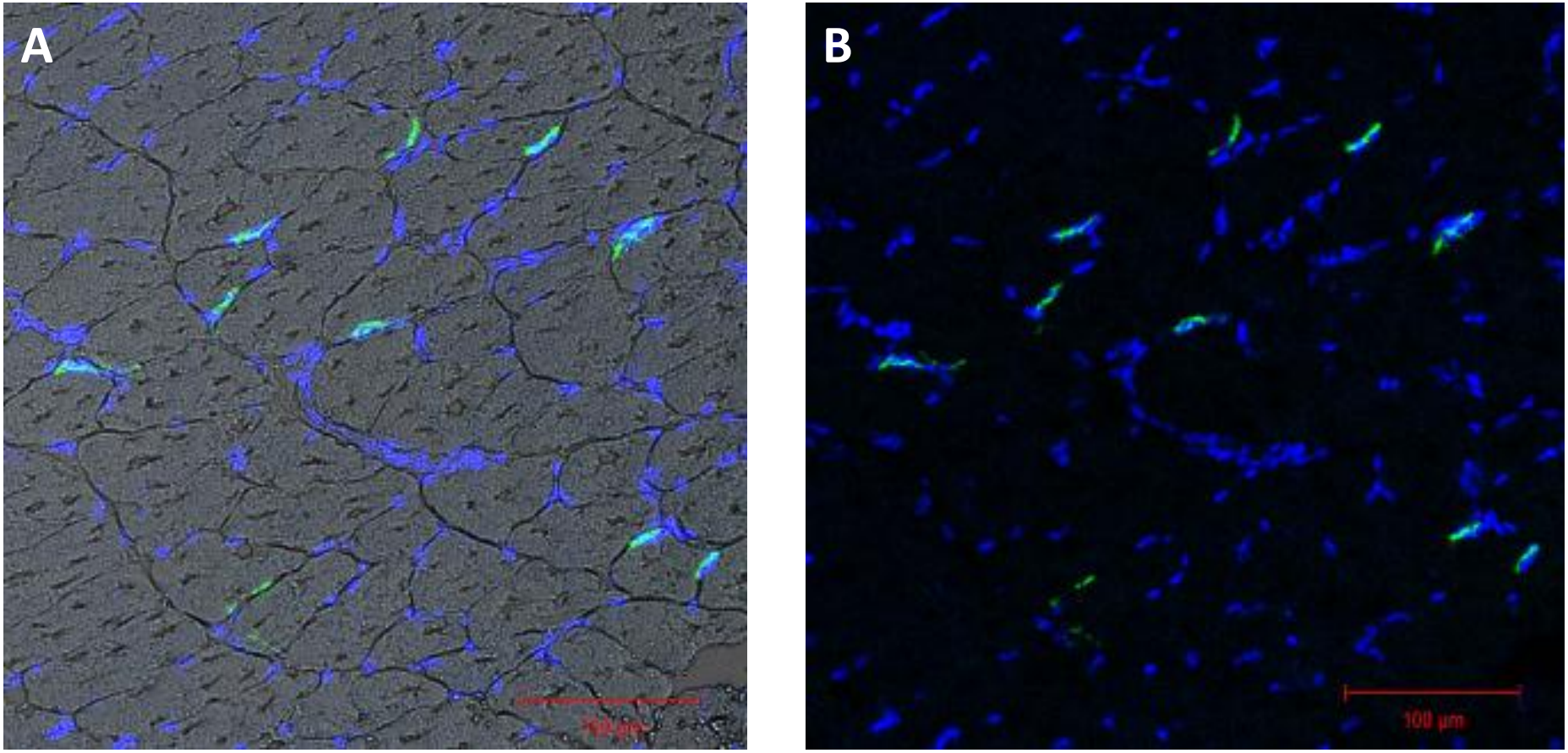

Figure 3.*5.1* **Intact *gastrocnemius* muscle depicting central location of NMJ in cross section (20x magnification). A)** Image with light transmission and **B)** solely immunofluorescent image, stained with α-bungarotoxin (green) for AChRs and Hoecsht (blue) for nuclei. Crescent-shaped NMJs are seen wrapping themselves around the curve of the cylindrical myofibre. Imaged on Carl Zeis LSM 780 confocal microscope. Scale bar = 100 µm.

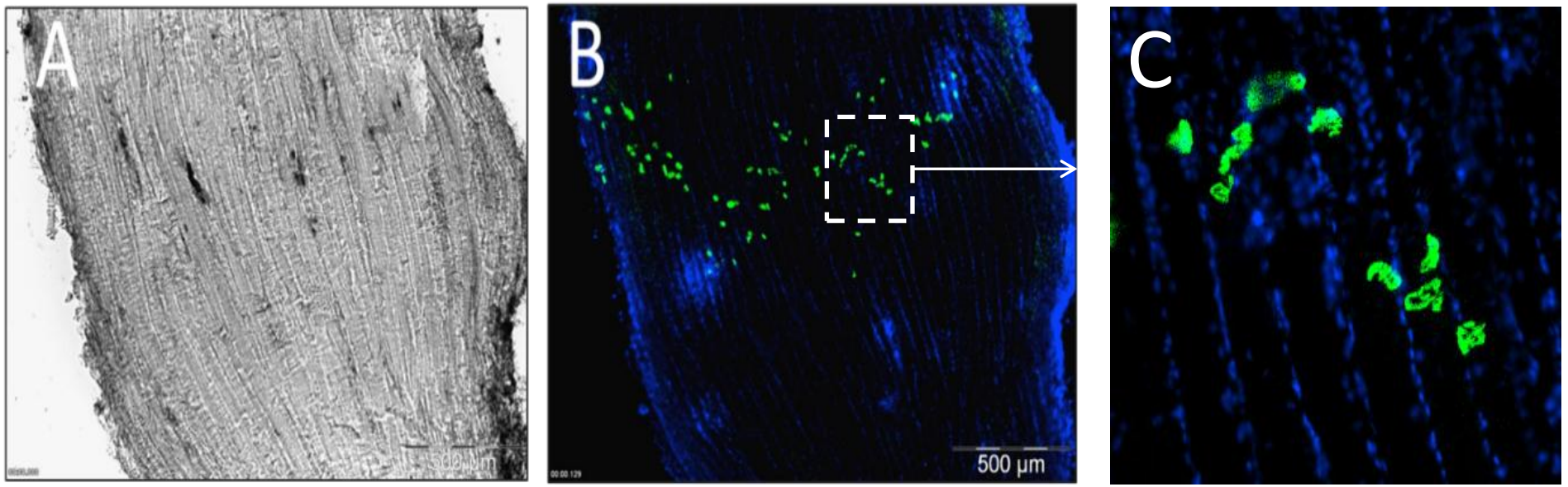

Figure 3.5.2 **Intact *plantaris* muscle depicting central location of NMJ in longitudinal section. A)** Light transmission image of myofibres in longitudinal section (4x magnification) **B)** Immunofluorescent image of same section stained with α-bungarotoxin (green) for AChRs and Hoechst (blue) for nuclei (20x magnification) (Scale bar = 500 µm). **C)** Zoomed in image of **A)**. Imaged on Olympus IX81 Wide field microscope.

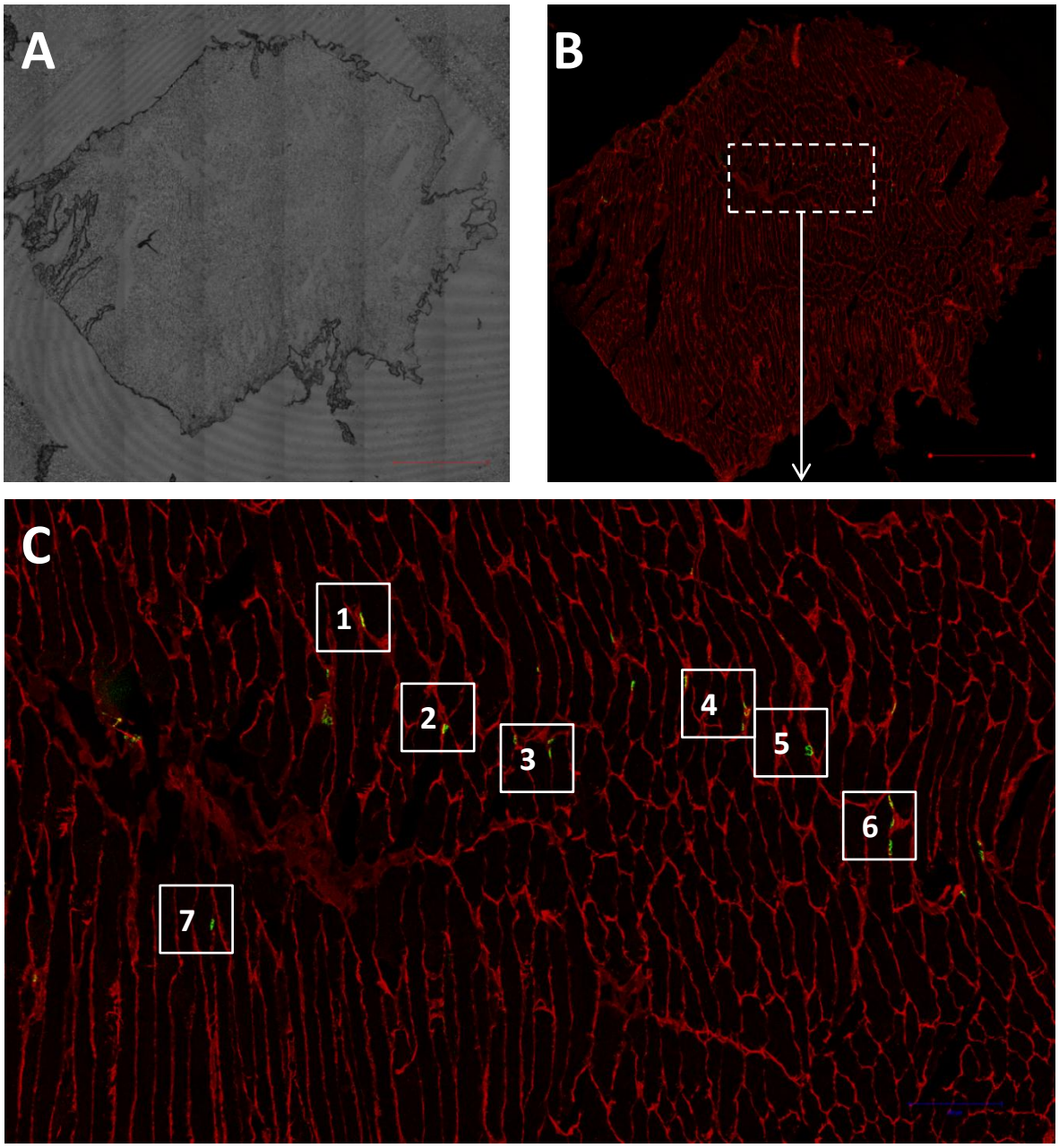

Figure 3.5.3 **Tile scans of the whole *gastrocnemius* section to locate NMJs and see arrangement along muscle.** 7x7 Tile scan at 10x magnification of non-injured *gastrocnemius* sample, 14 Days post injury. **A)** Light microscopy and **B)** anti-laminin (red) and α-btx (green) (Scale bar = 1 000 µm). **C)** Shows a zoomed in view of B) and NMJs are bordered with a block and assigned a reference number Scale bar = 500 µm. A few selected NMJs are numbered here for convenience of viewing.

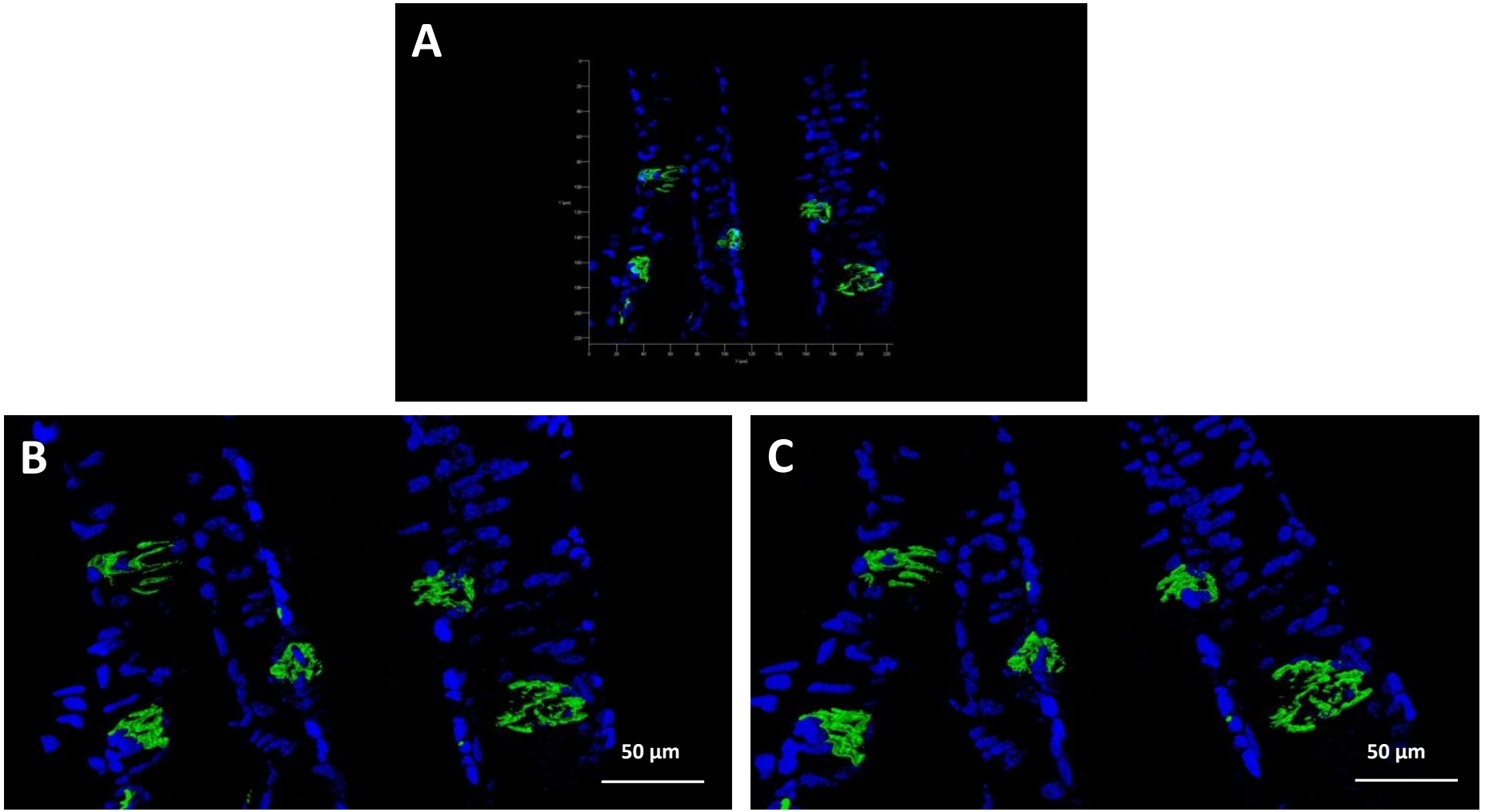

Figure 3.5.4 **Myonuclei's intimate relationship with the NMJ (40x magnification). A)** 3D image of intact *plantaris* muscle, stained with α-bungarotoxin (green) for AChRs and Hoescht (blue) for nuclei. **B)** and **C)** Digitally zoomed views of A) viewed at different angles for better perception of the NMJ structure. Note how nuclei positioning represents the cylindrical myofibres and how NMJ is moulded around subsynaptic nuclei. Images taken on Zeiss LSM 780 confocal microscope. All images were taken as a series of z-stacks and combined to create a 3D image. Scale bar = 50 µm.

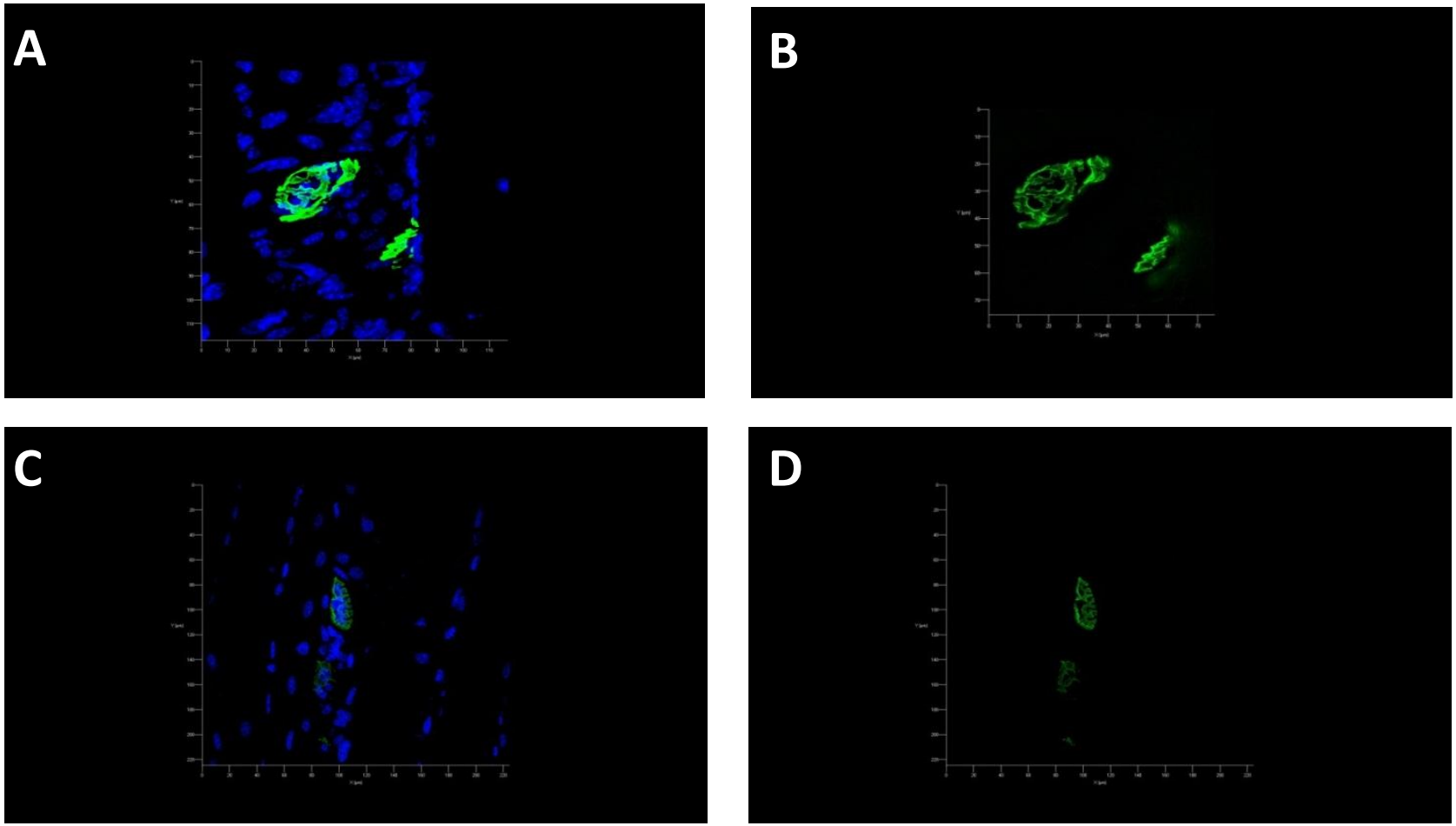

Figure 3.5.5 **3D depictions of NMJs highlighting the junctional folds A)** Confocal microscopy image of intact *plantaris* muscle, stained with α-bungarotoxin (green) and Hoechst (blue) (40x magnification). **B)** Super-resolution image of the same NMJ with α-bungarotoxin (green) (63x magnification). The intricate arrangements of AChRs making up the junctional folds can be seen in detail at this magnification. This arrangement results in the coral-like appearance of the NMJ. A different α-btx stained NMJ from the same section displays less intertwined folding than A), shown in **C)** with confocal microscopy, which includes Hoechst staining (blue) and **D**) with super-resolution microscopy. Imaged on Zeiss LSM 780 confocal microscope with Elyra S1 Super Resolution Platform. All images were taken as a series of z-stacks and combined to create a 3D image with structured illumination.

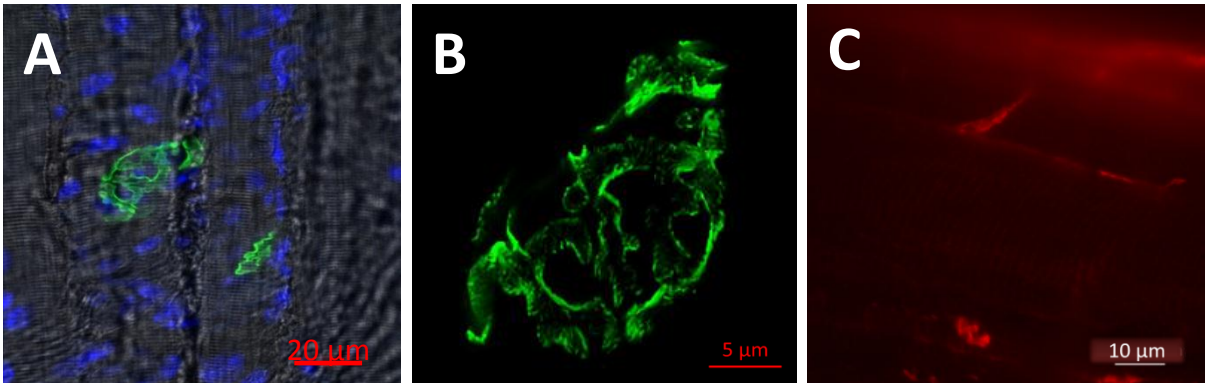

Figure 3.5.6 **Striation patterns on the NMJ. A)** IHC stained intact *plantaris* muscle showing a topography of α-btx stained NMJs (green) along striated myofibres - seen as dark lines with light transmission (Scale bar = 20 µm). **B)** We noted etched out lines on the surface of NMJs that had been imaged with super resolution at 60x magnification (Scale bar = 5 µm). These patterns may be coupled to the striations seen on skeletal muscle tissues, as seen in **C)** 60x magnification super resolution image of laminin (red) showing the striations of the myofibre (Scale bar = 10 µm).

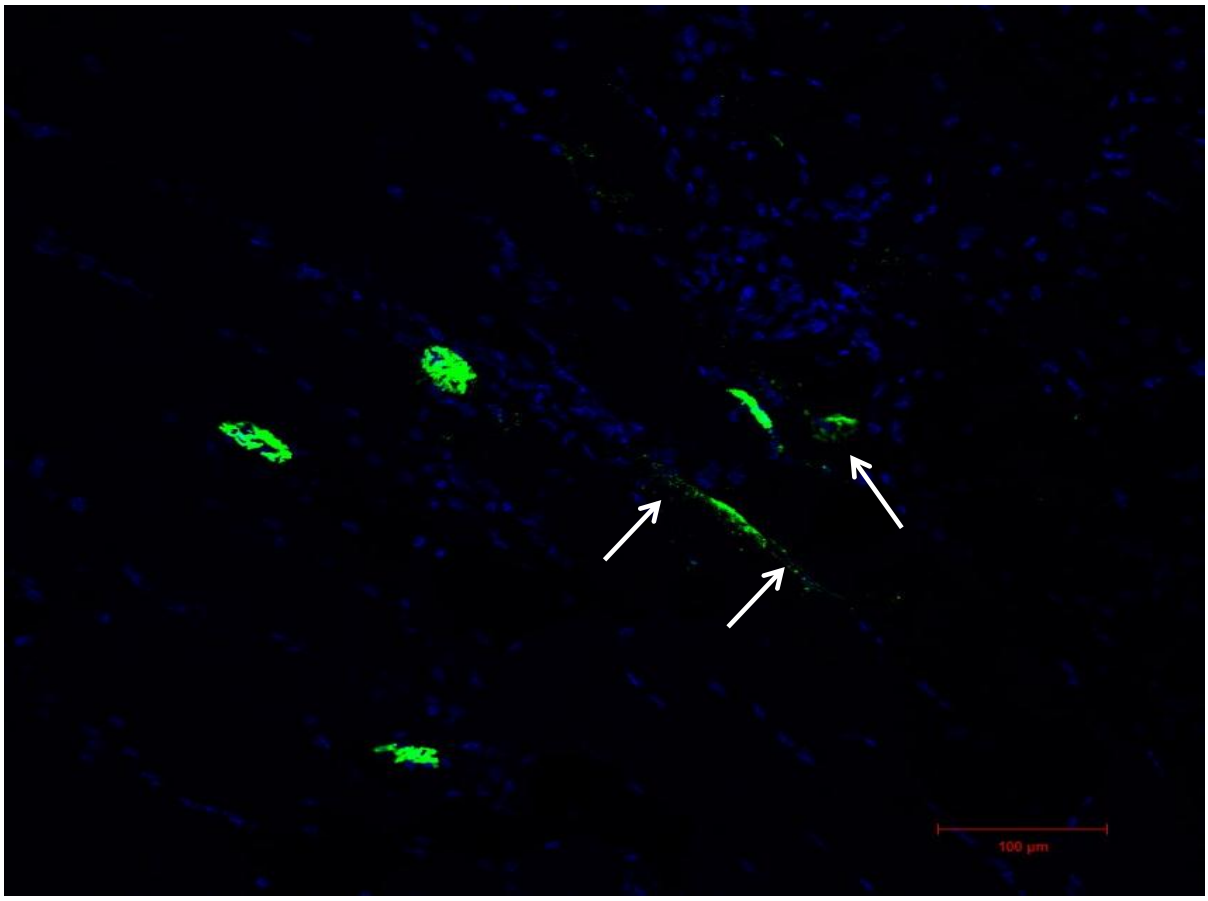

Figure 3.5.7 **Damaged NMJs in injured *gastrocnemius* muscle, 3 days after muscle contusion injury (**20x magnification). α-Btx stained NMJs (green) - appearing more dispersed in sites closer to severely disrupted myofibres with a great influx of nuclei (Hoechst - blue). NMJs suffering extreme damage appear flattened white arrows when viewed in longitudinal section; with AChRs dispersed along the sarcolemma of its respective myofibre (white arrows). Scale bar = 100 µm.

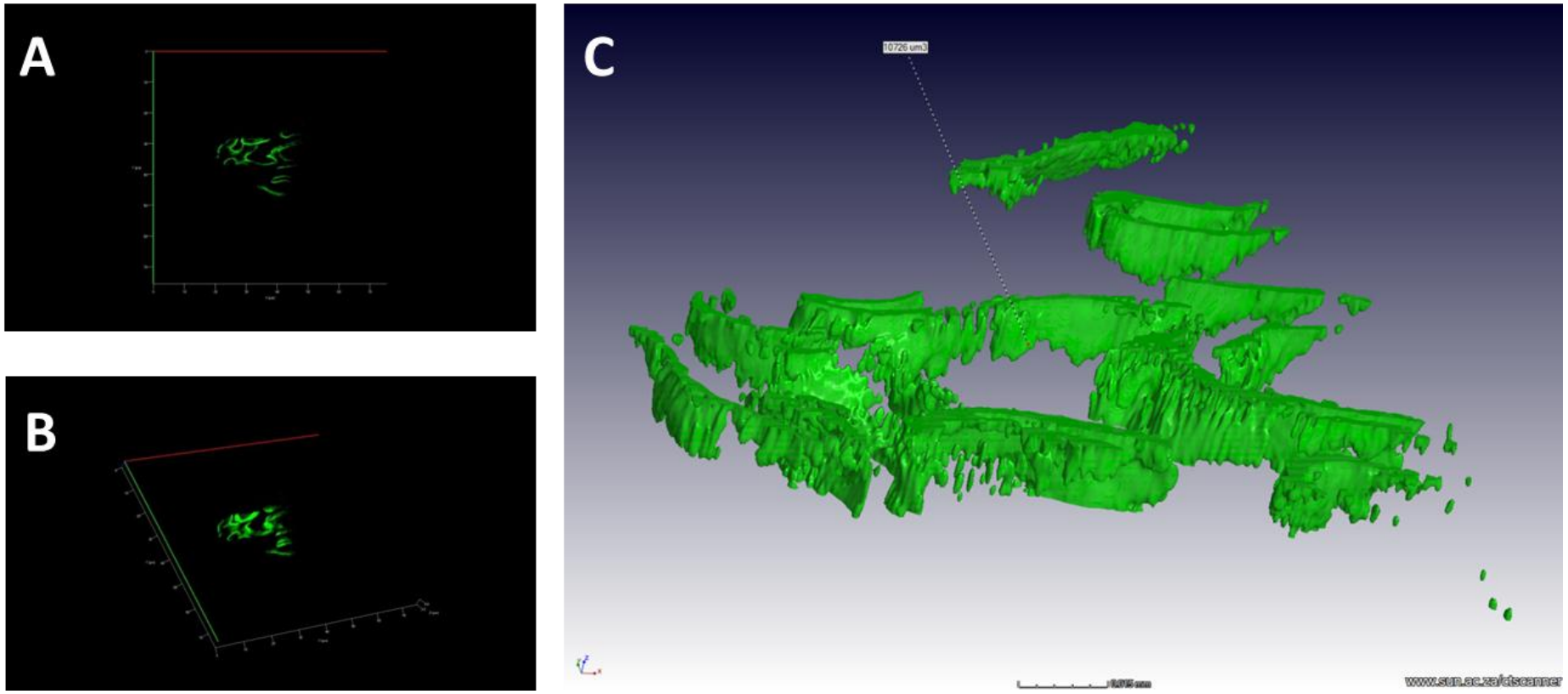

Figure 3.6.1 **Intact NMJ in *en face* view.** Section from intact *plantaris* muscle of mouse, not subjected to contusion injury. **A)** and **B)** 3D super-resolution image of an α-btx stained NMJ at 63x magnification showing the classic coral-like structure typical of the mature NMJ **A)** in XY view and **B)** at an angle to include Z plane view. **C)** 3D render of z-stack images (n = 30) from super-resolution showing surface area and volume measurements. Note: Further organisation can be seen in the 3D render view.

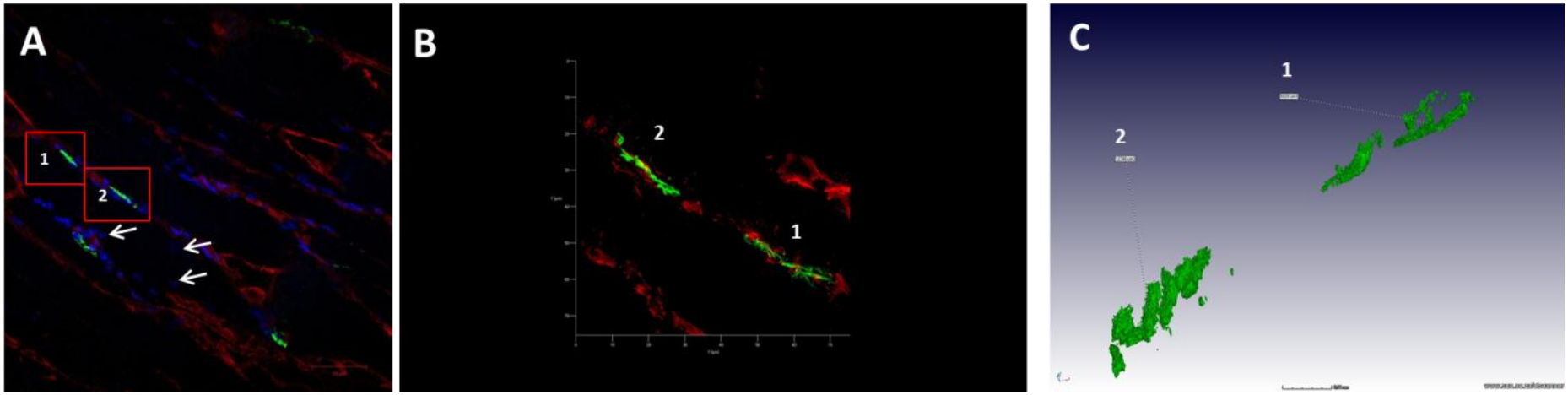

Figure 3.6.2 **Injured NMJs in side-long view, 5 days post injury.** Section from injured *gastrocnemius* **A)** Confocal image at 40x magnification with α-btx stained NMJs (green); anti-laminin for the sarcolemma (red) and Hoechst stained nuclei (blue). Two NMJs (1 and 2, red boxes) are positioned on the side of longitudinally-sectioned myofibres. NMJs appear long and slim with little or no apparent organisation. Increased nuclei within the region as well as centrally located nuclei (white arrows) show recent myofibre regeneration. Scale bar = 50 µm. **B)** 3D super-resolution images of NMJ 1 and 2 at 63x magnification with laminin. Image is inverted view of confocal image. **C)** 3D Render of z-stacks (n = 91) of 3D image in B), showing surface area and volume measurements.

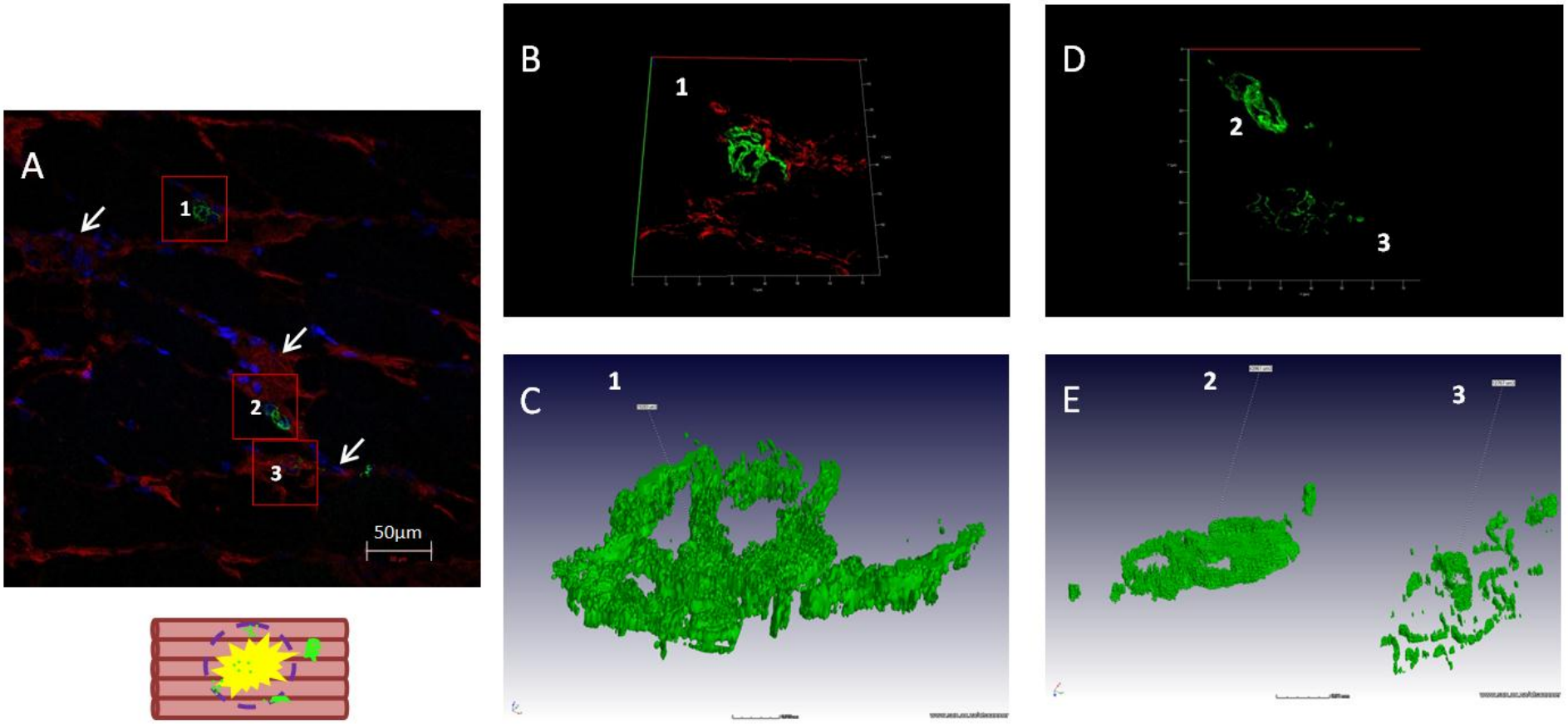

Figure 3.6.3 **Injured NMJs in *en face* view in border zone, 5 days post injury.** Section from injured *gastrocnemius* muscle. **A)** Confocal image at 40x magnification of α-btx stained NMJs (green); anti-laminin for the sarcolemma (red) and Hoechst stained nuclei (blue). Three *en face* NMJs (1, 2 and 3, red boxes) are visible in the border zone of muscle contusion injury. NMJs appear damaged, particularly NMJ 3, closer proximity of the impact zone. Increased nuclei within the region and laminin accumulation (white arrows) indicate myofibre regeneration. Scale bar = 50 µm. **B** and **D)** 3D super-resolution images of **B)** NMJ 1 including laminin and **D)** NMJ 2 and 3, without laminin. NMJ 3 shows fracturing of the structure; however the junctional folds are still evident. Both images taken at 63x magnification. **D** and **E)** 3D render of z-stacks ((D) n = 52; E), n = 57) from 3D images in B) and D) respectively, showing of surface area and volume measurements. The image below A) shows a schematic view of the effect of contusion injury to NMJs in the impact area (yellow) compared to tNMJs in the border zone (within purple circle.)

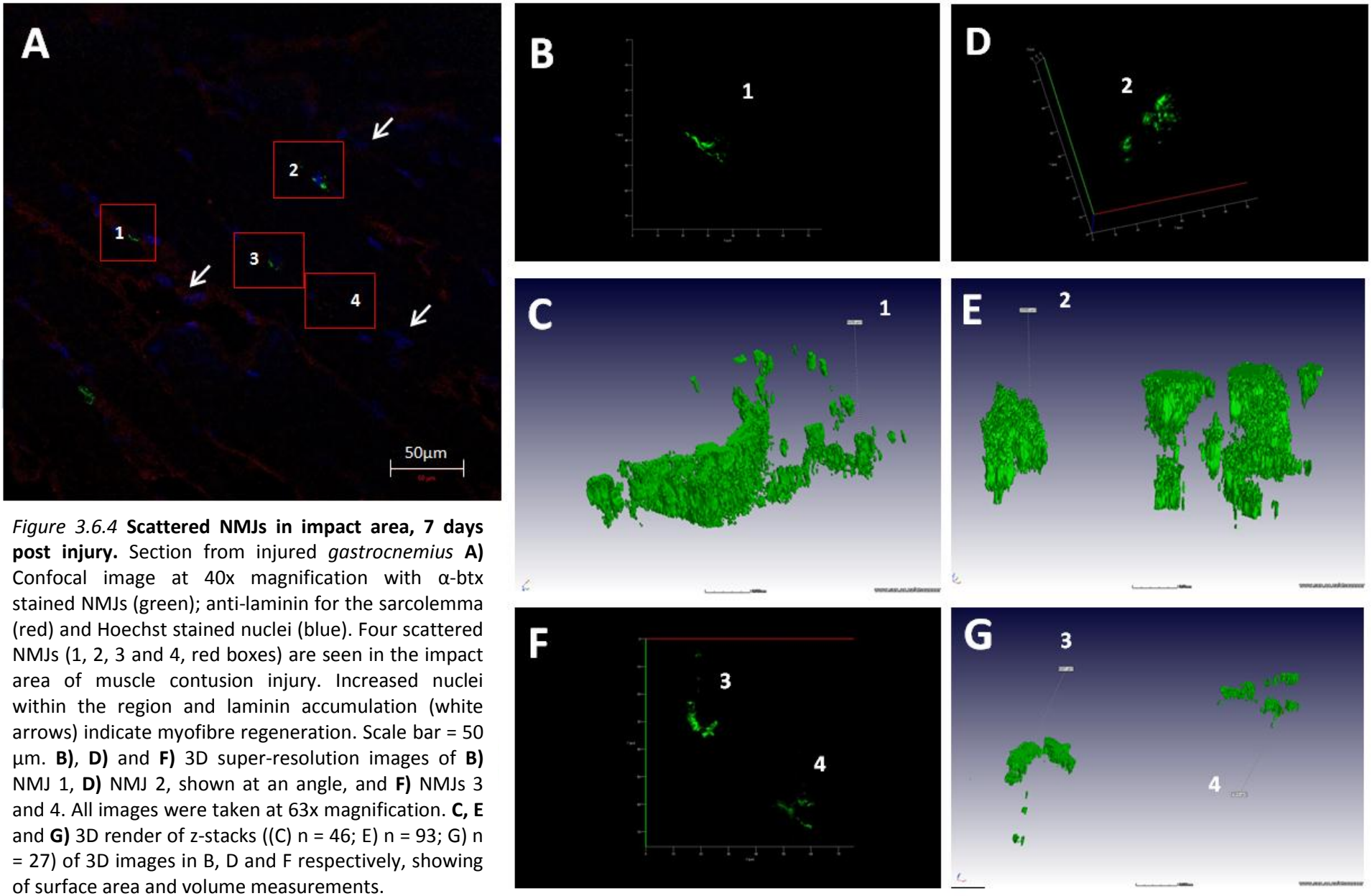

Figure 3.6.4 **Scattered NMJs in impact area, 7 days post injury.** Section from injured *gastrocnemius* **A)** Confocal image at 40x magnification with α-btx stained NMJs (green); anti-laminin for the sarcolemma (red) and Hoechst stained nuclei (blue). Four scattered NMJs (1, 2, 3 and 4, red boxes) are seen in the impact area of muscle contusion injury. Increased nuclei within the region and laminin accumulation (white arrows) indicate myofibre regeneration. Scale bar = 50 µm. **B)**, **D)** and **F)** 3D super-resolution images of **B)** NMJ 1, **D)** NMJ 2, shown at an angle, and **F)** NMJs 3 and 4. All images were taken at 63x magnification. **C, E** and **G)** 3D render of z-stacks ((C) n = 46; E) n = 93; G) n = 27) of 3D images in B, D and F respectively, showing of surface area and volume measurements.

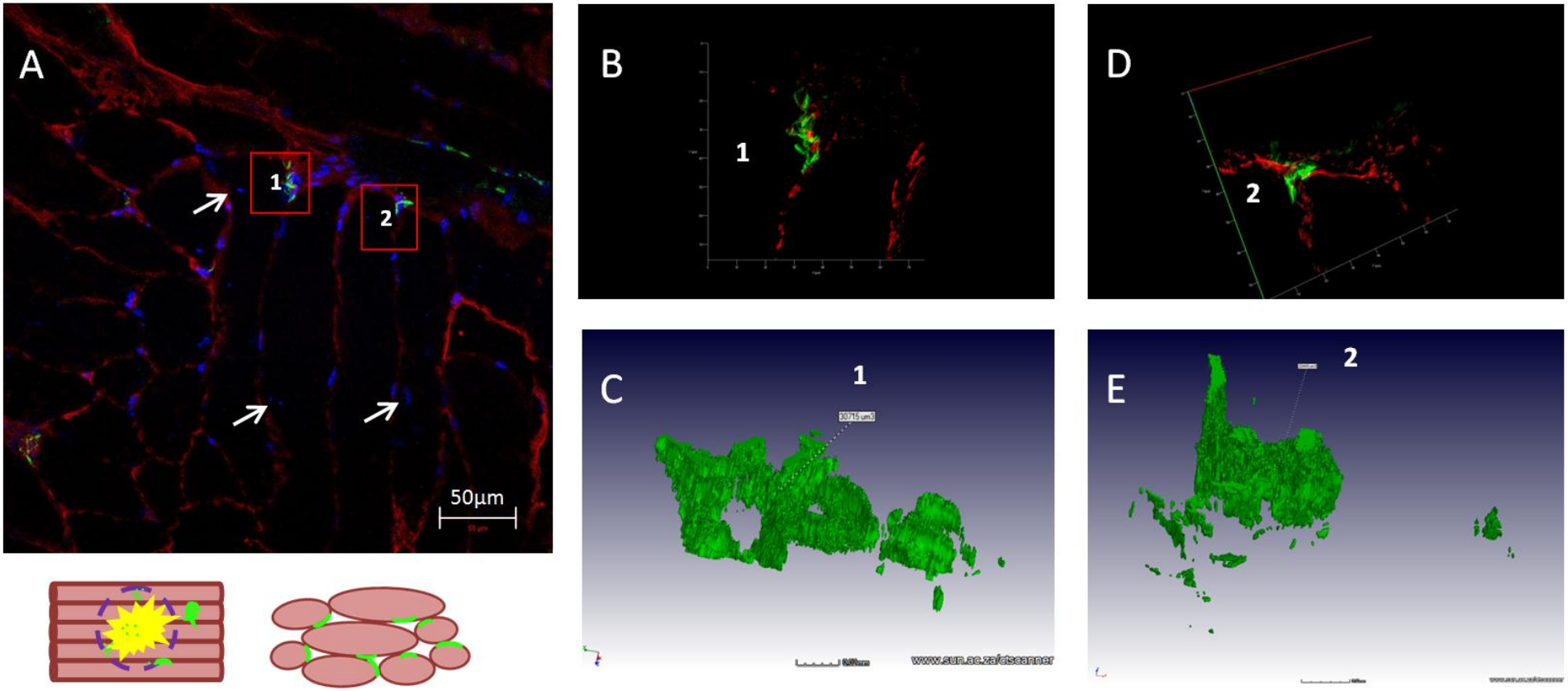

Figure 3.6.5. **Regenerating NMJs in diagonal section, 14 days post injury.** Section from injured *gastrocnemius* **A)** Confocal image at 40x magnification with α-btx stained NMJs (green); anti-laminin for the sarcolemma (red) and Hoechst stained nuclei (blue). Two NMJs (1 and 2, red boxes) are positioned on the side of diagonally-sectioned myofibres. NMJ 2 displays characteristic moulding of NMJ around the curve of the fibre. Laminin accumulation and increased nuclei within the region as well as centrally located nuclei (white arrows) indicate recent myofibre regeneration. **B)** and **D)** 3D super-resolution images of NMJ 1 and 2 respectively , at 63x magnification. Image is inverted view of confocal image. **C** and **E)** 3D render of z-stacks ((C) = 102; E) = 104) of 3D images in B) and D) respectively, showing surface area and volume measurements. Scale bar = 50 µm.

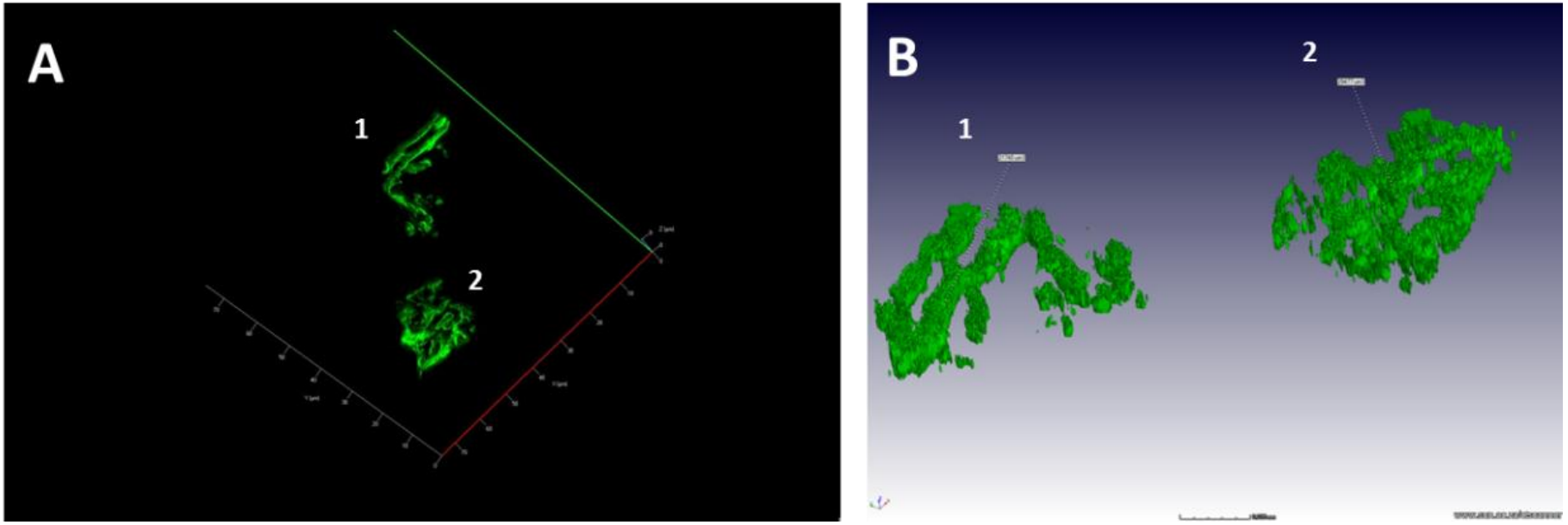

Figure 3.6.6 **Other variations of NMJs in *en face* view, 14 days post injury.** Section from injured *gastrocnemius* muscle. **A)** 3D super-resolution image of α-btx stained NMJs at 63x magnification, 1) showing a denser version of the normal coral-like structure and 2) showing some of the classic complex, but also a few straight, far-extending branches. **B)** 3D Render of z-stacks (n = 89) of 3D image in B), showing surface area and volume measurements. Presence of scattered AChRs indicate NMJ endured some damage from contusion injury.

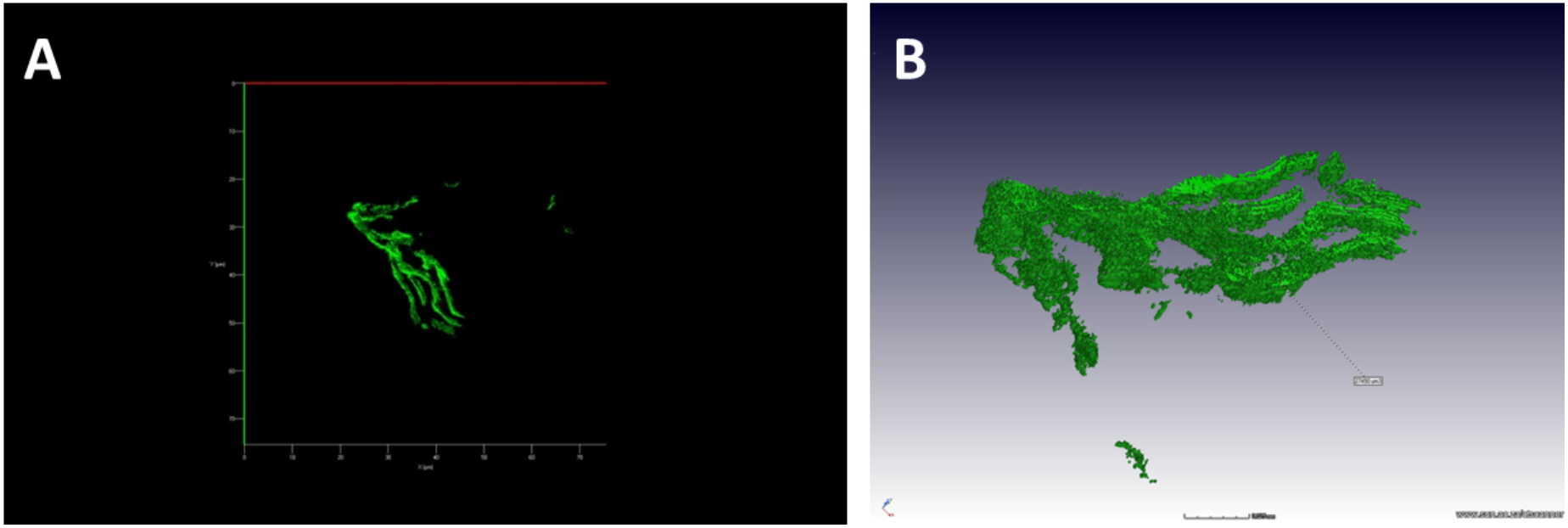

Figure 3.6.7 **Injured NMJ in *en face* view with extended processes, 14 days post injury.** Section from injured *gastrocnemius* muscle. **A)** 3D super-resolution image of α-btx stained NMJ at 63x magnification, showing little of the normal coral-like structure, but rather has straight, far-extending branches. **B)** 3D render of z-stack images (n = 53) from A), showing surface area and volume measurements. Presence of scattered AChRs indicate NMJ endured some damage from contusion injury.

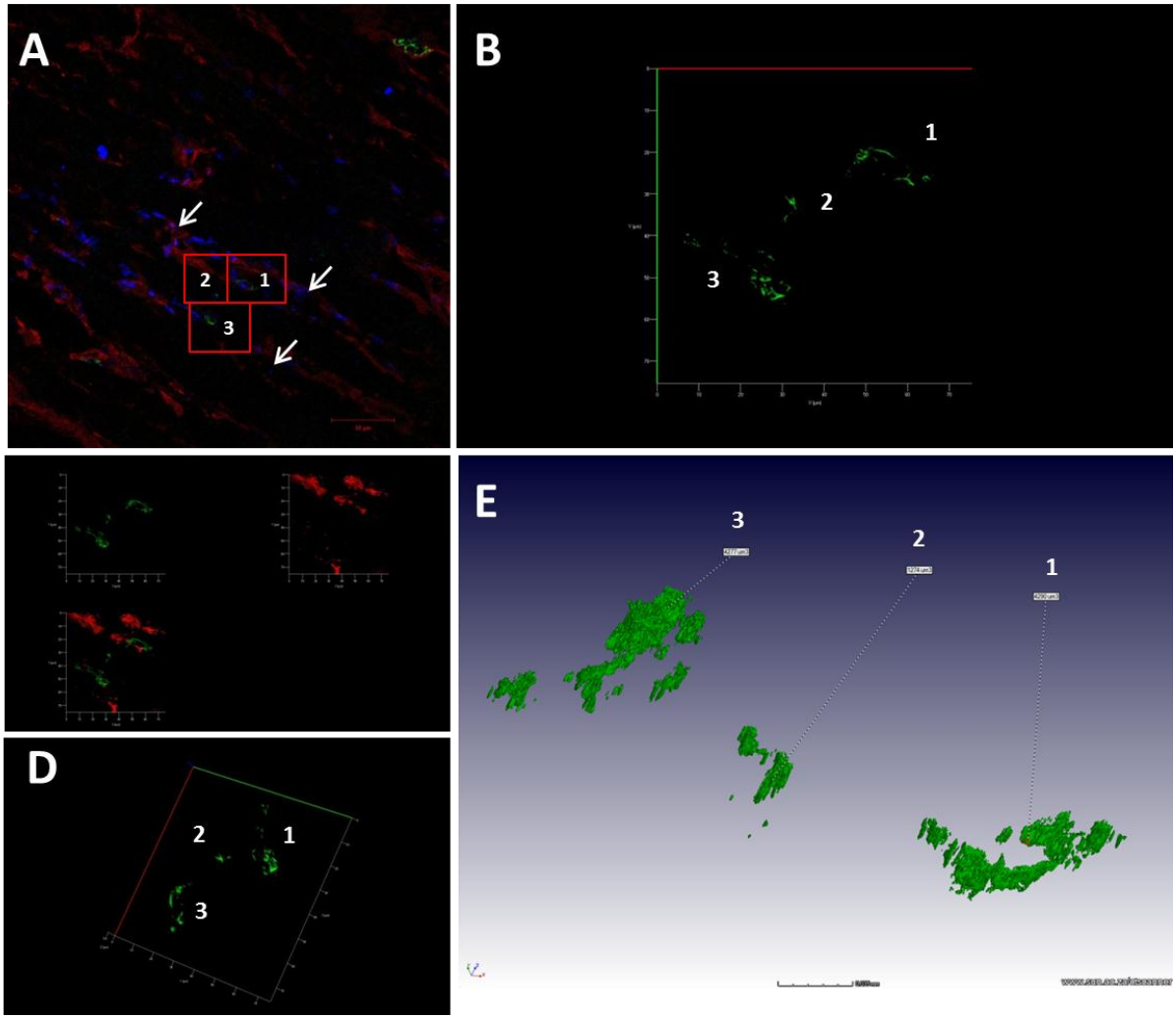

Figure 3.6.8 **Tips of regenerating NMJs as section cuts only the superficial layer of sarcolemma, 14 days post-injury.** Section from injured *gastrocnemius* muscle of **A)** Confocal image at 40x magnification of α-btx stained NMJs (green); anti-laminin for the sarcolemma (red) and Hoechst stained nuclei (blue). The superior tips of three NMJs (1, 2, and 3, red boxes), are found in close proximity to one another on longitudinally-sectioned myofibres. Laminin deposits; increased nuclei within the region; as well as centrally located nuclei (white arrows) indicate recent myofibre regeneration. NMJs themselves are faint and show no organisation at 40x view. Scale bar = 50 µm. **B)** 3D super resolution image of NMJs of interest. Increased magnification shows narrow surfaces, many of which are not linked. **C)** 3D super-resolution image showing NMJs and laminin separately and merged. **D)** 3D super-resolution image showing image at an angle for better spatial perception of the slim structures. All super-resolution images were taken with 63x magnification. **E)** 3D render of z-stacks (n = 51) of 3D image in B), showing surface area and volume measurements. Image is inverted view of super resolution image.

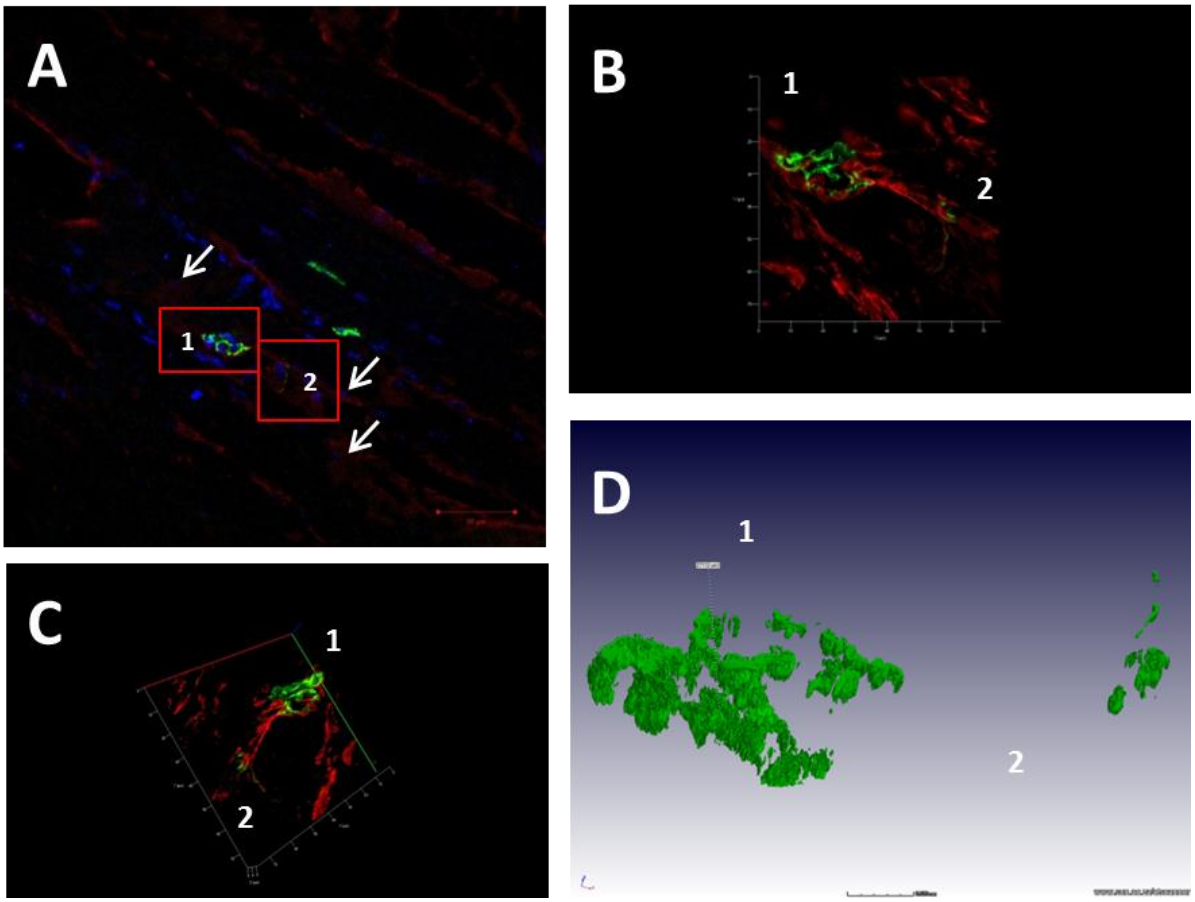

Figure 3.6.9 **Regenerating NMJ in *en face view,* 14 days post injury. A)** Confocal image at 40x magnification with α-btx stained NMJs (green); anti-laminin for the sarcolemma (red) and Hoechst stained nuclei (blue). Image shows two NMJs (1 and 2, red boxes) spread over the top of regenerating, longitudinally sectioned myofibres. NMJ 1 shows regeneration, with clearly visible sub-synaptic myonuclei and 2) a thin strip of damaged AChRs reaching across the myofibre. Laminin accumulation; a multitude of nuclei and central nuclei (white arrows) indicate this was the impact area of the contusion injury. Scale bar = 50 µm. **B)** 3D super-resolution images of NMJ 1 and 2, taken at 63x magnification and **C)** shown at an angle for better spatial perception. **D)** 3D render of z-stacks (n = 83) of 3D image in B), showing surface area and volume measurements.

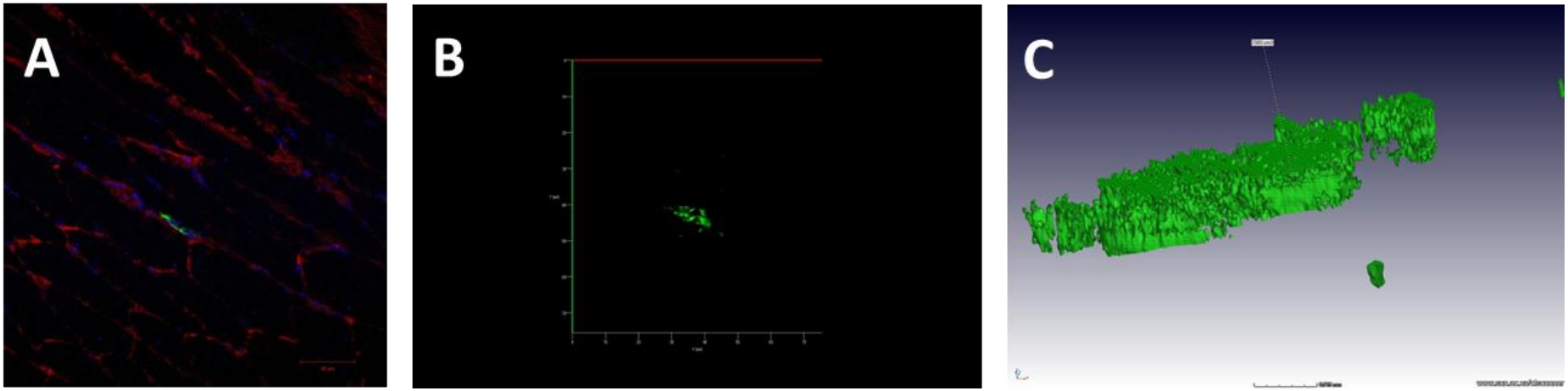

Figure 3.6.10 **NMJs wrapping around longitudinally sectioned myofibre in regenerating muscle section from border zone, 14 days post injury.** Section from injured *gastrocnemius* **A)** Confocal image at 40x magnification with α-btx stained NMJ (green); anti-laminin for the sarcolemma (red) and Hoechst stained nuclei (blue). NMJ has sidelong appearance on the edge of the myofibre, but also has extensions wrapping around the curve of the cylindrical myofibre. Laminin build-up and increased nuclei within the region indicate some myofibre regeneration. Scale bar = 50 µm. **B)** 3D super-resolution image of NMJ at 63x magnification. White arrow indicates portion of AChRs of the distal edge of the curved extensions coming back into view, although continuity of the structure was not captured in this image. **C)** 3D render of z-stacks images (n = 28) from B), showing surface area and volume measurements. Curved processes were not evident in the 3D images.

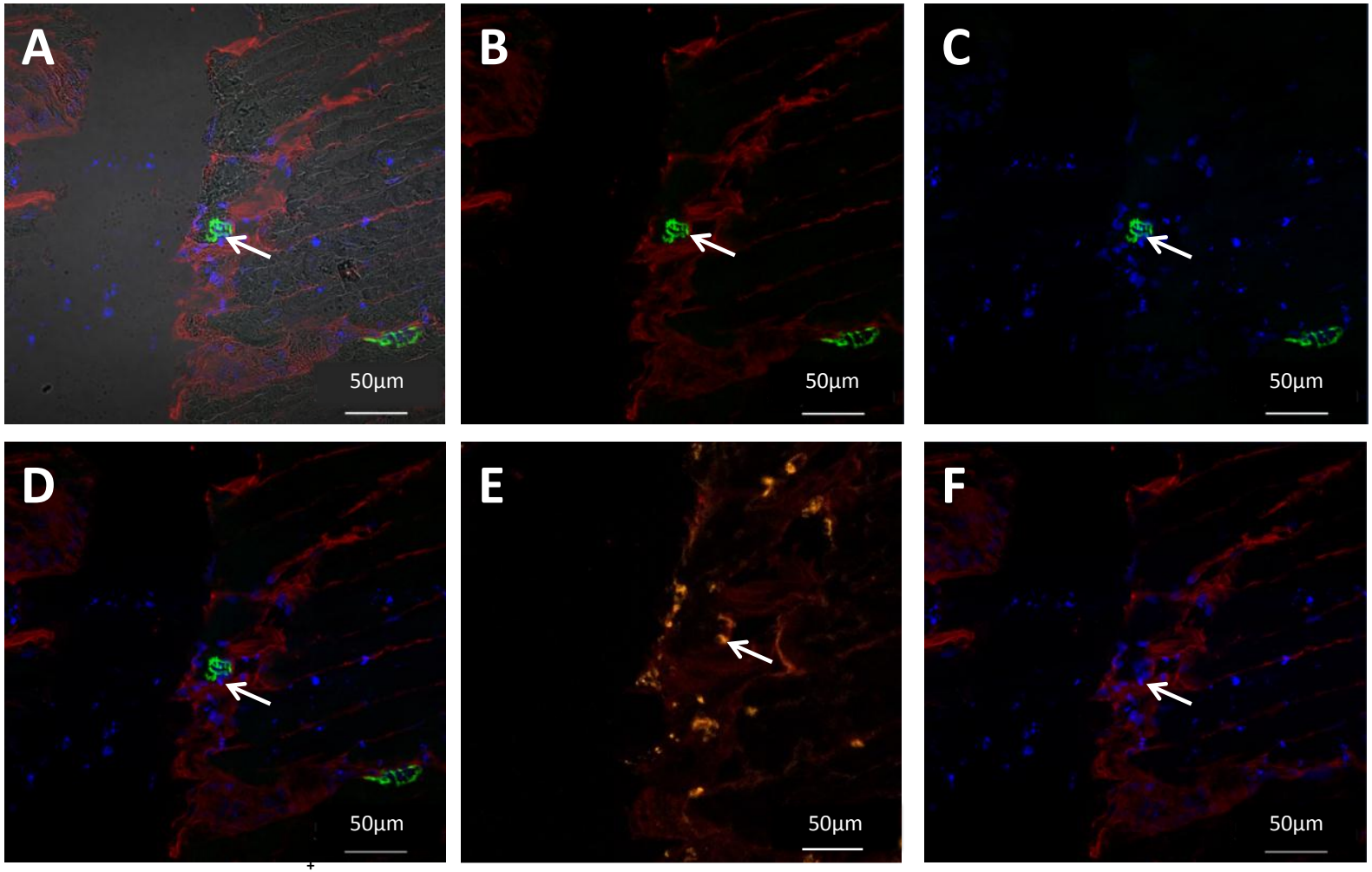

Figure 3.8.1 **Visualising BrdU$^+$ subsynaptic nuclei.** 40x magnification of non-injured *gastrocnemius*, 14 days post injury. Section stained with α-btx for NMJs (green), anti-laminin for muscle membrane (red), Hoechst for nuclei (blue): **A)** with light microscopy; **B)** anti-laminin (red) and α-btx (green); **C)** α-btx and anti-laminin; **D)** α-btx, anti-laminin and Hoechst; **E)** laminin and anti-BrdU (orange) (second round of staining) and **F)** anti-laminin and Hoechst. Scale bar = 50 µm.

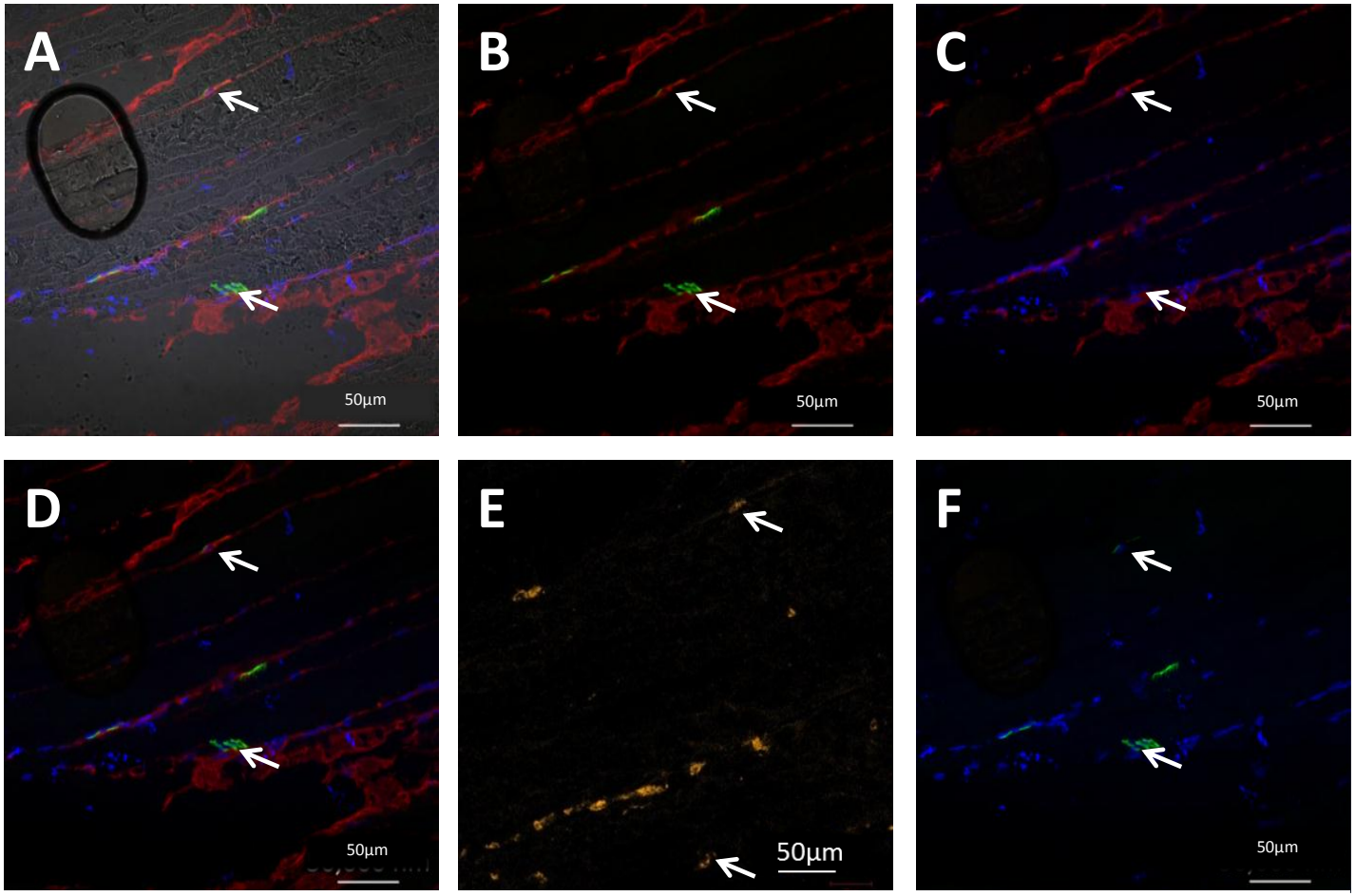

Figure 3.8.2 **Visualising BrdU^{+} subsynaptic satellite cell.** 40x magnification of non-injured *gastrocnemius*, 14 days post injury. Top arrow indicates a subsynaptic BrdU^{+} nucleus enclosed in a pocket of laminin – a satellite cell. **A)** includes light microscopy; **B)** anti-laminin (red) and α-btx (green); **C)** α-btx and anti-laminin; **D)** α-btx, anti-laminin and Hoechst; **E)** anti-BrdU (orange) (second round of staining) and **F)** anti-laminin and Hoechst. Note:. Arrows mark the correlating areas for the slightly magnified BrdU stained image in **E)**. Scale bar = 50 µm.

Chapter 4 Discussion

4.1 Introduction

To our knowledge, this is the first study to investigate the effect of a muscle contusion injury on the morphology of the NMJ. This is important because the reality of peripheral nerve injury includes causes other than complete severance of nerve supply and related neurally released factors. The data will be discussed within the context of other studies, but it should be noted that similar findings may not necessarily be expected.

This focus is supported by qPCR analysis of the effect of a muscle contusion injury on the AChR γ- and ε-subunit expression. Furthermore, this study touches on visualising SCs located beneath the NMJ by means of confocal microscopy.

4.2 Mouse mass

Mice were all above 20 g and past the rapid growth phase. Therefore, maturation would not have influenced any results in the study. Weight increased steadily, but duration of 28 days post injury was required for the growth to be significant.

The added weight of the mini-osmotic pump increased the mass at sacrifice of all mice in the BrdU group by ~ 1.1 g. This contributed towards bigger differences between the mass at injury and mass at sacrifice and for these differences to be significant at additional time points of day 3, 7, 10 and 14. No decrease in mass resulting from stress of the pump implantation was perceived.

4.3 AChR-ε mRNA expression

AChR-ε subunit expression was low in both legs in the groups sacrificed earlier (days 1, 3 and 5) in comparison with the later groups (days 7, 10 and 14). This is in agreement with Jianjun *et al.* (2005) who noted a peak in ε-subunits at 7 days post injury in *gastrocnemius* muscle denervated by an intramuscular injection of BoTX[30]. However, while Jianjun *et al.* (2005) found the ε-subunit mRNA levels returned to normal by 15 days post injury[30], our results indicated only a small decrease at day 10 and not anywhere close to the extent of being back to normal. At day 14 post injury AChR-ε subunit mRNA remained high.

The differences for the slower recovery of ε-subunit mRNA in our study can be due to the nature of the injury sustained by the muscle. While Jianjun *et al.* focused on solely denervating the muscle[30]

(BoTx denervates the muscle by inhibiting the release of ACh from the motor neuron[31], a muscle contusion injury affects both the nerve, NMJ and the muscle fibre. Hence the damage sustained by the postsynaptic apparatus and the muscle fibre are sure to contribute to the regeneration time course over and above the lack of neurotransmitter and neural stimuli.

The increase seen in later time points in the non-injured *gastrocnemius* could be due to factors released from the injured limb causing a systemic change sufficient to stimulate AChR-ε subunit mRNA synthesis. Jianjun *et al.* found that ε-subunit mRNA levels in the non-injured muscle of the contralateral leg followed the same pattern of the injured muscle[30]; hence this is not a novel finding. The systemic change in response to injury could have included an increase in inflammatory molecules and growth factors that could cause upregulation of AChR subunits (in this case the ε-subunit, but possibly all AChR subunits). Typically muscle injury first follows a path of degeneration before inflammation[3] hence immune cell released factors appear later.

In order to determine whether this is a systemic effect, a group of mice that are not subjected to any injury in either leg is necessary as a completely negative control. Additionally, it would be interesting to compare the AChR subunit expression between the popular method of NMJ damage (nerve transection) and this muscle contusion injury model. This can be done by adding one or more groups of mice that have undergone a nerve transection of their sciatic nerve and sacrificed at the same time point/s as used here.

One technical possibility for the difference in both legs between the earlier and later time points exists: the samples were run on two different plates for qPCR experiments due to the large sample size - days 1, 3 and 5 on the first plate and days 7, 10 and 14 on the second plate. Great consideration for this arrangement was given prior to the experiments and, as per procedure, a reference sample (in duplicate as per the experiment samples) was added to each plate and CT readings were taken during the experiment. The difference of the readings between reference samples on each plate was applied to the calculations in order to eradicate any discrepancies between the two plates.

As we used the largest of the qPCR plates (96 well plate) it is not possible to include all samples on one plate. Another arrangement of samples that could be used is adding half the duplicated samples of each group to one plate (n = 3) and the other half to the other plate. However, the chance that this difference was due to a variation between the two plates is highly unlikely as reference samples were used and samples treated exactly the same and within 2 hours of one another on the same day in the same conditions.

4.4 Muscle selection and sectioning

This study employed an injury model familiar to our research group. Our research group has also used the BALB/C mouse; the *gastrocnemius* muscle and the cryopreserving technique in previous studies on muscle contusion injury. Longitudinal sectioning is, however, an unexplored technique for our research group and this technique was refined in our study in terms of the precise location of injury as well as the location and arrangement of the NMJs – also a region of interest previously uncharted by our research group.

4.4.1 Longitudinal Sectioning

Four factors determine the successful sectioning of a longitudinally orientated muscle sample. Firstly, one must identify the orientation of the first sections and be able to adjust the orientation of the muscle should fibres appear diagonal- or cross sectioned (see Figure 3.3.1.1). For a large muscles like the *gastrocnemius*, it difficult to section purely longitudinally orientated fibres. Due to its enlarged shape, the muscle bulges and hence a single section can include fibres in all three orientations. Efforts were made to obtain the largest possible area of longitudinally oriented fibres in each case (See Figures 3.3.1.1, 3.3.1.2 and 3.5.3).

The second factor is to discern between the various causes of damage to the tissue. We found freezer damage that produced multiple areas of artefact visible as large unstained areas of water. Freezer damage was seen in the practise mice samples and resulted from the suboptimal temperature of the isopentane. When the isopentane was cooled to freezing point, the integrity of the muscle samples improved.

Damage from possible thawing and refreezing causes the myofibres to lose their structure and normally elongated fibres are seen as fragmented and lacking sarcolemma organisation. H&E staining reveals no increase in nuclei; therefore no immune response has occurred as is the case in true injured myofibres.

Damage resulting from the cryo-sectioning blade shows portions of fibres split and crinkled up at the ends. This is similar to the phenomenon of the sealing off of the fibre seen in regenerating muscle, but H&E staining reveals no accumulation of myonuclei in the areas of artefact.

True damage resulting from the muscle contusion injury is identified by i) swelling of the myofibre as oedema (fluid accumulation) sets in with necrotic fibres; ii) disrupted fibres; iii) large numbers of infiltrating immune cells and proliferated SCs (seen as purple stained nuclei in H&E staining); iv) scar tissue formation (parenthesis); v) sealing off of torn myofibres; vi) fibrosis and vii) SC activity for the

repair of damaged fibres and the construction of new fibres (seen in regenerating muscle) (see Figure 3.3.2 .1–3.3.2.3).

Finally, one must consider the ideal thickness of sections for visualising both NMJ and SCs. SC studies show best results when muscle is sectioned at ~5 - 10 µm[3,84], while NMJ studies used thickness of up to 50 µm[84,94]. In our study, NMJs in initial assessments were better captured in thicker sections of 15 – 20 µm (see Figures 3.5.2, 3.5.5, 3.5.6). Later work proved a thickness of 10 µm to be sufficient for both NMJ and SC visualisation (see Figures 3.8.1 and 3.8.2).

4.4.2 Selection of muscle

The *gastrocnemius* is the largest muscle in the calf muscle complex and lies superficially to its synergists. This makes it the best candidate for muscle contusion injury by our specialised apparatus. The *gastrocnemius* is densely innervated along its deep surface by the tibial branch of the sciatic nerve[27]and thus motor endplates may overlap.

To fully understand location and arrangement of NMJ bands along *gastrocnemius* muscle in longitudinal orientation, it is beneficial to take serial sections of muscle as well as various orientations of different samples and view on a basic fluorescent microscope. This practise will enable accurate targeting of the location of the NMJs. Alternatively, use a smaller muscle, i.e. the *plantaris, soleus* or *tibialis anterior*. These muscles have a smaller fibre area which allows for easier, more intact section with more chance of obtaining solely longitudinally orientated myofibres. However, our contusion injury model is designed to specifically injure the gastrocnemius muscle. The proposed muscles lie beneath the gastrocnemius and are therefore not directly impacted. Hence, development of a new technique is necessary in order to assess injury of another muscle.

The *soleus* is innervated by the tibial nerve in the same fashion as the *gastrocnemius*. The long, thin *tibialis anterior* muscle is innervated by the deep peroneal branch of the sciatic nerve and has proved to be a useful muscle to study NMJ morphology[27]. Intact *plantaris* produced a better quality image for method development.

4.5 Tracing the uptake of BrdU into the regenerating muscle tissue and its proximity to the NMJ

4.5.1 BrdU$^+$ cells increase according to the time lapsed after injury

As expected, the prevalence of BrdU$^+$ cells within the muscle and adjacent blood vessels increased with the number of days post injury. At day 3 and 5, only a small portion of BrdU$^+$ cells were visible

in the bloodstream and very few $BrdU^+$ were detected along the muscle. In these samples there had been less time for blood cells and satellite cells to proliferate in comparison to samples takes at 7 and 14 days post injury. In the latter, $BrdU^+$ cells occupied the larger proportion in the blood stream and were readily detected in the myofibres, particularly around the sites of injury. This is a good representation of the amount of repair work occurring at the sites of myofibre injury.

$BrdU^+$ cells were also noted in the non-injured samples at day 14 post injury, in similar large proportions in the blood stream as the injured muscle as the turnover rate blood cells is high and thus cells are constantly dividing and proliferating. In the non-injured myofibres, $BrdU^+$ cells were noted in uniform arrangement along the myofibres (see Figure 2.9), indicative of the continual maintenance role of the satellite cell in normal muscle tissue. This is in contrast to the clusters of $BrdU^+$ cells found in injured muscle samples at the same time point post injury (see Figure 2.10, where satellite cells have focused on a particular site on the myofibre.

4.5.2 Using tile scans as a technique to plot NMJ arrangement and determining the location of $BrdU^+$ cells in proximity to the motor end-plate

Challenges lay in imaging BrdU with α-btx (see Pilot study 3), as well as in locating the innervation pattern of the NMJs along the larger gastrocnemius muscle. A method of creating tile scans of the entire surface of the section enabled one to relocate NMJs for further imaging and to determine NMJ sites to analyse for co-localisation of BrdU+ nuclei. This method allows one to analyse sections of larger muscle groups (e.g. the *gastrocnemius*) as a whole which is especially useful in studies done on longitudinally sectioned.

4.6 NMJ morphology

Little research has been published on the actual morphological changes of the NMJ following an injury (of any nature) and subsequent regeneration.

Pratt *et* al. 2013 used an injury model consisting of a series of lengthening contractions to compare the morphology of an uninjured wild type NMJ to a) an injured wild-type NMJ; b) an uninjured NMJ from a dystrophic mouse (mdx NMJ) and c) an injured mdx NMJ[26]. This study made use of α-btx staining of AChRs to portray the NMJ and images show injured NMJs at 24 hours post-injury. No noticeable difference was seen in the injured wild type mouse, but the organization of the mdx NMJ severely lacked junctional folds or any sort of organization. 24 hours after muscle lengthening, the AChRs of the mdx NMJs aggregated into multiple, unconnected islands[26].

4.6.1 Intact NMJ

The *en face* view of the intact NMJ demonstrates the classic coral-like arrangement that NMJs are renowned for (see Figure 3.6.1). The super resolution images show that this particular section of the NMJ does not contain some of the connecting junctional folds. A 3D render of this sample shows smooth edges (in Z plane) and continuity of AChRs on the visible folds of this NMJ. The smooth edges demonstrate the mature organization of the AChRs on an intact adult NMJ.

In comparison, all the NMJs on the injured samples showed a granular appearance along the Z plane (see Figures 3.6.2 – 3.6.10). These NMJs are referred to as the injured and regenerating NMJs. The majority of these injured and regenerating NMJs show discontinuous and scattered AChRs to various extents. It can be concluded that the crush injury had a completely different localised damage than induced by a stretch-induced injury. In terms of application, both the models have value.

4.6.2 Day 5 post injury NMJs

The sidelong NMJs from the day 5 sample, view A, in Figure 3.6.2, show AChRs arranged in a long thin line as NMJs are presented by only one of their folds bordering the sarcolemmal periphery of the myofibre. NMJ 1 displays a more scattered version of a Sidelong NMJ than NMJ 2. Increased magnification shows beginnings of the superficial NMJ folds (NMJ 2) while the wispy, slightly dispersed appearance of (NMJ 1) suggests more damage was incurred to this structure.

We can presume that NMJ 1 was situated closer to the impact zone and therefore more affected by the contusion than NMJ 2. However, both NMJs have maintained their basic level of organization implying that this muscle section lay in the border zone of the injury area.

On the same day 5 sample, in Figure 3.6.3, 3 examples of NMJs could be seen in the *en face* view, also on border zone of Injury. NMJ 1 is located above NMJ 2 and 3 in the confocal image (Panel A). NMJ 1's structure seems robust, but its organization appears as a combination of junctional folds and slightly extended processes (Panel B and C). This peculiar organization could be a product of a mildly damaged/recovering NMJ. NMJ 1 displays a staggered Z plane surface, characteristic of the injured NMJs, but no noticeable scattered AChRs.

NMJ 2 has maintained a highly complex level of organization although scattered AChR clusters appear on either side of the structure (Panel D and E). NMJ 3 has the most fractioned appearance implying that damage was severe, although it has maintained perceptible organization of junctional folding (Panel D and E). All three NMJs show damage seen by the jagged appearance of the Z axis (compare to uninjured sample), especially NMJ 3 with its remarkable fragmentation of the structural

complex. From this it can be deduced that NMJ 3 lay in closer proximity to the impact zone, although not directly in the impact zone as this would have caused more severe scattering of the AChRs (as seen in day 7 NMJs) that would not have recovered enough to show any organization within this short period of time. Interpretation of images with only some organisation is difficult because it isn't clear if they are damaged to that particular extent, or if regeneration is progressing. This issue is partly answered by observations that day 7 NMJs were actually morphologically more severely disrupted, suggesting that the process of degradation is still present at 7 days.

4.6.3 Day 7 post injury NMJs

Severe fragmentation is seen in all NMJs analysed on the day 7 post injury sample (see Figure 3.6.4). The confocal image (Panel A) shows NMJs as faint bodies made up of small collections of AChRs that show no organization to resemble a characteristic motor end-plate. 3D super resolution images (Panel B, D, and F) and 3D renders (Panel C, E and G) emphasize the fragmentation of the injured NMJs. NMJ 2 displays the separation of entire sections of AChRs from the original motor end plate (Panel D and E). In NMJ 4, the smallest structure, most AChRs have degenerated completely (Panel F and G).

The fragmented appearance and diminished amount of AChRs indicate that these NMJs were in the area that received direct impact from contusion injury and are still in the degenerated stage.

4.6.4 Day 14 post injury NMJs

In Figure 3.6.7, the *en face* NMJ 1 appears to be regrouping its fragments that were separated by contusion injury. It is likely that the slight strip of AChRs referred to as NMJ 2 could be fragments separated from the main NMJ 1 upon injury, but not completely destroyed.

Figure 3.6.8 shows the tips of NMJ structures in close proximity to one another, alluding to an injured *en face* NMJ that has been scattered and additionally, sectioned to contain only the superficial tips of the end-plate.

Figure 3.6.5 shows NMJs positioned in diagonally sectioned muscle. NMJ 1 has a vaguely *en face* structure although it has short, spiky processes that extend instead of making junctional folds. The confocal image in Panel A shows an influx of nuclei in the region of NMJ 1 and Panel B shows fragmented laminin alluding to a damage to the sarcolemma of the myofibre – confirming that this area was subjected to serious contusion injury. NMJ 2 represents a true diagonally sectioned NMJ as one clearly observes the sharp curving around the periphery of the myofibre in Panel A and D. The 3D super resolution image in Panel D also shows scattered laminin, indicating injury while the 3D

render in Panel E shows scattered AChR deposits – albeit more voluminous in the 3D render - confirming the occurrence of an injury to this particular area. The unorganised condition of NMJ 1 and dispersed NMJs surrounding the area of interest show that this site was the point of impact from the contusion injury.

Figure 3.6.10, contains a NMJ wrapping around the myofibre. While the confocal image in Panel A shows the NMJ's processes/folds curving around the cylinder form of the myofibre, 3D super resolution microscopy (Panel B) and the 3D render (Panel C) failed to portray these curved processes for closer observation of their structure. A reason for this could be that when taking the 3D image, the Z planes containing the curving processes were excluded from the portion of the section imaged (insufficient Z-stacks) or that these processes were simply not picked up on the super resolution microscopy at the later imaging stages.

The *en face* NMJs in Figures 3.6.6 and 3.6.7 demonstrate the morphology of NMJs that are in the process of regeneration. Figure 3.6.6 shows robust NMJs with evident junctional folding (Panel A) and structural depth (Panel B) – indicating large numbers of AChRs.

Figure 3.6.7 shows an NMJ with extended processes. This arrangement was not identified in samples of intact muscle, leading to the conclusion that this morphology is part of the later response to injury - either the NMJ arrangement of folds in this extended manner is part of a premature regenerating NMJ or NMJ morphology may have an adaptive response. These possibilities create scope for further study involving analysis of numerous NMJs from both injured and uninjured samples to determine the occurrence of the arrangement of extended junctional processes.

4.7 NMJ Surface Area and Volume Measurements using super-resolution imaging

Morphological assessments discussed above are open to interpretation and hence provide only a qualitative collection of different typical arrangements. Advances is microscopy software, however, enable researchers to start quantifying NMJ sizes and shapes. The process of data collection in this section of the study was an exploratory venture to harness the power these novel analytical tools for quantitative investigation of the NMJ.

Surface area was measured using the area of each individual NMJ from the super-resolution images on Image J software. The Z-stacks of the entire imaged NMJ were combined and underwent structured illumination to create a clear, single image for measurements.

The VGStudioMax 2.2 software combined the number of TIFF files (e.g. 30 z-stacks = 30 TIFF files) to render a 3D reconstruction of the individual NMJs. The volume of these 3D renders was then measured by the same programme.

A total of 20 NMJs from 4 *gastrocnemius* samples (1 intact sample and 3 injured samples at 5, 7 and 14 days post-injury) were analysed for this section. All measurements discussed here are according to Table 3.1. Bar graphs comparing measurements across the time points are seen in Figures 3.9.1 (surface area) and 3.9.2 (volume).

4.7.1 Intact NMJ

The intact NMJ (n = 1 assessed; Z-stacks: n = 30) had a surface area of 96.4 μm^2; a volume of 10 726 μm^3; a density of 357 μm^3/Z-stack. These acted as a bench mark for the values of the injured NMJs.

4.7.2 Day 5 post injury NMJs

In the Side view NMJs from Figure 3.7.2, NMJ 2's volume is more than double that of NMJ 1 (12748 μm^3 > 5825 μm^3). This shows that NMJ 2 has maintained its deeper AChR layers, remaining more secure, intact and in place compared to those of NMJ 1.

In contrast, the *en face* NMJ 3 from Figure 3.7.3 shows discernible organisation, but lacks continuity and depth. Diminished surface area and volume measurements confirm that this NMJ has been subjected to a more severe injury in comparison to NMJ 1 and 2 on the same image. This indicates that NMJ 3 was closer to the site of impact, although not exactly at the site of impact as - in comparison to the scattered NMJs seen at 7 days post-injury – some level of organisation and presence of AChRs is still evident.

The amplified value of *en face* NMJ 2 (see Figure 3.7.3 and Table 3.1) hints at an exaggerated increase in AChR production as seen in the later stages of the PCR analysis of the AChR-ε subunit (see Figure 3.2.2). Although the PCR results only show a significant increase in AChR-ε subunit production by day 7, one must take into account that the PCR samples comprised of multiple sections including many NMJs and there may well be a number of NMJs that have already increased their AChR supply. Additionally, as this NMJ is found in the border zone, it may have experienced a prematurely accelerated AChR accumulation. The large value of NMJ 2 can be explained by these NMJs being present in their section in near entirety, while the other NMJs are only captured in part in the section analysed.

4.7.3 Day 7 post injury NMJs

The Scattered NMJs' surface areas (ranging between 25.9 μm^2 – 56.8 μm^2) were the lowest values analysed (excluding the Tip categories for reasons discussed below). The low volumes (NMJs 1, 3 and 4) represent the diminished numbers of AChRs in these severely damaged structures.

4.7.4 Day 14 post injury NMJs

The Tip category NMJs in field of view B – as well as NMJ 2 from field of view A if one considers it separately from NMJ 1 - had the smallest surface area, volume and volume/Z-stack values of all NMJs measured in this experiment. This highlights that these sections contained only the tip of NMJ and therefore AChRs visualized did not occupy a large surface area or any depth of structure. This demonstrates the difference between the nature of a scattered NMJ, as seen in day 7 samples, and a tip NMJ as discussed here. This was a learning curve to discover that the quantification of Tip NMJs is meaningless and can be excluded from future studies.

The diagonally sectioned NMJ 2 in Figure 3.7. 5 showed a lesser surface area than the *en face* NMJs of day 14, but its volume and volume/Z-stack measurements were analogous with the *en face* values. This illustrates that the NMJ was orientated in the muscle section to be sectioned along its narrow side, with the complex arrangement of AChRs residing beneath, not visible in the 2D imaging, but clearly visible in 3D analysis.

Since 3D imaging failed to pick up the curving arms of the wrapped around NMJ in Figure 3.7.10, it is not necessary to divulge into further comparisons of this category.

Surface areas of *en face* NMJs in the day 14 sample were, on average, higher than the intact NMJ, averaging 160.0 μm^2. This can be attributed to the increased production of AChR subunits as part of the regeneration process, which is elevated in the second week following muscle contusion injury as seen Section 4.3.2.

4.7.5 NMJs with extended processes rather than junctional folding

The NMJ arranged with multiple extended processes rather than junctional folds in Figure 3.6.7 did not differ from its day 14 *en face* counterparts in surface area and volume, although volume/z-stack value was strikingly high (517 μm^3). The similarity in surface area is logical when one takes into account that the folding of processes only makes the NMJ arms occupy a shallow area, but does not actual make them smaller. This fact also holds true for volume measurements. One can rationalize that the stark increase seen when the volume is divided by the number of z-stacks it traverses results from the extended processes traversing a smaller Z plane than NMJs that had a more 3D

structure due to junctional folding. The z-stack number is therefore smaller for the extended NMJ, but includes a more complete NMJ than some NMJs with junctional folds that were only captured in part. The volume is similar to the *en face* NMJs with standard junctional folding because the larger XY plane measurements of the extended NMJ even though it occupies a less space along the Z plane,

This extended type NMJ has not been presented in the literature to date and it is worth considering that the arrangement of these long extensions rather than detailed folding of their junctional processes may be an alternative manner of NMJ regeneration.

4.8 Effectivity of antibodies tested

This study used some other techniques that were new to our research group. As we strove to visualize the NMJ staining antibody (α-btx) together with the SC staining antibody (BrdU), it was important that these two antibodies were both effective on their own and compatible with one another.

4.8.1 α-Btx as a tool to visualize NMJs

α-Btx proved an excellent tool to identify and visualize NMJs. According to Invitrogen detection technologies, 488 is popular because of brightness, pH insensitivity and much greater photostability than fluorescein α-bungarotoxin pH-insensitivity[82].

It is important to mention one set back with regards to the α-btx antibody which was the long delay in the delivery of the antibody due to recent changes in South African import laws. The resulting 9 month long wait delayed the commencement of laying the ground work for NMJ location and description. This step is crucial as to understand the NMJ's distribution along the chosen muscle of one's study.

It is important to identify a damaged NMJ and track progression of recovery before adding any interventions.

Another attractive option is to co-stain the NMJ sections with an antibody against the nerve (e.g. against neurofilament) in order to describe the morphology of the nerve in the crush or border zone areas of a contused muscle sample. To date staining of the nerve has been used mostly to identify neural degeneration and regeneration in muscle subjected to nerve transection[27] and there is scope for studies on analyses of the nerve following a muscle targeted injury, like the muscle contusion injury.

4.8.2 BrdU as a tool to visualize SCs

BrdU proved a valuable, but complex tool for visualizing SCs in the regenerating muscle and many obstacles arose that compromised the staining success of the anti-BrdU.

For animal work, the added variables of dose and administration efficacy complicate the quest for obtaining identifiable $BrdU^+$ nuclei with the proper IHC techniques – particularly when trouble shooting for the nuclear membrane permeabilization step. In addition, this method requires a number of practise animals and thus alternative procedures for BrdU troubleshooting should be considered.

Cell culture provided a good platform to test efficacy of the BrdU brands. Therefore I suggest further ICC work to clarify a successful method of nuclear depermeabilization and other questions concerning the staining and imaging aspects of BrdU analysis. A simpler method to assess efficiency of BrdU dose, delivery and circulation in the body is to collect blood smears from the animals since white cell proliferation is high. $BrdU^+$ nuclei in the blood stream are abundant and easily visible. Concerning administration by injection one could also determine when BrdU effect starts, peaks and subsides by taking multiple blood smears from the same animal over a period of time.

4.8.3 α-Btx and BrdU as tools to visualize NMJs and SCs together

The nuclear permeabilization step was the truly confounding factor in this project. It required large amounts of trouble shooting to obtain clear BrdU immunofluorescence in the muscle sections. Then, the severity of our chosen permeabilizing agent - HCl - obliterated the neuromuscular junctions, making the goal of visualizing the two counterparts – the NMJ and the SC – together far more complicated than originally anticipated. Options to explore include the use of heat to denature DNA or digestion by DNAse. Alternatively one could use EdU – a nucleoside analogue of thymidine similar to BrdU, but with no need for a nuclear permeabilization step.

The use of DNAse or heat (or replacing BrdU for EdU to eliminate the nuclear permeabilization step) could preserve the α-btx stained AChRs. This is appealing as one could visualize the NMJ and the SC together and capture a single image. This reduces the time spent imaging on the microscope and creates a more unified picture than the two-step staining procedure. Additionally, this method allows us to obtain super-resolution images of the muscle membrane, NMJ, and subsynaptic myonuclei as currently our confocal microscope has no laser to detect Hoechst stained nuclei. Super-resolution images of combined BrdU and AChRs allow for better accuracy in counting subsynaptic nuclei as well further exploring the possibilities of quantifying the dimensions of the neuromuscular components.

4.9 Conclusion

In this study, we successfully induced a standardised skeletal muscle contusion injury in mice using a non-invasive technique. We found an increase in adult (ε) AChRs in injured as well as non-injured mouse *gastrocnemius* muscle during the second week following muscle contusion injury. This indicates that there may be a systemic response to the muscle contusion injury that increases this AChR subunit's mRNA expression, although it is necessary to add a non-injured control group to the study to verify this finding.

We depicted muscle fibres in longitudinal section in a) intact and b) injured skeletal muscle and identified NMJs in both of these sections. We effectively administered BrdU to the mice in this study by means of mini-osmotic pumps and successfully stained immunohistochemically for and imaged $BrdU^+$ cells in the bloodstream (white blood cells) and well as along the myofibres (proliferated SCs). We witnessed a considerable increase in $BrdU^+$ nuclei in muscle sections taken at 3, 5, 7 and 14 days post injury. We detected $BrdU^+$ myonuclei residing beneath the NMJ confirming that the NMJ is indeed an area of SC activity.

We made use of cutting edge technologies to create interactive tile scan images of the entire *gastrocnemius* muscle section; image NMJs in super-resolution and render 3D NMJ constructs to describe and measure intact, damaged and regenerating NMJs. We noted altered morphologies in NMJs following muscle contusion injury as well as a trend towards severe reduction in NMJ size 7 days after the injury event. Thereafter, we observed an increase in NMJ size in regenerating muscle at 14 days post injury that exceeded the values of uninjured, intact NMJ.

This study overcame technical obstacles and laid down foundations to propel future quantitative and qualitative research in the largely unexplored field of neuromuscular regeneration.

References

1. MacIntosh B.R., Gardiner P.F., McComas A.J. *Skeletal Muscle: Form and Function*. 22–48, 257–270. Human Kinetics (2006).

2. Hootman, J.M, Macera, C.A., Ainsworth, B.E., Addy, C.L. and Martin, M.B.S. Epidemiology of musculoskeletal injuries among sedentary and physically active adults. *Med. Sci. Sport. Exerc.* **34,** 838–844 (2008).

3. Kruger, M.J. Antioxidant (Oxiprovi™) supplementation and muscle recovery from contusion injury – an *in vivo* study (Thesis). *Stellenbosch University* (2007).

4. http://www.kinatex.com/en/CommonProblem/Muscle-injuries-12.html.

5. Tatsumi, R., Sankoda, Y., Anderson, J.E., Sato, Y., Mizunoya, W., Shimizu, N., *et al.* Possible implication of satellite cells in regenerative motoneuritogenesis : HGF upregulates neural chemorepellent Sema3A during myogenic differentiation. *American Journal of Physiology - Cell Physiology* 297 C238-C252 (2009).

6. Conboy, I.M., Conboy, M.J., Smythe, G.M. and Rando, T.A. Notch-mediated restoration of regenerative potential to aged muscle. *Science* **302,** 1575–7 (2003).

7. Conboy, M.J., Karasov, A.O. and Rando, T.A. High incidence of non-random template strand segregation and asymmetric fate determination in dividing stem cells and their progeny. *PLoS Biol.* **5,** 1120 – 1126 (2007).

8. Casio, M. Structure and function of the glycine receptor and related nicotinicoid receptors. *J. BIiological Chem.* **279,** 19383–19386 (2004).

9. Christov, C., Chre´tien, F., Abou-Khalil, R., Bassez, G., Vallet, G., Authier, F., *et al.* Muscle satellite cells and endothelial cells : close neighbors and privileged partners. *Mol. Biol. Cell* **18,** 1397–1409 (2007).

10. Ferreira, R., Neuparth, M.J., Ascensão, A., Magalhães, J., Vitorino, R., Duarte, J.A., *et al.* Skeletal muscle atrophy increases cell proliferation in mice gastrocnemius during the first week of hindlimb suspension. *Eur. J. Appl. Physiol.* **97,** 340–6 (2006).

11. Caldas, E. and Araujo, D.A. Adaptation of proof of concepts into quantitative NMR methods : Clinical application for the characterization of alterations observed in the skeletal muscle tissue in neuromuscular disorders. *Univ. Paris Sud* (2014).

12. Gervásio, O.L., Armson, P.F. and Phillips, W.D. Developmental increase in the amount of rapsyn per acetylcholine receptor promotes postsynaptic receptor packing and stability. *Dev. Biol.* **305,** 262–275 (2007).

13. Shi, H., Verma, M., Zhang, L., Dong, C., Flavell, R.A. and Bennett A.M. Improved regenerative myogenesis and muscular dystrophy in mice lacking Mkp5. *J. Clincal Investig.* **123,** 2064–2077 (2013).

14. Hirata, M., Sakuma, K., Okajima, S., Fujiwara, H., Inashima, S., and Yasuhara, M. Increased expression of neuregulin-1 in differentiating muscle satellite cells and in motoneurons during muscle regeneration. *Acta Neuropathol.* **113,** 451–459 (2007).

15. Mizunoya, W., Upadhaya, R., Burczynski, F.J., Wang, G. and Anderson, J.E. Nitric oxide donors improve prednisone effects on muscular dystrophy in the mdx mouse diaphragm. *Am. J. Physiol. Cell Physiol.* **300,** C1065–1077 (2011).

16. Sakuma, K., Nishikawa, J., Nakao, R., Watanabe, K., Totsuka, T., Nakano, H., *et al.* Calcineurin is a potent regulator for skeletal muscle regeneration by association with NFATc1 and GATA-2. *Acta Neuropathol.* **105,** 271–280 (2003).

17. Shinin, V., Gayraud-morel, B., Gomès, D. and Tajbakhsh, S. Asymmetric division and cosegregation of template DNA strands in adult muscle satellite cells. *Nat. Cell Biol.* **8,** 677–687 (2006).

18. Serrano, L.S., Baeza-Raja, B., Perdiguero, E., Jardí, M., Muñoz-Cánoves, P. Interleukin-6 is an essential regulator of satellite cell-mediated skeletal muscle hypertrophy. *Cell Metab.* **7,** 33–44 (2008).

19. Stratos, I., Zhengdong, L., Herlyn, P., Rotter, R., Behrendt, A., Mittlmeier, T., *et al.* Vitamin D increases cellular turnover and functionally restores the skeletal muscle after crush injury in rats. *Am. J. Pathol.* **182,** 895–904 (2013).

20. Wang, Q. and Mcpherron, A.C. Myostatin inhibition induces muscle fibre hypertrophy prior to satellite cell activation. *J. Physiol.* **590,** 2151–2165 (2012).

21. Bourke, D.L., Wylie, S.R., Theon, A., Bandman, E. Myosin heavy chain expression following myoblast transfer into regenerating chicken muscle. *Basic Appl. Myol.* (1995).

22. Yang, S.Y., and Goldspink, G. Different roles of the IGF-I Ec peptide (MGF) and mature IGF-I in myoblast proliferation and differentiation. *FEBS Lett.* **580,** 2530 (2006).

23. Reinecke, H., Veronica, P., and Murray, C.E. Skeletal muscle stem cells do not transdifferentiate into cardiomyocytes after cardiac grafting. *J. Mol. Cell Cardiol.* **34,** 241–249 (2002).

24. Cascio, M. Structure and function of the glycine receptor and related nicotinicoid receptors. *The Journal of Biological Chemistry.* **279, 19,** 19383–19386 (2004).

25. Punga, A.R. and Ruegg, M.A. Signaling and aging at the neuromuscular synapse: lessons learnt from neuromuscular diseases. *Curr. Opin. Pharmacol.* **2,** 1–7 (2012).

26. Pratt, S.J.P., Shah, S.B., Ward, C.W., Inacio, M.P., Stains J.P. and Lovering, R.M. Effects of in vivo injury on the neuromuscular junction in healthy and dystrophic muscles. *J. Physiol.* **591,** 559–70 (2013).

27. Magill, C.K., Tong, A., Kawamura, D, Hayashi, A., Hunter, D.A., Parsadanian, A., Mackinnon, S.E., *et al.* Reinnervation of the *tibialis anterior* following sciatic nerve crush injury: A confocal microscopic study in transgenic mice. *Exp. Neurol.* **207,** 64–74 (2007).

28. Apel, P.J., Alton, T., Northam, C., Ma, J., Callahan, M., Sonntag, W.E., *et al.* How age impairs the response of the neuromuscular junction to nerve transection and repair: An experimental study in rats. *J. Orthop. Res.* **27,** 385–393 (2009).

29. Ma, J., Shen, J., Garrett, J.P., Lee, C.A., Li, Z., Elsaidi, G.A. *et al.* Gene expression of myogenic regulatory factors, nicotinic acetylcholine receptor subunits, and GAP-43 in skeletal muscle following denervation in a rat model. *J. Orthop. Res.* **25,** 1498–1505 (2007).

30. Ma, J., Shen, J., Tan, K.H., Lee, C.A., Elsaidi, G.A., Smith, T.L., *et al.* Gene expression of nAChR, SNAP-25 and GAP-43 in skeletal muscles following botulinum toxin A injection: a study in rats. *J. Orthop. Res.* **23,** 302–309 (2005).

31. Shen, J., Ma, J., Lee, C.A., Smith, B.P., Smith, T.L., Tan, K.H., *et al.* How muscles recover from paresis and atrophy after intramuscular injection of botulinum toxin A: Study in juvenile rats. *J. Orthop. Res.* **24,** 1128–35 (2006).

32. Janssen, I., Heymsfield, S.B., Wang, Z., Ross, R.. Skeletal muscle mass and distribution in 468 men and women aged 18 – 88 yr. *J. Appl. Physiol.* **89,** 81–88 (2000).

33. Saladin K.S. *Anatomy & Physiology: The Unity of Form and Function. 4th edition McGraw Hill* (2007).

34. Sanes, J. R. The basement membrane / basal lamina of skeletal muscle. *J. Biol. Chem.* **278,** 12601–12604 (2003).

35. Proctor, D.N., O'Brien, P.C., Atkinson, E.J., Nair, K.S. Comparison of techniques to estimate total body skeletal muscle mass in people of different age groups. *Am. J. Physiol. - Endocrinol. Metab.* **277,** E489–495 (1999).

36. Zammit, P.S., Partridge, T.A. and Yablonka-reuveni, Z. The skeletal muscle satellite cell : The stem cell that came in from the cold. *J. Histochem. Cytochem.* **54,** 1177–1191 (2006).

37. Zammit, P. S. All muscle satellite cells are equal , but are some more equal than others ? *J. Cell Sci.* **121,** 2975–2982 (2008).

38. Hawke, T.J. and Garry, D.J. Myogenic satellite cells: physiology to molecular biology. *J. Appl. Physiol.* **91,** 534–551 (2001).

39. Lindström, M., Pedrosa-Domellöf, F. and Thornell, L.E. Satellite cell heterogeneity with respect to expression of MyoD, myogenin, Dlk1 and c-Met in human skeletal muscle: application to a cohort of power lifters and sedentary men. *Histochem. Cell Biol.* **134,** 371–385 (2010).

40. Mackey, A. L., Kjaer, M., Charifi, N., Henriksson, J., Bojsen-Moller, J., Holm, L., *et al.* Assessment of satellite cell number and activity status in human skeletal muscle biopsies. *Muscle nerve* **40,** 455–465 (2009).

41. Engelbrecht, L. Grape seed extract affects adhesion competence and maturation of primary isolated rat myoblasts after contusion injury (Thesis). *Stellenbosch University* (2013).

42. Shefer, G., Rauner, G., Yablonka-Reuveni, Z. and Benayahu, D. Reduced satellite cell numbers and myogenic capacity in aging can be alleviated by endurance exercise. *PLoS One* **5,** e13307 (2010).

43. Borisov, A.B., Dedkov, E.I. and Carlson, B.M. Differentiation of activated satellite cells in denervated muscle following single fusions in situ and in cell culture. *Histochem. Cell Biol.* **124,** 13–23 (2005).

44. LeGrand, F. and Rudnicki, M.A. Skeletal muscle satellite cells and adult myogenesis. *Curr. Opin. Cell Biol.* **19,** 628–633 (2007).

45. Wozniak, A.C. and Anderson, J.E. Single-fiber isolation and maintenance of satellite cell quiescence. *Biochem. Cell Biol.* **676,** 674–676 (2005).

46. Rantanen, J., Hurme, T., Lukka, R., Heino, J. and Kalimo, H. Satellite cell proliferation and the expression of myogenin and desmin in regenerating skeletal muscle: evidence for two different populations of satellite cells. *Lab Investig.* **72,** 341–347 (1995).

47. Sadeh, M., Czyewski, K. and Stern, L.Z. Chronic myopathy induced by repeated bupivacaine injections. *J Neurol Sci* **67,** 229–238 (1985).

48. Studitsky, A.N. Free auto- and homografts of muscle tissue in experiments on animals. *Ann. New York Acad. Sci.* **120,** 789–801 (1964).

49. Zammit, P.S., Heslop, L., Hudon, V., Rosenblatt, J. D., Tajbakhsh, S., Buckingham, M.E., *et al.* Kinetics of myoblast proliferation show that resident satellite cells are competent to fully regenerate skeletal muscle fibers. *Exp. Cell Res.* **281,** 39–49 (2002).

50. Van Tubbergh, K. Skeletal Muscle Repair after Micro-Damage: Effect of Ice Therapy on Satellite Cell Activation (Thesis). *Stellenbosch University* (2005).

51. Kummer, T.T., Misgeld, T. & Sanes, J.R. Assembly of the postsynaptic membrane at the neuromuscular junction: paradigm lost. *Curr. Opin. Neurobiol.* **16,** 74–82 (2006).

52. Wurz, J. Why does the body maintain many isoforms of any receptors for any given physiological ligand? (Honours Brain Teaser) *Stellenbosch University* (2013).

53. Albuquerque, E.X., Pereira, E.F.R., Alkondon, M. and Rogers, S.W. Mammalian nicotinic acetylcholine receptors: From structure to function. *Physiol. Rev.* **89,** 73–120 (2009).

54. Purves, D., Augustine, G.J., Fitzpatrick, D., Hall, W.C., LaMantia, A.S., McNamara, J.O. *et al. Neuroscience (4th ed.)*. 122–126 (2008).

55. Unwin, N. Refined structure of the nicotinic acetylcholine receptor at 4A resolution. J Mol Biol. 2005 Mar 4;346(4):967-89. Epub 2005 Jan 25. *J. Mol. Biol.* **346,** 967–989 (2005).

56. Witzemann, V., Brenner, H.R. and Sakmann, B. Neural factors regulate AChR subunit mRNAs at rat neuromuscular synapses. *J. Cell Biol.* **114,** 125–141 (1991).

57. Court, F.A., Gillingwater, T.H., Melrose, S.H., Sherman, D.L., Greenshields, K.N., Morton, A.J. *et al.* Identity, developmental restriction and reactivity of extralaminar cells capping mammalian neuromuscular junctions. *J. Cell Sci.* **121,** 3901–3911 (2008).

58. Sandrock Jnr, A.W., Dryer, S.E., Rosen, K.M., Gozani, S.N., Kramer, R., Theill, L.E. *et al.* Mainenance of acetylcholine receptors by neuregulins at the neuromuscular junction *in vivo*. *Science* **276,** 599 – 603 (1997).

59. McCarthy, J.J., Mula, J., Miyazaki, M., Erfani, R., Garrison, K., Farooqui, A.B., *et al.* Effective fiber hypertrophy in satellite cell-depleted skeletal muscle. *Dev. and Stem Cells* **138,** 3657–3666 (2011).

60. Kues, W.A., Brenner, H.R., Sakmann, B. & Witzemann, V. Local neurotrophic repression of gene transcripts encoding fetal AChRs at rat neuromuscular synapses. *J. Cell Biol.* **130,** 949–957 (1995).

61. Gordon, T. The physiology of neural injury and regeneration: The role of neurotrophic factors. *J. Commun. Disord.* **43,** 265–273 (2010).

62. Goldman, D., Brenner, H. R., Heinemann, S., Arbor, A. and Diego, S. Acetylcholine mRNA levels Are Regulated by Muscle Activity. *Neuron* **1,** 329–333 (1988).

63. Macpherson, P.C.D., Wang, X. and Goldman, D. Myogenin Regulates Denervation-Dependent Muscle Atrophy in Mouse Soleus Muscle. *J. Cell Biochem.* **112,** 2149–2159 (2011).

64. Gigo-Benato, D. Russo, T.L., Geuna, S., Domingues, N.R.S.R., Salvini, T.F. and Parizotto, N.A. Electrical stimulation impairs early functional recovery and accentuates skeletal muscle atrophy after sciatic nerve crush injury in rats. *Muscle nerve* **41,** 685–693 (2010).

65. Mozaffar, T., Strandberg, E., Abe, K., Hilgenberg, L.G., Smith, M.A., and Gupta, R. Neuromuscular Junction Integrity after Chronic Nerve Compression Injury. *J. Orthop. Res.* **27,** 114–119 (2009).

66. Tsai, S.W. Tung, Y.T., Chen, H.L., Shen, C.J., Chuang, C.H, *et al.* Treadmill running upregulates the expression of acetylcholine receptor in rat *gastrocnemius* following botulinum toxin A injection. *J. Orthop. Res.* **31,** 125–31 (2013).

67. Pintér, S., Mendler, L. and Dux, L. Neural impacts on the regeneration of skeletal muscles. *Acta Biochem. Pol.* **50,** 1229–1237 (2003).

68. Sharp, P.S., Dick, J.R.T. amd Greensmith, L. The effect of peripheral nerve injury on disease progression in the sod1 (g93a) mouse model of amyotrophic lateral sclerosis. *Neuroscience* **130,** 897–910 (2005).

69. Nadine, S., Mohammed, A., Gajendran, N., Martinez-Pena, I., Wakefield, S., Thumheer, R., *et al.* Neuregulin/Erb regulate neuromuscular junction development by phosphorylation of dystrobrevin. *J. Cell Biol.* **195,** 1171–1184 (2011).

70. Stratos, I., Graff, J., Rotter, R., Mittlmeier, T. and Vollmar, B. Open blunt crush injury of different severity determines nature and extent of local tissue regeneration and repair. *Am. J. of Pathol.* **182 (3),** 950–957 (2010).

71. Tatsumi, R., Sankoda, Y., Anderson, J.E., Sato, Y. , Mizunoya, W., Shimizu, N., *et al.* Possible implication of satellite cells in regenerative motoneuritogenesis : HGF upregulates neural chemorepellent Sema3A during myogenic differentiation. *Am. J. of Physiol. - Cell Physiol.* **297,** 238–252 (2009).

72. Beiner, J. M. *et al.* The effect of anabolic steroids and corticosteroids on healing of muscle contusion injury. *Am. J. Sports Med.* **27,** 2–9 (1999).

73. Herbernick, M.A. Contusions. *Medscape* emedecine.medscape.com/article/88153–overview (2013).

74. Winkler, T., von Roth, P., Matziolis, G., Schumann, M.R, Hahn, S., Strube, P., *et al.* Time course of skeletal muscle regeneration after severe trauma muscle function against the background of MRI and histological findings. *Acta Orthop.* **82,** 102–111 (2011).

75. Guo, B., Cheung, K., Yeung, S. S., Zhang, B. and Yeung, E. W. Electrical stimulation influences satellite cell proliferation and apoptosis in unloading-induced muscle atrophy in mice. *PLoS One* **7,** e30348 (2012).

76. Kami, K. & Senba, E. In vivo activation of STAT3 signaling in satellite cells and myofibers in regenerating rat skeletal muscles. *J. Histochem. Cytochem. Off. J. Histochem. Soc.* **50,** 1579–1589 (2002).

77. Macaluso, F. *Ethics Application: A Skeletal Muscle Injury Model for Mice*. #2009B02002 (2009).

78. Hirata, M., Sakuma, K., Okajima, S., Fujiwara, H. & Inashima, S. Increased expression of neuregulin-1 in differentiating muscle satellite cells and in motoneurons during muscle regeneration. *Acta Neuropath.* **82 (1),** 451–459 (2007).

79. Sakuma, K. and Yamaguchi, A. The recent understanding of the neurotrophin's role in skeletal muscle adaptation. *J. Biomed. Biotechnol.* **2011,** 201696 (2011).

80. Viguie, C. A., Lu, D., Huang, S. and Rengen, H. Quantitative study of the effects of long-term denervation on the *extensor digitorum longus* muscle of the rat. *Anat. Rec.* **248,** 346–354 (1997).

81. Shi S.L., Fu, A.K.Y., Ip, N.Y. Molecular mechanisms underlying maturation and maintenance of the vertebrate neuromuscular junction. *Trends Neurosci.* **35,** 441–453 (2012).

82. Molecular Probes™ Invitrogen Detection Technologies. α -Bungarotoxin and Conjugates: Product Information. **MP 01175,** 1–2 (2005).

83. Rupp, A., Morrison, I., Barrie, J.A., Halstead, S.K., Townson,K.H., Greenshields, K.N., *et al.* Motor nerve terminal destruction and regeneration following anti-ganglioside antibody and

complement-mediated injury: An *in* and *ex vivo* imaging study in the mouse. *Exp. Neurol.* **233,** 836–48 (2012).

84. Deschenes, M.R., Roby, M.A., Eason, M.K. and Harris, M.B. Remodeling of the Neuromuscular Junction Precedes Sarcopenia Related Alterations in Myofibers. *Exp. Gerontol.* **45,** 389–393 (2010).

85. Yumoto, N., Kim, N. & Burden, S.J. Lrp4 is a retrograde signal for presynaptic differentiation at neuromuscular synapses. *Nature* **489,** 438–442 (2012).

86. Mauro A. Satelite cell of skeletal muscle fibres. *J. Biophys. Biochem. Cytol.* **9,** 493–495 (1961).

87. Exalpha Inc. In Vitro Labeling with Bromodeoxyuridine. https://www.exalpha.com/protocols/brdu–labeling

88. Magavi, S.S.P. and Macklis, J.D. Identification of Newborn Cells by BrdU Labeling and Immunocytochemistry *In Vivo*. **198,** 283–290 (2008).

89. Sigma Aldrich. BrdU Product Information Sheet. **398,** 9285 (1992).

90. The Office of Environmental Health and Safety Boston University. OEHS policies and guidelines: Bromodeoxyuridine (BrdU) treatment http://www.bu.edu/orc/files/2013/06/EHS–Brdu_Treat (2008).

91. Livak K. J., S. T. D. Analysis of Relative Gene Expression Data using Real-time Quantitative PCR and the 2(-Delta Delta C(T)) Method. *Methods* **25,** 402–408 (2001).

92. IHC world H&E staining protocol. www.ihcworld.com/_protocols/special_stains/h&e_el

93. Chan, R.W. and Gargett, C.E. Development of a label retaining cell method to identify stem cells in mouse endometrium. **80,** 2004 (2004).

94. Payne, A.M., Zheng, Z., Messi, M.L., Milligan, C.E., González, E. and Delbono, O. Motor neurone targeting of IGF-1 prevents specific force decline in ageing mouse muscle. *J. Physiol.* **570,** 283–294 (2006).

95. Kuppers, D. Simultaneous cell surface and BrdU staining for flow cytometry. *Fero Lab* http://labs.fhcrc.org/fero/Protocols/BrDUstaining. (2011).

96. Life Technologies. Protocol for dual pulse labeling using EdU and BrdU incorporation. http://www.lifetechnologies.com/za/en/home/references/protocols/cell-and-tissue-analysis/flow-cytometry-protocol/cell-proliferation/dual-pulse-labeling-of-cell-proliferation. (2010).

97. Conboy, I.M., Conboy, M.J., Smythe, G.M. & Rando, T.A. Notch-mediated restoration of regenerative potential to aged muscle. *Science* **302,** 1575–7 (2003).

98. Giordano, C., Rousseau, A.S., Wagner, N. and Gaudel, C. Peroxisome proliferator-activated receptor β activation promotes myonuclear accretion in skeletal muscle of adult and aged mice. *Pflugers Arch - Eur J Physiol* **458,** 901–913 (2009).

99. Sellathurai, J., Cheedipudi, S., Dhawan, J. and Schrøder, H. D. A novel *in vitro* model for studying quiescence and activation of primary isolated human myoblasts. *PLoS One* **8,** e64067 (2013).

100. Srikuea, R., Zhang, X., Park-Sarge, O.K., Esser, K.A. VDR and CYP27B1 are expressed in C2C12 cells and regenerating skeletal muscle: potential role in suppression of myoblast proliferation. *Am. J. Physiol. - Cell Physiol.* **303, 4** C396–C405 (2012).

Appendix A PCR sample preparation

- **Section frozen sample**
- Section samples of ± 30 mg and collect in 2ml RNAse-free Eppendorf tube
- Add 750µl Tri Pure Isolation Reagent
- Place samples on ice

(Can freeze down at this step and continue later)

- **Homogenize sample**
- Clean Homogenizer (Kinematica; Polytron PT2100) with tissue paper and ddH_2O (x2). Check for protein debris.
- Allow to air dry or wash with Tri Pure Reagent if using immediately
- Place individual tube of sample in beaker of ice to keep cool
- Homogenise at 30 000 rpm for 3 x 10 sec
- Wash Homogenizer tip in between samples with ddH_2O (x2)
- Wipe tip with paper towel, check for debris.

Can leave samples for 1 hour on ice or freeze down at this step

- **RNA Isolation**
- Add 200µl chloroform to each tube
- Mix by shaking tube
- Leave for 10min at RT
- Centrifuge 15min at 12g
- See 3 layers

a) Top (clear fluid) – RNA
b) Middle (whitish layer) – DNA
c) Bottom (pink fluid) – Protein

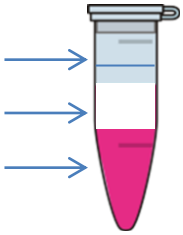

- **Carefully** remove only **top** RNA layer with pipette and place in fresh RNAse-free 1.5ml Eppendorf tube
- Add equal volume of isopropanol to the same volume of RNA
- Shake vigorously

- Leave for 10 min at RT
- Centrifuge for 10min at 12 000 g
- White pellet should now be visible
- Ensure pellet is not free to float in fluid (usually stuck on the bottom tube)
- Gently tip out isopropanol and aspirate the remaining bit out with a pipette
- Add 400µl 70% Sigma Ethanol
- Resuspend the pellet by inverting the tube (this washes away any left over isopropanol)
- Centrifuge for 6min at 8500g – ensure pellet is lying at the bottom
- Remove the ethanol, leave cap open at RT to evaporate any remaining ethanol (5 – 10min)
- Pellet should become invisible
- Add TBE buffer (20 or 30µl, according to size of pellet) – this is now the stock solution
- *Can freeze down or quantify RNA immediately*

Appendix B Sample preparation and RNA Quantification

Sample preparation

- Label small 0.5ml RNAse- free eppendorf tubes accordingly
- Add 14 µl of RNAse- free H_2O at a dilution of1:15, or 19 µl if RNA content is high and need a more diluted (more reliable) 1:20 solution. NOTE DILUTION USED.
- Pipette 1µl of RNA sample into tube and pipette up and down to mix
- Keep eppendorf tubes on ice
- Prepare a separate Eppendorf tube of RNAse- free H_2O (for cleaning) as well as a solution with 1µl of TE buffer in place of sample (as blank)

Quantification

Quantify with Nanodrop Lite Spectrophotometer (Thermo Scientific)

- Lift lid and rinse with a 1µl of H_2O sample, repeat.
- Wipe dry
- Choose 'RNA' option
- Measure Blank (TE control)
    - Add 4µl of TE close lid and press "Blank"
    - Repeat step to "Confirm"
- Wipe dry and add same amount of first sample
- Close lid and press "Measure"
- Note reading 1
    - RNA reading in ng/µl
    - A260/A280 value
- Repeat until satisfied with consistent readings (3-5x)
    - Readings should be within 0.03 of each other (values lay between 1.7 – 2.1)
- Wipe dry and repeat with next sample

Calculate average of readings for each sample to get RNA concentration

Appendix C Reverse Transcription Protocol

Step 1: Sample preparation

- 1µg mRNA per sample
- Prepare each sample in duplicate
- Make up a total volume of 11ul

1 Add:

1) 7µl sample
2) 2µl DNAse buffer
3) 2µl DNAse enzyme

2 Incubate for 20 min at 30°C (Applied Biosystems 2720 Thermal Cycler)

3 Add 0.22µl of 0.2M EDTA

4 Heat at 75°C for 10min

5 Place samples on ice.

Step 2: Reverse Transcription RNA → cDNA

1. Add 2µl primer (random hexamer primers, Roche) – therefore 13µl of volume in tube
2. Heat for 10min at 60°C
3. Add to solution:

3.1. 4µl 5x Buffer

3.2. 0.5µl RT enzyme

3.3. 0.5µl protector RNAse

3.4. 2µl DNTP deoxynucleotide triphosphate

= total volume of 20µl in tube to give a final RNA concentration of 1000/20 = 50ng/µl

4. Heat for 10min at 25°C and 60 min at 50°C
5. Heat at 85°C for 5min
6. Place tubes on ice

Appendix D Haematoxylin and Eosin Staining Protocol

Cryo-sections:

Leave frozen slides in Coplin jar for 3 minutes to thaw

i) Rinse in distilled water (ddH_2O) – 2 dips
ii) Harris haematoxylin – 3 min
iii) Rinse in ddH2O
iv) Acid alcohol – 20 dips -4 min
v) Rinse in ddH2O
vi) Blue in Scott's Tap water – 2 dips
vii) Rinse in ddH2O
viii) Eosin – 30 s
ix) Rinse in ddH2O
x) Mount with a coverslip using DPX Mountant/ mounting media

Appendix E Immunofluorescence Staining Protocol

i) Leave slides to thaw (if stored in freezer , -4˚C): thaw for 3 min

ii) Paraformaldehyde (2% in 10x PBS): incubate for 8 min

iii) Triton X-100 (0.25%): incubate for 15 min

iv) Wash with 1x PBS: 3 x 5 min

v) Dry around section and circle with wax pen

vi) Denaturing/depurinating step (for BrdU sections only):

i) HCl 2M : incubate for 30 min (initial work)

ii) HCl 2M: incubate for 90 min (2013 – best results)

iii) HCl 4M: incubate for 30 min (2014 – best results)

iv) Methanol/Acetone 1:1: incubate for 10 min (for BrdU/α-btx sections)

vii) Wash with 1x PBS: 1 x 10 min; 1 x 5 min

(First wash longer to neutralize HCl or methanol/acetone)

viii) Blocking serum (5% Donkey serum and 1% BSA in 1x PBS)

ix) Wash with 1x PBS: 3 x 5 min

x) Primary Antibodies: incubate overnight (5 pm – 8 am)

a. Laminin (1:250)
b. BrdU555 (1:20)
c. BrdU555 (1:20)/ Laminin (1:250)
d. BrdU555 (1:20)/ CD56 (1:50)/ Laminin (1:250)
e. fMHC (1:200)/ Dystrophin (1:200)

xi) Wash with 1x PBS: 3 x 5 min

xii) Secondary Antibodies: incubate for 1 hr

a. AlexaFluor594 (1:250)/ α-btx488 (1:1000)
b. (no secondary antibodies for BrdU555 staining alone)
c. AlexaFluor594 (1:250)
d. AlexaFluor488 (1:100)/ AlexaFluor594 (1:250)
e. AlexaFluor555 (1:200)/ AlexaFluor594 (1:250)/ α-btx488 (1:1000)

xiii) Wash with 1x PBS

xiv) Hoechst (1:500): incubate for 15 min

xv) Wash with 1x PBS: 3 x 5 min

xvi) Dry and mount with tissue mounting medium

xvii) Wrap in foil for transport or storage

Briefly, slides were immersed in 4% Paraformaldehyde for 8 minutes followed by 0.1% Triton-X for 15 minutes. After washing with 0.1M PBS (1 ℓ of 1 M phosphate buffer, 90 g NaCl, 9 ℓ ddH2O; pH 7.4; 5 minutes x 3 for all the washing steps mentioned) slides were dried, and sections encircled with a wax pen. For nuclear permeabilization of BrdU sections, sections were left in 2M Hydrochloric acid for 90 minutes followed by another washing step. Non-specific binding sites were blocked by incubating the sections with Blocking serum (5 % donkey serum; 1% BSA) at room temperature for 1 hour. The serum was then washed off and primary antibody added to the slides and incubated at 4°C overnight (5pm – 9am). In the morning, slides were washed prior to addition of secondary antibodies for 1 hour. After washing, the nuclear stain, Hoechst (1:500) was added and left for 15 minutes. Slides were dried and fluorescent mounting medium (Dako, Diagnostech) added to allow the coverslip to be laid on top.

Descriptions of antibodies and motivation for using these:

4 **Anti-Laminin:** attaches to laminin – the structural protein of the sarcolemma

5 **α-Bungarotoxin Alexa488 Conjugate:** neurotoxin from *bungarus multicinctus* snake that targets AChRs of the NMJ

6 **Anti-BrdU:** attaches to BrdU **-** labels proliferated nuclei that have incorporated BrdU into their DNA

7 **Anti-NCAM:** attaches to CD56 (or NCAM) - membrane marker of activated SC (also of Natural Killer cells)

8 **Anti-fMHC:** attaches to fMHC - indicator of regenerating muscle fibre

9 **Hoechst:** standard nuclear stain

Appendix F Cell Culture Protocol

Media:

1. Proliferation medium (PM)
    1. 440ml Dulbecco's modified eagles medium (DMEM)
    2. 50ml FCS (10%)
    3. 5mL Penstrep Penicillin/Streptomycin (1%)
    4. 5ml L-glutamine (1%)
2. Sterile 1x Phosphate buffered saline (PBS)
3. Trypsin-EDTA

Cell thawing and proliferating:

4. Warm up proliferation medium in water bath (37^{o}C)
5. Add 2 ml warm PM to 15 ml falcon tube
6. Remove 1 vial of C2C12 cells (1 x 10^{6} cells/1 ml per vial) from liquid nitrogen cell tank
7. Thaw cells (± 2 min)
8. Add cells to falcon tube
9. Centrifuge (3 min at 1500 r.p.m)
10. Add 4 ml PM in T25 or 9 ml PM in T75
11. After centrifugation, Remove supernatant(PM and specifically DMSO- cryoprotectant, but toxic to cells)
12. Resuspend cells in 1 ml PM and add to T25/T75
13. Incubate for 1 day (T25) or 2 days (T75)

Seeding:

14. Remove PM from flask

15. Wash with sterile PBS (sPBS)

    1. ± 8ml (T75)

    2. ± 4ml (T25)

16. Remove PBS

17. Add 4ml Trypsin-EDTA (T75) (?2ml for T25)

18. Incubate (37^{o}C, 4 min)

19. Add PM (8 ml) in 15 ml Falcon tube

20. Spin down (3 min, 1 500 R.P.M)

21. Remove medium

22. Resuspend pellet in 1ml PM

23. Count cells (10µl per window on haemocytometer)

24. Make up resuspended solution of ± 5 000 cells per 500µl PM

25. Seed in 24 well plates (500µl per well ∴ 5 000 cells per well)

(Can seed extra in a T25 if necessary to repeat cell staining procedure)

26. Leave to settle for ± 2 hours in incubator

27. Add BrdU diluted in PM (final concentration of 10µM per well) to each well

Appendix G Immunocytochemistry Protocol

(Adapted for anti-BrdU AlexaFluor 555 Conjugate from work by Lize Bruwer, Thesis 2013)

Staining Protocol in wells

Work on a black box with damp tissue paper in the middle compartment

When working with $BrdU^+$ cells work in dark conditions (light sensitive)

Keep all of following items on ice (calculate amounts according to amount of sections to stain and size of wells)**:**

1. **Fixative** – acetone: methanol (1:1) (in Molecular Lab – work in fume hood)
2. **Blocking** – 2% BSA in 10x PBS
3. **BrdU AlexaFluor 555 Conjugate**- made up in 10x PBS (made up at optimum concentration, in an eppendorf covered in foil – LIGHT SENSITIVE)
4. **Hoechst** – 1:1000 made up in 10x PBS (made up at optimum concentration, in an eppendorf covered in foil – LIGHT SENSITIVE)

Methods

Steps for staining cells in 24 well dish:

5.	**Washing x2:**	Add 250µl 1x PBS to each well	**5 min**
6.	**Fixing:**	Add 250µl acetone:methanol per well	**10 min**
7.	**Washing x3:**	Add 250µl 1x PBS to each well	**5 min**
8.	**Blocking:**	Add 250µl 2% BSA to each well	**1 hour**

9. Pipette blocking solution gently off cells

DO NOT WASH NOW!

WORK IN THE DARK FROM THIS STAGE ONWARDS!

10.	**Primary ab:**	Add 100µl of antibody solution to each well	**2 hour RT**
11.	Remove by gentle pipetting		
12.	**Washing x3:**	add 250µl 1x PBS	**10 min**
13.	Remove by gentle pipetting		
14.	**Hoechst:**	add 200µl Hoechst solution	**10 min**
15.	Remove by gentle pipetting		
16.	**Washing x3:**	add 250µl 1x PBS	**10 min**
17.	Remove by gentle pipetting		
18.	Let wells air dry for a few minutes before imaging		

Appendix H Antibody combinations

H.1 Introduction

Following the complications of staining BrdU and α-btx on the same section, the decision was made to image two consecutive sections, one with BrdU, the other with α-btx. Antibodies that would complement the study were chosen to be imaged as the fourth frequency in each section - 488 in the BrdU stained section and 555 in the α-btx stained section.

Nuclear membrane marker, CD56 (or NCAM) marks activated satellite cells (K4) was therefore chosen to assist in confirming satellite cells in the BrdU-stained section.

Fetal Myosin Heavy Chain (fMHC) is present in newly formed or regenerating muscle fibres and thus distinguishes these from normal adult muscle fibres (K4). We chose fMHC to stain with the α-btx sections to help determine whether the NMJs imaged were residing on regenerating fibres or not.

Table H.1 Antibody Combinations

Purpose	Antibody, Concentration, Brand and Catalogue nr	Species	Secondary	Species
For regeneration NMJ and myofibres	**α-btx** (1:1000) Life Technologies B13422	*Bungarus Multicinctus*	**(Conjugate with AlexaFluor®488)**	/
	fMHC (1:200) DBHS N2.261	Mouse monoclonal	**AlexaFluor®555** (1:200) Abcam AB150106	Donkey anti-mouse
	Dystrophin (1:200) Santa Cruz Sc-15376	Rabbit polyclonal	**AlexaFluor®594** (1:250) Life Technologies A21207	Donkey anti-rabbit
For Satellite cells	**BrdU** (1:20) Life Technologies B35131X	Mouse monoclonal	**(Conjugate with AlexaFluor®555)**	/
	CD56 (NCAM) (1:50) Santa Cruz sc-1507	Goat Polyclonal	**AlexaFluor®488** (1:50) Abcam AB150129	Donkey anti-Goat
	Laminin (1:250) Dako Z0097	Rabbit polyclonal	**AlexaFluor®594** (1:250) Life Technologies A21207	Goat anti-rabbit
For Both	**Hoechst** (1:500) Sigma 14533	Nuclear stain	(Excitation wavelength: 350nm)	/

IH2. Methods

Two sections per slide were stained in combinations as per Table I.1 according to the IHC protocol in Appendix H with adaptations as per Table I.2

Table H.2 Staining guide for different antibody combinations (for IHC protocol in Appendix E).

Antibody Combinations	Step 6	Step 10	Step 12
BrdU/CD56/Laminin	6.2	10.4	12.4
fMHC/α-btx	N/A	10.5	12.5

Images were taken with confocal microscope (Zeiss LSM 780) at 20x and 40x magnification.

H.3. Results

CD56 as a complimentary antibody to BrdU

CD56 was most prominently seen in Natural Killer Cells in blood vessels of the myofibre (see Figure I.1). CD56 was successfully visualised in myofibres, fitting the criteria for satellite cell determination (see Figure I.2). However the secondary antibody created crystals resulting in grainy images with too much autofluorescence which compromised the search to pinpoint activated satellite cells.

BrdU staining was unsuccessful and therefore not possible to envision with CD56 stain.

fMHC as a complimentary antibody to α-btx

fMHC was successfully imaged with α-btx (see Figure I.3). However, fMHC fluorescence picked up many of the sarcolemma structures, questioning the specificity of the antibody.

H.4 Conclusion

Due to the unreliability of the AlexaFluor 488 for CD56 staining as well as uncertainties of the fMHC antibody's true positivity, another technique was chosen of of staining sections for α-btx – imaging – restaining with HCl for BrdU – imaging.

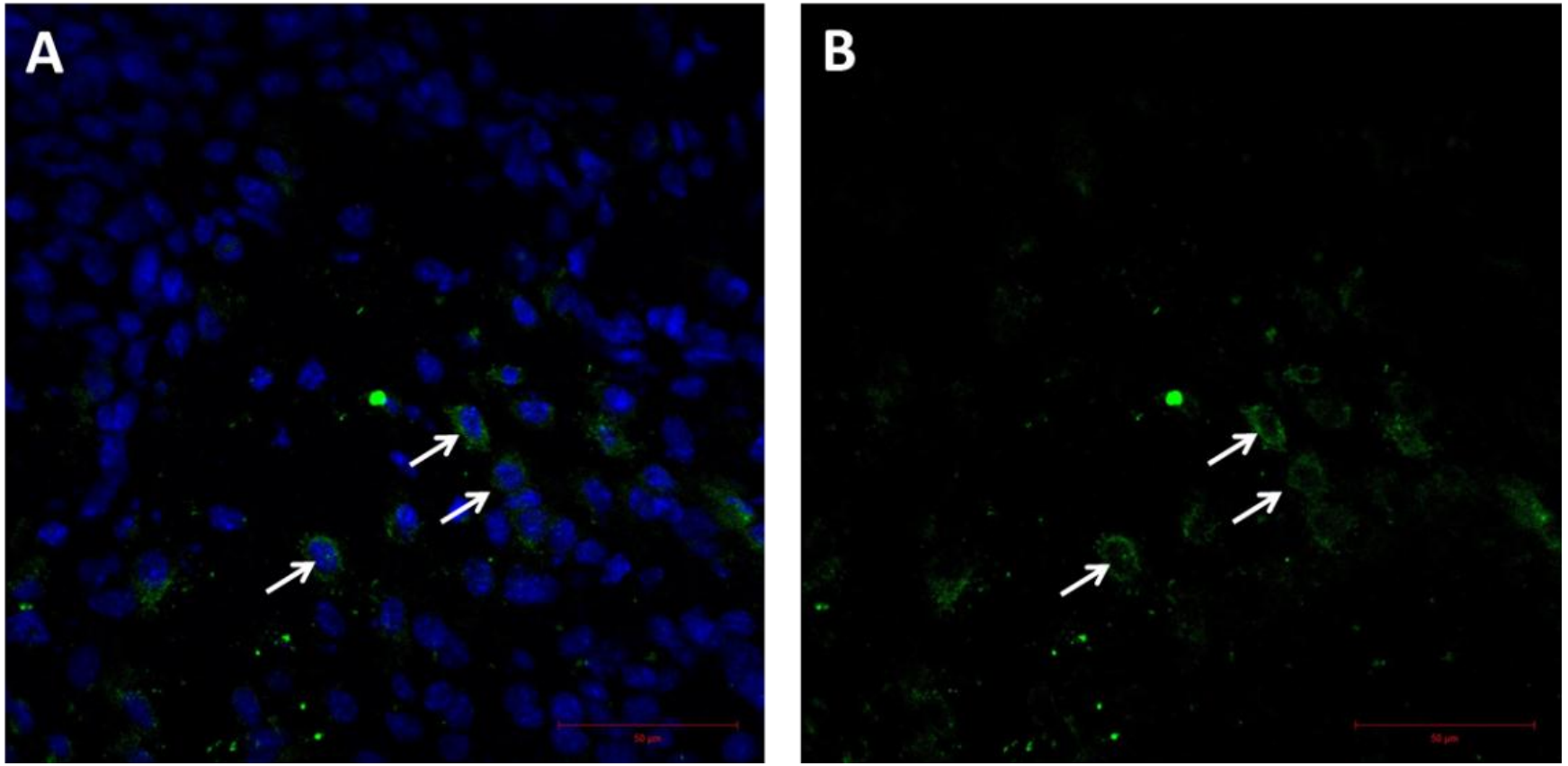

Figure H.1 Natural Killer cells (white arrows) in the blood stream in the *gastrocnemius* muscle, 7 days post injury. **A)** Positive NCAM staining (green) in the membrane of the Hoechst stained nucleus (blue) **B)** NCAM staining the nuclear membrane (40x magnification.)

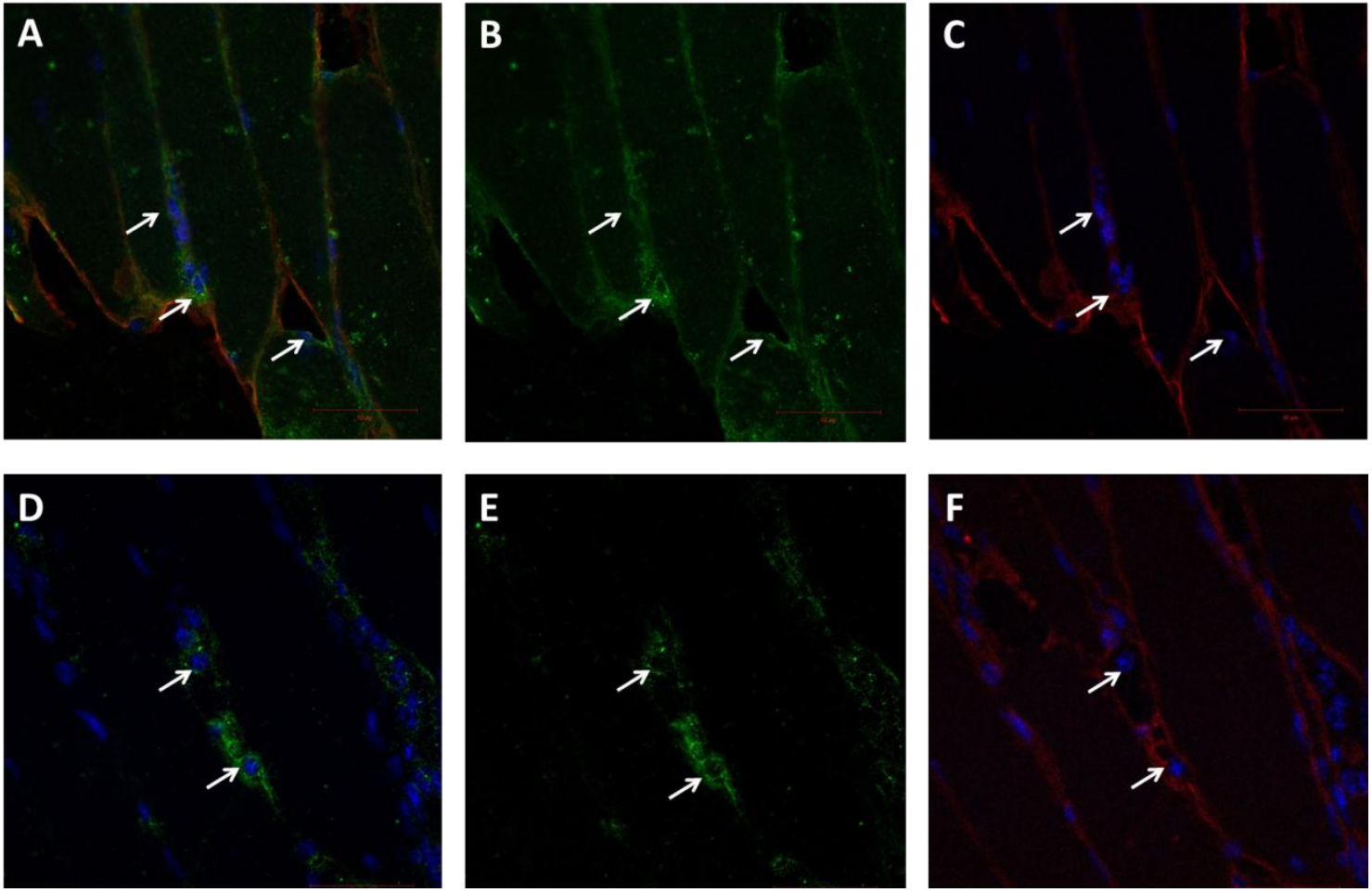

Figure H.2 Satellite Cells (white arrows) in *gastrocnemius* muscle, 7 days post injury. Satellite cells are indicated by **A)** and **D)** nucleus (blue) surrounded by **B)** and **E)** CD56 stained myonuclei enclosed within **C)** and **F)** the sarcolemma, shown by laminin staining (red). (40x magnification)

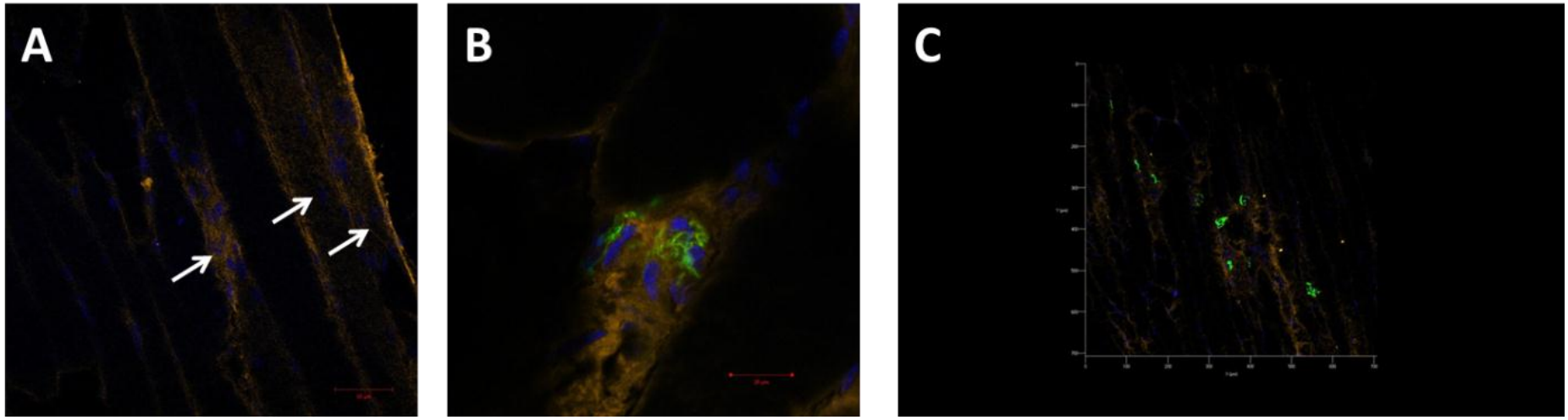

Figure H.3 fMHC surrounding the NMJ in injured *gastrocnemius* muscle sections, 7 days post injury. **A)** Showing positively stained myofibres (orange) with centralised nuclei (blue) (white arrows) confirming myofibre regeneration. **B)** A 40x magnification showing a damaged NMJ (green) with a localisation of fMHC. **C)** A 3D image at 20x magnification showing NMJs arranged along a number of $fMHC^{+}$ stained fibres.

Appendix I BrdU *in vivo* Dose Table

Author, Journal & Date	Species & Age (if available)	BrdU Dose & Source (if available)	Time of injections	Intervention and time of analysis	Analysis	DNA denaturing (depurinate) step
General Protocols						
Fero Lab[95]	/	/	30-100 mg/kg BW (0.1mL/gm) 1-2 hours before sacrifice	/	/	2.5 N HCl, 37°C 15min or 0.1N NaOH can also be used
OEHS Boston University[90]	/	/	2 mg in 100µl of sPBS IP injections daily for up to 1 week. Injection a few hours before analysis	/	/	/
Life Technologies[96] **BrdU staining protocol**	/	1 ml concentrated reagent per 100 g BW Life Technologies	2 hours before sampling	/	/	/
Articles						
Christov[9] ***MBoC*** **2007**	Myf5nlacZ/+ pups Myf5nlacZ and Myf5GFP-P knock-in mice	50 mg/kg BW	Twice daily From postnatal days 3–8	None	*Tibialis anterior* 6 weeks (42 days)	2 N HCl for 30 min at 37°C
Conboy *et al.*[97] ***Science*** **2003**	Male C57BL/6 mice young - 2/3 months,	Not specified	2days after injury 2hrs before sampling Or 3 days before sampling, ie d5 after	Injections (Notch inhibitor /activator/control) **For SC analysis:** pierced multiple times with a 23-	Proliferating cells	Not specified

	adult - 5/7 months, and aged - 23/24 months		injury	gauge needle **Tissue response to injury:** dry ice for 5 seconds		
Conboy *et al*[7] *PLoS Biology* 2007	Species not specified	30 mg/kg BW Sigma	Two doses (4h apart) within first 48h after muscle injury	CTx - intramuscular injection	Cells from regenerating muscle	2.5 M HCl for 30 min
Court *et al.*[57] *J of Cell Science* 2008	C57Bl/6	Not specified	3 days or 4 days after denervation injection	2.5 µl botulinum toxin type A injection	TS muscle	Not specified
Ferreira *et al.*[10] *Eyr J of Appl Physiol.* 2006	Male CD1 mice	50 mg/kg	Once 48hr before sacrifice	Hind limb suspension	*Gastrocnemius*	2 M HCl 30 min at 56°C
Giordano *et al.* [98] *Eur J Physiol* 2009	Male C57BL6J and B6D2 10 weeks	100 mg/kg Sigma	Daily (9am)	None	*Tibialis anterior* muscles and duodenum	not specified
Guo *et al.*[75] *PLoS ONE* 2012	BALB-C Mice	10mg/ml	Daily for 14 days	Unloading Electrical stimulation	Proliferating SCs	2 N HCl Time not specified
Hao Shi *et al.*[13] *J of Clinical Inv.* 2013	MKP-5 knockout mice	100mg/kg Developmental Studies Hybridoma Bank	Once, 24hours after injection, 18hrs before sampling	Injection of CTx 50 µl CTX (*tibialis anterior)* 300 µl CTx *(gastrocnemius, soleus)*	*Tibialis anterior, gastrocnemius , soleus*	1.5 M HCl 30 minutes at RT
Hirata *et al.*[14] *Acta Neuropathol* 2007	Adult male Wistar rats 10 weeks	100 mg/kg Roche Diagnostics	1 h before sampling	intramuscular injection - bupivacaine	*Tibialis anterior* and spinal chords	Not specified
Mizunoya et al.[15] *Am J Physiol Cell* 2011	Dystrophic mdx mice	100 mg/kg Sigma	Two hours before euthanasia	Oral administration of Nitric oxide donor reagents	*Diaphragm; quadriceps; triceps surae and heart*	2 N HCl 1 hour

Sakuma et al.[16] *Acta Neuropathol* 2003	Male Wistar Rats - 10 and 20 weeks & DWJ mice - 12 weeks	100mg/kg Boehringer,Mannheim	1 hr before sampling	Intramuscular injection - bupivacaine	*Tibialis anterior* 4, 6 and 8 days post-surgery	Not specified
Serrano *et al.*[18] *Cell Metab* 2008	IL-6−/− mice	30 mg/kg BW Sigma	Daily for 2 days	Immobilization of muscle via tendon transection	*Plantaris* muscle	Not specified
Shinin *et al.*[17] *Nature Cell Biol* 2006	Myf5nlacZ/+ knock-in mice	25 µg /g (post-natal growth) Or 30µg/g (post freeze injury) Sigma	Twice daily for 6 days, 4-10 weeks of chase Or Three times daily for 3 days 4-12 weeks of chase	None	isolated myofibres	4N HCl (20 minutes) Or cells: DNAse I 30 min at 37 °C
Stratos *et al.*[19] 2 *Am J of Pathology* 013	Male Wistar rats 300-325 g	50 mg/kg IP	48h prior to final experiments at days 1, 4, 14, 42 post-injury	Muscle crush injury	*Soleus*	Not specified
Wang *et al.*[20] *J of Physiology* 2012	Male Mstn WT and KO mice	50 mg/kg Sigma	Daily 48hr; 7 days; and 14 days	Injections of soluble activin receptor type IIB or control	*Tibialis anterior* and *extensor digitorum longus* (muscle tissue and isolated myofibres)	DNase I (Roche) in DMEM 37◦C for 30 min.

Appendix J BrdU *in vitro* Dose Table

Author & Journal	Cell type & BrdU Source	BrdU Dose & Incubation Time	DNA denaturing step
Life technologies **BrdU Labelling protocol**[96]	/ Life Technologies	1:100 from concentrate 37°C for 60 minutes to overnight	1:1 Denaturing solution from Invitrogen BrdU Staining kit 30 minutes at 37°C
Bourke *et al.*[21] ***BAM*** **1995**	myoblasts (unspecified) Brand unspecified	10mM BrdU 14-16 hours	Not specified
Reinecke *et al.*[23] **J Mol Cell Cardiol.** **2002**	SCs isolated from male Fischer rats Brand unspecified	10µM Overnight	0.1 N HCl for 30 min at 37°C then 1.5 N HCl for 15 min at 37°C then 0.1 M boric acid for 10 min at RT.
Sellathurai *et al.*[99] ***PLOS One*** **2013**	3 human primary myoblast cultures BrdU (Sigma- Aldrich).	100 µM BrdU 1 hr pulse or 10 µM fcumulative BrdU incorporation	2 N HCL for 30 min
Serrano *et al.*[18] ***Cell Metabolism*** **2008**	C212 Sigma	5 mg/ml) 1 h at 37ºC prior	Not specified
Shinin *et al.*[17] ***Nature Cell Biology*** **2006**	Isolated myofibres from Myf5nlacZ/+ knock-in mice BrdU (Sigma, St Louis, MO)	0.2µM BrdU 48 hrs - replaced with new BrdU for chase (18-16hrs)	2000U DNAse I (Roche, Basel, Switzerland) per 2–5 × 10^5 cells 30 min at 37 °C
Srikuea *et al.*[100] **AJP – Cell Phys** **2012**	C2C12 cmyoblasts BrdU (Sigma)	10 µM 1 h at 37°C and (5% CO_2)	Not specified
Tatsumi *et al.*[71] ***AJP-Cell Phys*** **2009**	Cultured SCs isolated from muscle groups 9-mo-old (adult) male Sprague-Dawley rats Sigma (St. Louis, MO	10 µM 2 hours	Not specified